HELLENIC REPUBLIC
UNIVERSITY OF IOANNINA
SCHOOL OF ENGINEERING
DEPARTMENT OF MATERIALS SCIENCE AND ENGINEERING
MASTER OF SCIENCE IN
«TECHNOLOGIES OF ADVANCED MATERIALS»

THEORETICAL ANALYSIS AND DESIGN OF INTEGRATED SPLIT-GATE GRAPHENE PHOTODETECTORS

Vasileios Georgakopoulos Paltidis

MASTER'S THESIS

IOANNINA 2022

HELLENIC REPUBLIC
UNIVERSITY OF IOANNINA
SCHOOL OF ENGINEERING
DEPARTMENT OF MATERIALS SCIENCE AND ENGINEERING
MASTER OF SCIENCE IN
«TECHNOLOGIES OF ADVANCED MATERIALS»

THEORETICAL ANALYSIS AND DESIGN OF INTEGRATED SPLIT-GATE GRAPHENE PHOTODETECTORS

Vasileios Georgakopoulos Paltidis

MASTER'S THESIS

IOANNINA 2022

Η παρούσα Μεταπτυχιακή Διατριβή εκπονήθηκε στο πλαίσιο των σπουδών για την απόκτηση του Μεταπτυχιακού Διπλώματος Ειδίκευσης στην εξειδίκευση: Υπολογιστική φυσική των υλικών που απονέμει το Τμήμα Μηχανικών Επιστήμης Υλικών του Πανεπιστημίου Ιωαννίνων.

Εγκρίθηκε την Παρασκευή 15/07/2022 από την εξεταστική επιτροπή:

1. Λοιδωρίκης Ελευθέριος, Καθηγητής του Τμήματος Μηχανικών Επιστήμης Υλικών της Πολυτεχνικής Σχολής του Παν/μίου Ιωαννίνων, **Επιβλέπων**

2. **Λέκκα Χριστίνα,** Αναπληρώτρια Καθηγήτρια του Τμήματος Μηχανικών Επιστήμης Υλικών της Πολυτεχνικής Σχολής του Παν/μίου Ιωαννίνων, **Μέλος τριμελούς επιτροπής**

3. **Παπαγεωργίου Δημήτριος,** Αναπληρωτής Καθηγητής του Τμήματος Μηχανικών Επιστήμης Υλικών της Πολυτεχνικής Σχολής του Παν/μίου Ιωαννίνων, **Μέλος τριμελούς επιτροπής**

ΥΠΕΥΘΥΝΗ ΔΗΛΩΣΗ

"Δηλώνω υπεύθυνα ότι η παρούσα διατριβή εκπονήθηκε κάτω από τους διεθνείς ηθικούς και ακαδημαϊκούς κανόνες δεοντολογίας και προστασίας της πνευματικής ιδιοκτησίας. Σύμφωνα με τους κανόνες αυτούς, δεν έχω προβεί σε ιδιοποίηση ξένου επιστημονικού έργου και έχω πλήρως αναφέρει τις πηγές που χρησιμοποίησα στην εργασία αυτή."

(Υπογραφή υποψηφίου)

PROLOGUE

I would like to thank my thesis supervisor Elefterios Lidorikis, professor at the department of M.S.E, for his guidance and teaching efforts throughout my learning journey. I would also like to thank the members of the examining committee, associate professor of M.S.E Christina Lekka and associate professor of M.S.E Dimitrios Papageorgiou for reviewing the thesis and providing constructive feedback. I also want to express my gratitude towards all the members of the CMSL lab and especially Ioannis Vangelidis and Dimitris V. Bellas for numerous fruitful discussions and help through all the hurdles encountered. Finally, but most importantly a big thanks to my family for their unconditional support.

ABSTRACT

The aim of this thesis is to investigate by theoretical means the physical mechanisms and working principles of integrated split-gate graphene photodetectors with the aim of designing novel state of the art devices. The recent surge in data traffic volumes creates a demand for more power efficient, complementary metal oxide (CMOS) compatible, high-speed optical communications. Traditional semi-conductor photodetectors fail in simultaneously addressing all these requirements facing issues in integration, complexity and spectral limitations while already being mature technologies. Graphene is a novel 2D material possessing broadband tunable light-matter interactions and exceptional charge transferring properties, properties that render it popular as an active layer in optoelectronic devices. Graphene based photodetection is promising satisfying most of these requirements with the major shortcoming being low power efficiency, described by figures of merit such as voltage-current responsivity RV-RI. Optical absorption in graphene results in energy transfer to the electronic system creating a thermalized hot carrier distribution. Due to an electron-phonon relaxation bottleneck graphene is able to de-couple its electronic temperature from the lattice resulting in a strong photo-thermoelectric effect (PTE), ideal for unbiased photodetection applications. Enhancing optical absorption is key to optimizing performance. Integrated photonic devices involve multiple optically active components (WGs, gates, contacts) arranged in complex photodetection schemes resulting in dynamic absorption-loss phenomena. To account for these, we perform 3D finite difference time domain (FDTD) simulations to obtain the optical absorption distribution and understand the sources of parasitic loss for a given device geometry. The same geometric parameters affect the electronic behavior of the device entangling absorption and thermoelectric effects. To explore the rich physics of the thermoelectric phenomena in a device with non-uniform absorption, temperature and charge density distributions, tools are developed, namely numerical solutions for the Poisson equation governing the static charge density and the thermoelectric equation governing heat and charge transport inside the active layer. The combined tools are then used to explore the impact of different geometric parameters on device performance, successfully simulating experimental results, addressing debated topics cited in literature and laying out a complete framework for studying device photo-thermo-electric phenomena in graphene.

Contents

1 Introduction to photodetection

1.1 Photodetection

Absorption is the process where light interacts with matter transferring its energy to the electronic system in the process. Photodetectors are devices comprised of different materials and geometries in order to facilitate light absorption and efficient charge transport enabling signal conversion. Traditionally this has been achieved with semiconducting materials like Si due to their unique electronic band structure characterized by a band gap in the range of a few eV. Photons with energy above the band gap promote electrons from the valence band to the conduction band. Simultaneously bias voltages accelerate the free electrons towards the source-drain terminals completing the cycle of signal conversion. Dark current , a consequence of bias voltage, is usually associated with fluctuations in a measured signal due to random time arrival of energy carriers decreasing the sensitivity of the detector [1]. In the near infrared (telecom spectrum) the energy of the incoming photons is not enough to overcome the Si band gap. The photonics industry has developed solutions to overcome this barrier combining Ge with Si [2] and compound (III-IV) semiconductors to achieve photodetection in these spectral ranges that reaches ~ 1 A/W responsivities and 60-100 GHz detection speeds, but these often require complex fabrication or require non-CMOS compatible materials while being mature technologies already performing at their physical limits [3]–[5]. Graphene's conical shaped electronic band structure coupled with high mobilities and ultrafast dynamics offers an alternative solution to these legacy systems. The zero-gap semiconductor is free of the spectral limitations associated with a fixed band gap electronic materials but this comes at the cost of increased dark current at lower bias voltages [6]. Unbiased configurations combine low dark currents with ultrafast dynamics that enable high detection speeds with the major shortcoming being low responsivity. Producing novel designs and optimizing existing ones based on a deep understanding of the underlying physical mechanisms is of paramount importance towards achieving a future of efficient high-speed broadband photodetection.

1.2 THz light sensing

Si-graphene based high responsivity photodetection devices have been realized for wavelengths < 1100 nm operating on the photogating effect where light absorption in heavily doped Si/SiO2 substrate generates carriers with prolonged lifetimes. However, this sacrifices the intrinsic high carrier mobility, which seriously restricts the response speed of graphene photodetectors [7]. In the terahertz frequencies, hot-carrier assisted photodetection has been proven the most efficient being fast and inherently broadband detection mechanism combined with low noise. Antenna coupled graphene field effect transistors integrated with lithographically-patterned high-bandwidth (~100 GHz) chips allow for time resolved THz spectroscopy in gases, imaging, metrology, ultra-fast data communications and for capturing snapshots of ultrafast dynamics, in materials and devices, at the nanoscale[8]. Devices can operate in single or dual gating architectures figure 5.1 with dual gate outperforming single gate. This is attributed to the greater control in Seebeck ΔS and small area of illumination which enhances the temperature gradient created [9].

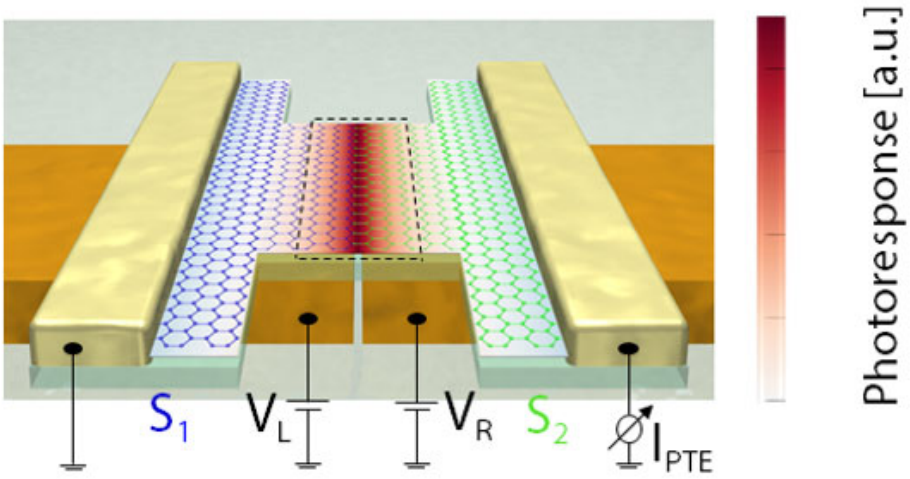

Figure 5.1 Antenna branches apply voltages V_L, V_R creating a p-n junction. The central part of the junction is where THz light is concentrated by the antenna gap. Color map shows the photocurrent response of the device.

1.3 Integrated photodetection

Photonic integrated circuits (PIC) leverage the ability of photonics for signal transmission and target to cointegrate them in the framework of traditional electronics in order to achieve better computing performance. Although traditionally used in sensing applications photodetection (PD) has risen to prominence as it plays a crucial role in optical communications serving as the opto-electronic link responsible for signal conversion. Shiue et al presented hBN-encapsulated devices featuring graphene channel mobilities of 40000-60000 $\frac{cm^2}{Vs}$. In order to boost performance, they used a top electrolyte-gate and placed the WG in close proximity to the electrodes taking advantage of the fermi

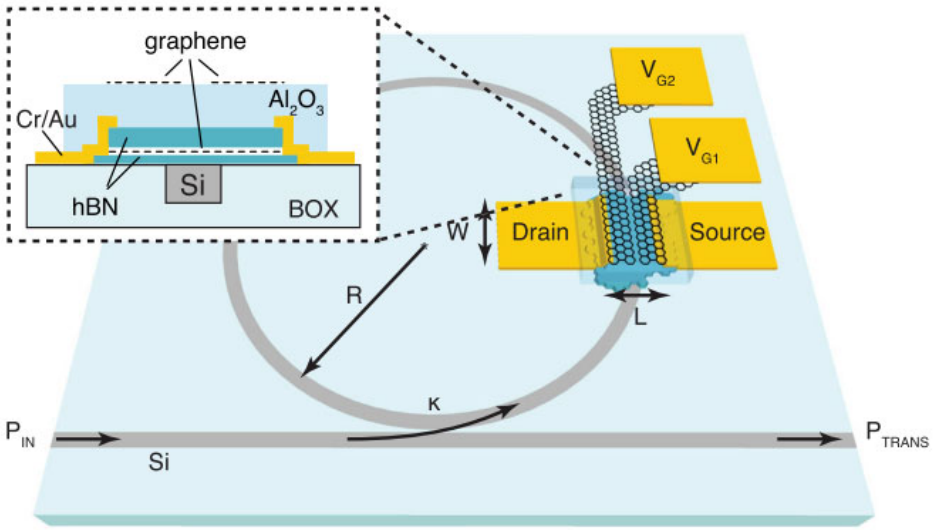

Figure 5.2 Light coupled from the bus WG is guided to the graphene PD. The photodetector uses a graphene split gate to control the Fermi energy in the channel. The incoming light constructively interferes to produce large electric field densities, boosting photodetection. [42]

level matching between channel and gate to induce a p-n junction, they reported a current responsivity exceeding 0.35 A/W [10] under biased operation. Other biased devices based on the photo-bolometric effect integrate along the waveguide plasmonic features like bowtie-shaped nanosized metallic structures. The in-plane electric fields couple evanescently to the graphene photodetector by exciting surface plasmon polaritons in the bowtie-shaped nanosized metallic structures focusing the light in a small area. They reported a responsivity of 0.6 A/W [11]. The most challenging frontier of graphene integrated photodetectors is unbiased operation as it yet lacks the ~ A/W responsivities enjoyed in other applications. Unbiased operation offers undeniable advantages on the limitation of dark current

and energy consumption driving interest in the scientific community. Asymmetric waveguide devices [12] explored in theoretical studies showed that taking full advantage of plasmonic enhancement can yield current responsivities of ~ 0.7 A/W in an unbiased configuration. Split-gate device architectures recently realized leverage tunability to improve performance while being versatile in manufacturing, with device architectures often not requiring sub 100 nm nanostructures. Graphene split gate PD on passive photonic waveguides were reported to reach RV ~ 3.5 V/W by Marconi et al and 5 V/W by Miseikis et al [4], [13]. Muench et al showed that light coupled from a Si_3N_4 WG to a plasmonic slot WG, ~100 nm in dimensions, situated in close proximity atop the graphene channel generates strong evanescent electromagnetic fields. The confinement of light generates high temperature gradients that benefit from the metal arms acting as electrostatic gates. The device yielded results of RV ~12 V/W [3]. Schuler et al used looped WGs known as micro-ring resonators which act as PIC-embedded resonant cavities combined with split gate graphene electrostatic gating achieving RV ~ 90 V/W. The resonator enables higher (compared to the bus WG) intra-cavity energy density due to interference resulting in a 10-fold enhancement of light-matter interaction and a >90% total light absorption effectively curbing transmission losses whilst maintaining small channel length size [14].

2 Graphene Theory

2.1 Electronic band structure

Graphene is a carbon allotrope forming a 2D crystal of atomic thickness [15] with extraordinary mechanical, optical, electronic and thermal properties. Carbon, C_6 is a very important element of the periodic often called the element of life for it' s ability to form organic compounds. The electronic structure of carbon is $1s^2 2s^2 2p^2$, that means that carbon has 4 unoccupied orbitals available for hybridization and bond forming. Different types of orbital mixing result in different molecular structures of carbon like graphite, diamond, carbon nano tubes with different material and electronic properties figure 2.1.

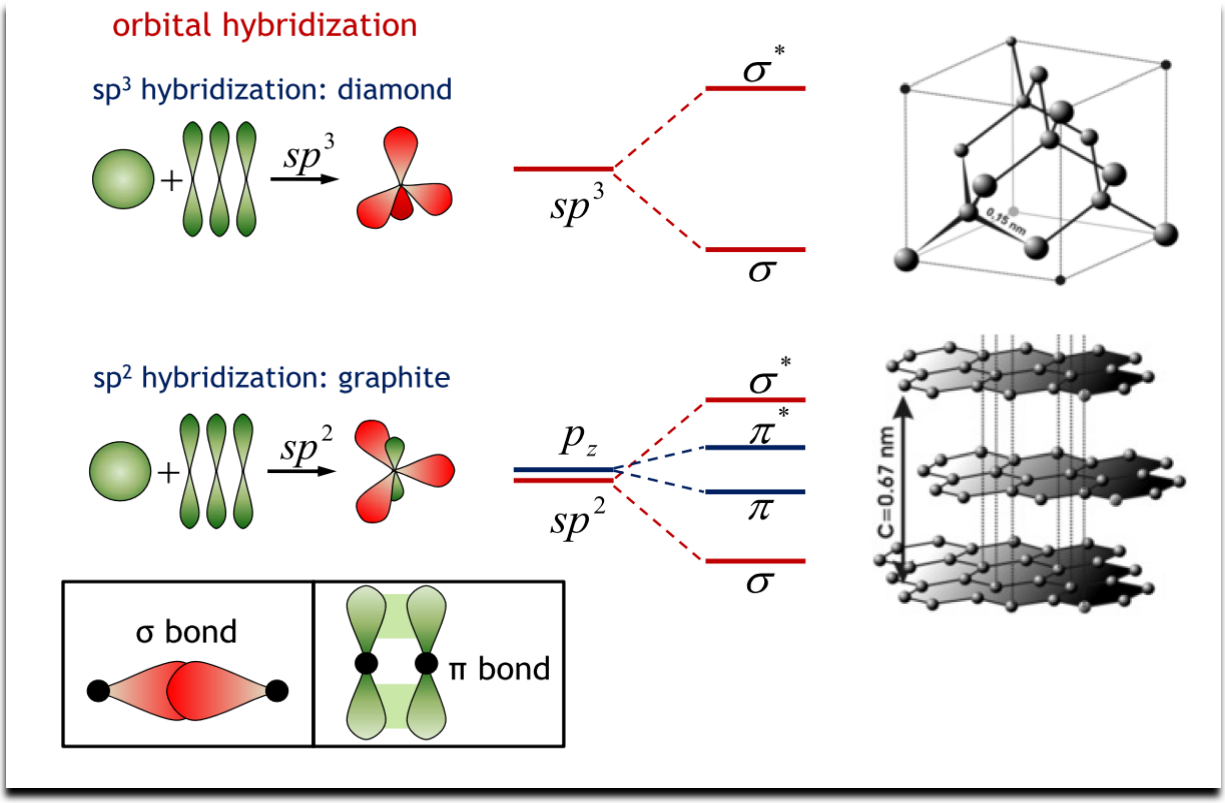

Figure 2.1 Hybridization of different carbon allotropes

First attempt of explaining the electronic band structure of graphene came from Wallace [16] as an approximation in the treatment of graphite by neglecting the interactions between planes, and supposing that conduction takes place only in layers. The 2D crystal lattice geometry resembles that of a honeycomb in both real figure 2.2a and reciprocal figure 2.2b lattice. Sg, Σg are the unit cells in

real and reciprocal space along with their corresponding lattice vectors $\boldsymbol{a_i}$, $\boldsymbol{b_i}$, $a_0 = \sqrt{3}\, b$, $b = 1.42$ Å where b is the C-C distance and Ag, Bg is the unit cell volume[2D].

Three of its four valence electrons form tight bonds with the neighboring atoms leaving one electron in the p_z orbital free for conduction. In the nearest neighbors tight binding approximation, the energy

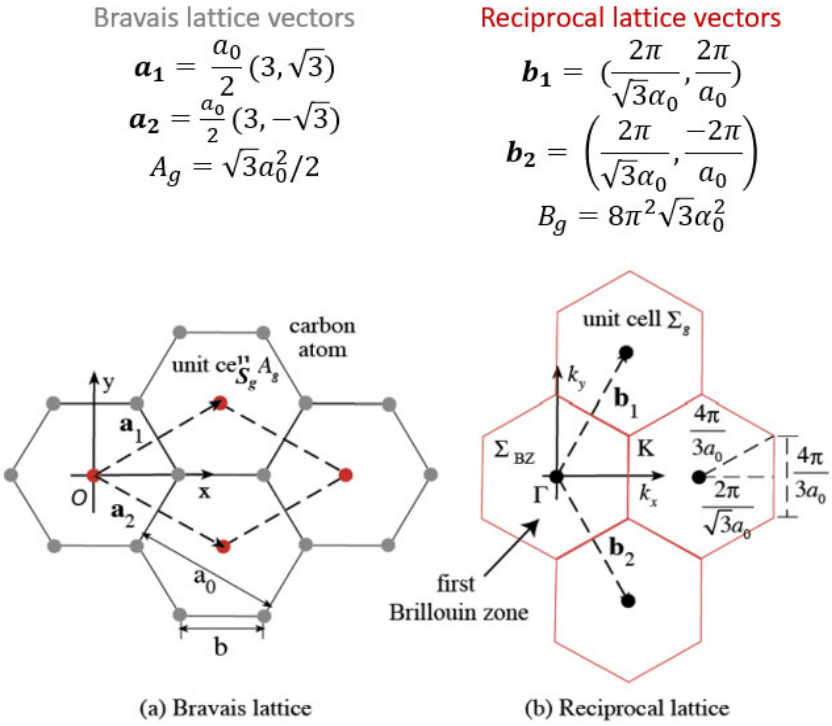

Figure 2.3 a) Real and b) reciprocal space unit cells and lattice vectors. [3]

dispersion relation for these conduction electrons is given by eq 2.1

$$E^{\pm}(\boldsymbol{k}) \pm \gamma \left[1 + 4\cos\left(\frac{\sqrt{3}k_x a_0}{2}\right)\cos\left(\frac{k_y a_0}{2}\right) + 4cos^2\left(\frac{k_y a_0}{2}\right)\right]^{\frac{1}{2}} \qquad (2.1)$$

Where $\pm$ is upper/lower band and $\gamma = 2.7\ eV$ is the carbon – carbon interaction energy [17]. The dispersion relation exhibits the hexagonal symmetry of the reciprocal unit cell figure 2.3 with the upper band touching the lower band at 6 different points called Fermi/Dirac points, forming a hexagon. Since each cell has two carbon atoms and each carbon atom contributes one electron at each band the

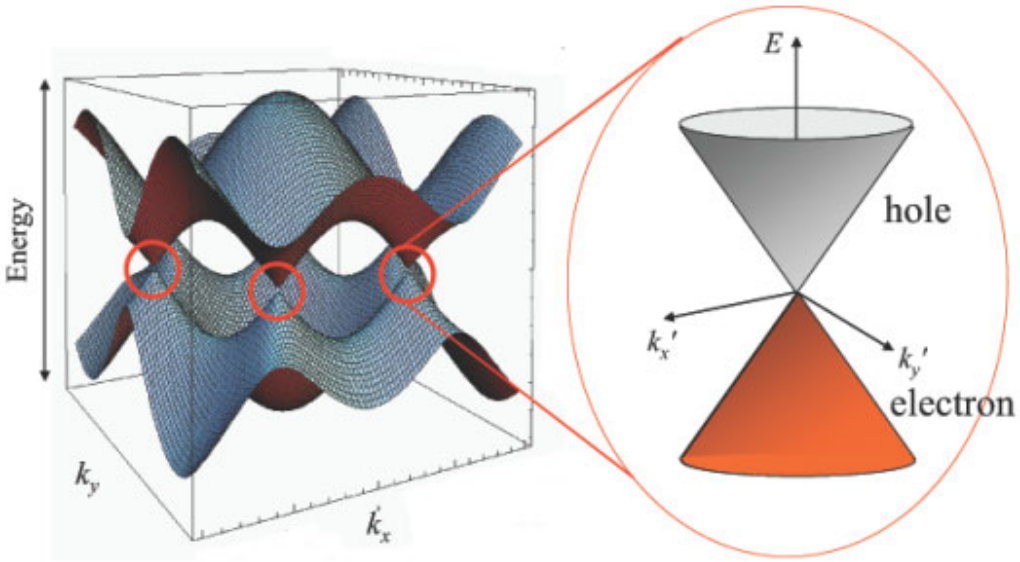

Figure 2.4 Band structure of graphene. Liner energy dispersion relation near the Dirac points [5]

fermi energy would land at the middle, this means that the upper band serves as a conduction band and the lower as a valence band. For an ideal graphene crystal this point would coincide with the charge neutrality point CNP. Even though graphene is not technically a semiconductor it is often called a zero-gap semiconductor because of its almost zero density of states (low conductivity) near Dirac points. If we expand the dispersion relation near the Dirac point $\boldsymbol{k_0}$, we get a linear dispersion relation eq 2.2.

$$E^{\pm} \sim \pm \hbar V_F \, q \;,\; q \;=\; |\boldsymbol{k} - \boldsymbol{k}_0| \,,\; V_F = 10^6 \, m/s \qquad (2.2)$$

The quasiparticles in graphene obey the Dirac rather than the Schrodinger equation and this has profound implications for their dynamics [18]. Their behavior was experimentally confirmed by groups around the world including Geim and Kim [19] who created Field effect transistor devices with graphene crystals and measured the conductivity curves σ(n) under strong magnetic field and low temperatures [20]. These revealed a half integer quantization of the conductivity (unconventional quantum hall effect) similar to the energy spectrum of fermions in quantized magnetic fields. From the single electron energy, we need a multiparticle model to account the total energy. Considering the electrons in the conduction/valence band behave like quasi free particles in a box figure 2.4, the wavefunction can be written as eq 2.3.

$$\Psi(x, y, z) = \sin(k_x x)\sin(k_y y) \;\; k_x = \frac{n\pi}{L_x}, k_y = \frac{n\pi}{L_y} \qquad (2.3)$$

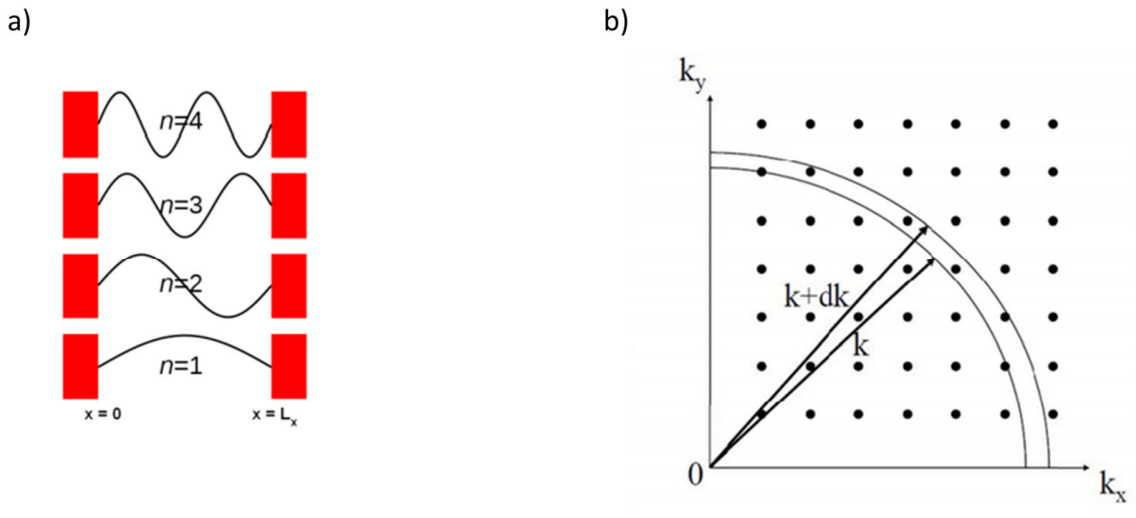

Figure 2.5 a) Particle in a box wavefunction b) 2D k space shell

The density of states is given by the number of allowed electrons/holes states per unit volume at a given energy. The allowed states are separated by $\frac{\pi}{L_{x,y}}$ so each state occupies $volume^{2D} = (\frac{\pi}{L_x L_y})^2$ If the total $volume^{2D}$ is A then the number of states per unit volume is $\frac{A}{\pi^2}$ .The number of states available for a given k are the states inside a shell of thickness dk at radius $|\mathbf{k}|$ eq 2.4. There is also a factor of ¼ due to unaccounted degeneracy of the +/- states of the wavefunction, a factor of 2 due to spin and a factor of 2 due to valley pseudospin. If we know the dispersion relation, we can the derive the density of states in terms of energy and calculate the electron density eq 2.5

$$g(k)\,dk = \frac{1}{4}\,2\,2\left[\frac{A}{\pi^2}\right]\,2\pi k\,dk, k = \frac{E}{\hbar V_F}\,dk = \frac{dE}{\hbar V_F} \quad (2.4)$$

$$g(\varepsilon) = \frac{2|\varepsilon|}{\pi\hbar^2 V_F^2},\; n = \frac{2}{\pi}\int_0^{E_F} g(\varepsilon)\,d\varepsilon = \frac{E_F^2}{\pi\hbar^2 V_F^2} \quad (2.5)$$

2.2 Electrical conductivity and optical absorption

Graphene is often called a two-dimensional gapless semiconductor with low doping EF ~ 0 acting as the nonconductive state, low density of states nearby, and high doping as the conductive one. Studied at low temperatures, graphene's conductivity has been shown to reach a minimum value with the prevalent mechanism of carrier relaxation being the presence of impurities [21]. Carrier density and Fermi energy can be controlled at the device level using electrostatic gating. At room temperatures the thermodynamic quantities are being described by averaged quantities like the average

energy using the fermi- Dirac statistical distribution eq 2.6. Since we know the fermi energy of graphene from the capacitor model, the chemical potential can be obtained by solving equation 2.7, code for all calculations provided in the appendix. The electrical conductivity can then be calculated from eq (2.8).

$$f(\varepsilon,\mu,T)=\frac{1}{e^{\frac{\varepsilon-\mu}{k_bT}}+1} \quad (2.6)$$

$$\int_0^\infty g(\varepsilon)\,[f(\varepsilon,\mu,T)-f(\varepsilon,-\mu,T)]\,d\varepsilon=\frac{E_F^2}{\pi\hbar^2V_F^2} \quad (2.7)$$

$$\sigma(\mu,T)=\int_{-\infty}^{\infty}\sigma(\varepsilon)\partial_\varepsilon f(\varepsilon,\mu,T)d_\varepsilon \quad (2.8)$$

Where $\sigma(\varepsilon)=q\mu_e n_{eff},\ n_{eff}=n(\varepsilon)\sqrt{1+\frac{n_0^2}{n(\varepsilon)^2}}$, $n(\varepsilon)=\frac{\varepsilon^2}{\pi\hbar^2V_F^2}$ with q being the elementary charge $\mu_e{\sim}10^4\,\frac{cm^2}{V}$ the mobility of electrons/holes assuming symmetric values and $n_0{\sim}\,10^{11}\,cm^{-2}$ [22] is the residual charge due to impurities, deformations and interactions with the substrate. Graphene's optical properties are essentially described by the transfer of energy from photons to electrons and are thus intimately linked to it' s electronic properties. For the optical properties graphene is modeled as an infinitesimally thin conductive layer with a surface conductivity

$$\sigma(\omega,\mu_c,\Gamma,T)=\frac{\iota e^2(\omega-2i\Gamma)}{\pi\hbar^2}\{\frac{1}{(\omega+2i\Gamma)^2}\int_0^\infty\varepsilon\big(\partial_\varepsilon f(\varepsilon)-\partial_\varepsilon f(-\varepsilon)\big)d\varepsilon-\int_0^\infty\frac{f(\varepsilon)-f(-\varepsilon)}{(\omega+2i\Gamma)^2-4\left(\frac{\varepsilon}{\hbar}\right)^2}d\varepsilon\} \quad (2.9)$$

eq 2.9. Where ω is the frequency of the incoming photons, μ_c is the equilibrium chemical potential, Γ is the electron-electron scattering rate and T is the electronic temperature [18], [21], [23]. The first term is due to intra-band transitions and the second due to inter-band figure 2.5. We can intuitively understand the mechanics of this equation by considering the individual terms inside the integral. The inter-band term describes the probability of absorbing-emitting a photon of energy $\hbar\omega$. This process is equivalent to the product of two probabilities: a state to be occupied in the conduction band $P_c{\sim}f\left(\frac{\hbar\omega}{2},\mu,T\right)$ and simultaneously a sate to be unoccupied in the valence band $P_v{\sim}1-f(-\frac{\hbar\omega}{2},\mu,T)$, the net probability for a photon to be absorbed follows the proportionality relation eq 2.10.

$$P_{abs}{\sim}f\left(\frac{\hbar\omega}{2},\mu,T\right)\left(1-f\left(-\frac{\hbar\omega}{2},\mu,T\right)\right) \quad (2.10)$$

$$P_{em}{\sim}\,f\left(-\frac{\hbar\omega}{2},\mu,T\right)\left(1-f\left(\frac{\hbar\omega}{2},\mu,T\right)\right) \quad (2.11)$$

At the same time electrons of higher energies will try to lower their energy by emitting a photon and

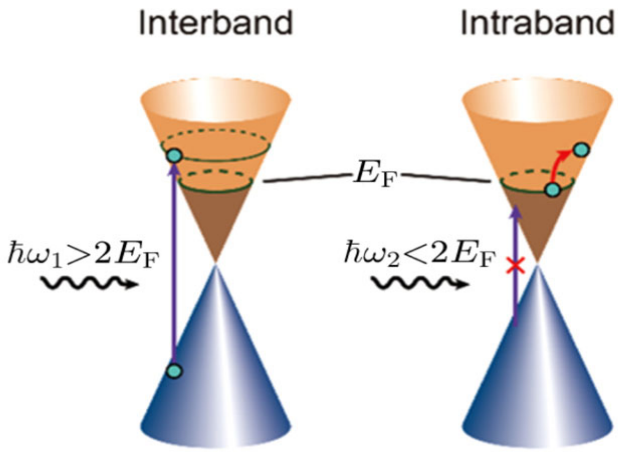

Figure 2.5 Inter-band and intra-band transitions for doped graphene. Pauli blocking for photon energies $\hbar\omega < 2\,E_F$.

occupy those empty states at the valence band eq 2.11. When those two processes reach equilibrium, the net absorption will be proportional to the difference in probabilities eq 2.12. The intra-band terms

$$P_{net} \sim P_{abs} - P_{em} \sim f(\varepsilon,\mu,T) - f(\varepsilon,\mu,T) \quad (2.12)$$

can be thought as the accessibility of empty states near the chemical potential or the highest energy occupied states. The expression can be written as $\int_0^\infty g(\varepsilon)\partial_\varepsilon f(\varepsilon,\mu,T)d\varepsilon$ for the electrons and $\int_0^\infty g(\varepsilon)\partial_\varepsilon\big(1-f(\varepsilon,\mu,T)\big)d\varepsilon = -\int_0^\infty g(\varepsilon)\partial_\varepsilon f(-\varepsilon,\mu,T)d\varepsilon$ for the holes. In the long wavelength $k \ll \frac{1}{t_{gr}}$ where $t_{gr} \sim 0.335\,nm$ is the graphene layer thickness and k the wavenumber, the equivalent bulk dielectric function is given by 2.13 and the absorbed optical power by 2.14.

$$\varepsilon = 1 + \frac{i\sigma}{\varepsilon_0 \omega t_{gr}} \quad (2.13)$$

$$P_{abs} = -0.5\omega|E|^2 Im(\varepsilon) \quad (2.14)$$

Experimental data support the accuracy of this model both in the visible [24] and in the infrared [25] figure 2.6. In the UV we have the Van Hove peak manifesting in a resonant manner as the energy of photons approaches the value of the hoping energy 2.8 eV. In the visible-near IR graphene exhibits universal conductance associated with a flat absorption of α ~ 2%. As we move deeper in the IR

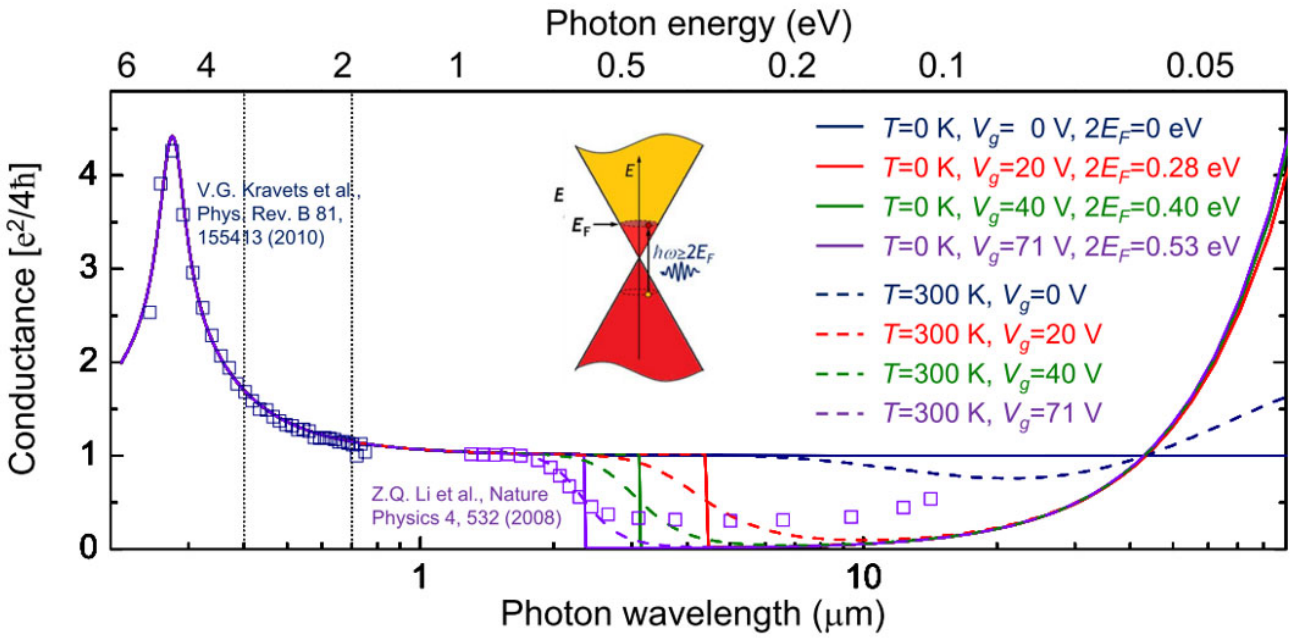

Figure 2.6 Real part of the surface conductivity for different temperatures and Fermi energies compared to experimental data.

spectrum, Pauli blocking takes effect reducing the conductivity, a direct consequence of the Pauli exclusion principle. Finally in the far IR we have Drude free electron conductance between neighboring states and the conductivity rises again figure 2.6.

3 Photonics

3.1 Waveguides for integrated photonics

Among optical waveguides (WG) only a few structures such as slab waveguides and step index optical fibers can be solved analytically. For more complex structures such as rectangular waveguides figure 3.1 often used in photonic integrated circuits numerical methods must be used to obtain a solution. Analysis begins by solving Maxwell's equation in the frequency domain using Lumerical [26] finite difference mode eigen solver (FDE) in a cross section (x-y plane) of the waveguide calculating the spatial profile of the fields and effective index (neff) of the quasi-TE and quasi-TM modes supported by the waveguide cavity. The fields are assumed to have a vector field form $E(x,y)\,e^{-i(\omega t-\beta z)}$, $H(x,y)e^{-i(\omega t+\beta z)}$ where ω is the angular frequency and β is the propagation constant. The mode effective index is given by $n_{eff} = \frac{c\,\beta}{\omega}$ where c is the speed of light. From the mode profiles of the electric field a qualitative description of the mode confinement can be observed.

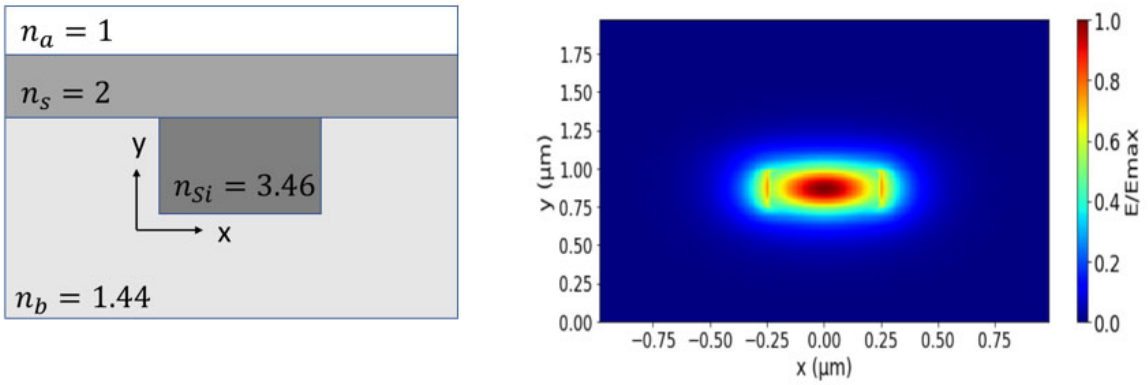

Figure 3.1 Geometric representation of a rectangular Si WG embedded in a SiO2 substrate with a Si3N4 dielectric spacer superstrate (left). Fundamental TE mode electric field intensity heatmap (right)

A quantitative description of the interaction with the light absorbing materials can be obtained from the imaginary part of the effective index. The shortcomings of this method are that in a device with multiple absorbing material (gates, contacts, active layer graphene) the loss is described by the imaginary part of the effective index and cannot be accounted for each individual absorbing material. Another thing to consider is effects like scattering losses or reflections at material interfaces also remain completely unaccounted for. To address these problems, we perform 3D FDTD simulations

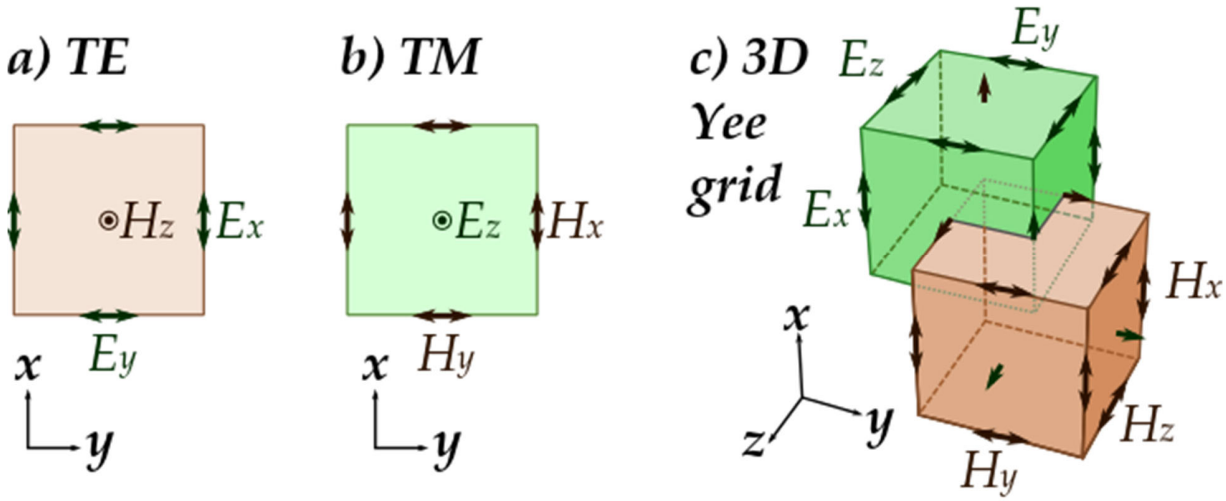

Figure 3.2 a) TE and b) TM electric and magnetic field components relevant to the face of a Yee cell c) Yee grid visualized as interpenetrating cubic voxels, the electric field components form at the edges of the cube while the magnetic field components form at the center of the faces of the cube.

(Lumerical) which is considered the state-of-the-art modeling method for solving Maxwell's equations on complex geometries.

3.2 Finite difference time domain method

The finite difference time domain FDTD algorithm solves Maxwell's curl equations for the electric and magnetic fields $\boldsymbol{B} = \mu\, \boldsymbol{H} = \mu_r\, \mu_0 \boldsymbol{H},\ \boldsymbol{D} = \varepsilon \boldsymbol{E} = \varepsilon_r \varepsilon_0 \boldsymbol{E}$. In the case of isotropic non-magnetic media absent of current and magnetism sources the equations take the form of eq 3.1.

$$\nabla \times \boldsymbol{H} = \frac{\partial \boldsymbol{D}}{\partial t} + \sigma \boldsymbol{E},\ \ \boldsymbol{D} = \varepsilon_0 \varepsilon_r \boldsymbol{E},\ \ \nabla \times \boldsymbol{E} = -\mu_0 \frac{\partial \boldsymbol{H}}{\partial t} \qquad (3.1)$$

Where $\varepsilon_r(x, y, z, \omega)$ is the dielectric permittivity and $\sigma(x, y, z, \omega)$ the electrical conductivity both being functions of position based on the material model. The system of six coupled partial differential equations forms the basis of the FDTD numerical algorithm. The FDTD method solves for the fields in a spatially and temporally discretized space, $(i\Delta x, j\Delta y, k\Delta z, n\Delta t)$ where (i, j, k, n) integers and $(\Delta x, \Delta y, \Delta z, \Delta t)$ step size, populated by Yee cells figure 3.2 [27]. The Yee cells serve as the minimum unit of space where all field components, functions of space and time $A(i\Delta x, j\Delta y, k\Delta z, n\Delta t)$, are defined. This is because the Yee algorithm [28] centers its E and H components so that every E component is surrounded by four circulating H components and every H component is surrounded by four circulating E components meaning that at any given point in space, we can know exactly only part of the fields. Using a central difference approximation for the derivatives finite deference

expressions can be derived for all the field components $(E_x, E_y, E_z, H_x, H_y, H_z)$. For example, for E_x field it is written as eq 3.2.

$$\frac{E^x_{i,j+\frac{1}{2},k+\frac{1}{2},n+\frac{1}{2}} - E^x_{i,j+\frac{1}{2},k+\frac{1}{2},n+\frac{1}{2}}}{\Delta t} = \frac{1}{\varepsilon_{i,j+\frac{1}{2},k+\frac{1}{2}}} \cdot \left[\frac{H^z_{i,j+1,k+\frac{1}{2},n} H^z_{i,j,k+\frac{1}{2},n}}{\Delta y} - \frac{H^z_{i,j+\frac{1}{2},k+1,n} H^z_{i,j+\frac{1}{2},k,n}}{\Delta z} - \sigma_{i,j+\frac{1}{2},k+\frac{1}{2}} \cdot \frac{E^x_{i,j+\frac{1}{2},k+\frac{1}{2},n+\frac{1}{2}} + E^x_{i,j+\frac{1}{2},k+\frac{1}{2},n-\frac{1}{2}}}{2}\right] \qquad (3.2)$$

Collecting all the terms and rearranging for $E^x_{i,j+\frac{1}{2},k+\frac{1}{2},n+\frac{1}{2}}$ yields the explicit time stepping equations. Similarly, we can derive equations for all other field components of E and H. Now the new values of an electromagnetic field vector component depend only on the values of other field vector components at adjacent points and the computation can procced in a leapfrog manner [27]. After the simulation completes all fields are Fourier transformed to get the frequency-wavelength response of the optical absorption since we are interested in a particular wavelength. For the source of the simulation, we use the fundamental TE mode at λ = 1550 nm found in previous 2D mode analysis of the WG cross section. For the boundary conditions perfectly matched layers (PML) are used to decay the fields as we move away from the region of interest. The simulation terminates when the fields inside the simulation box have decayed beyond some predetermined tolerance. While performing the simulation it is important to choose small enough step size (dx, dy, dz), smaller than the wavelength $\sqrt{\Delta x^2 + \Delta y^2 + \Delta z^2} < c\Delta t$ for the algorithm to be computationally stable. The way to estimate a step size that optimizes both performance and accuracy is to run simulations with ever decreasing step size until the macro quantities of interest converge.

3.3 Light-matter interaction modeling

Nanoscale structures made of conducting material embedded in dielectric media enable optical electromagnetic wave propagation that is locally confined to a metal–dielectric interface. This confinement of light enhances the electric field leading to a plethora of applications including antennas, sensors, resonators and waveguides able to manipulate light beyond the diffraction limit. At near-infrared and visible optical wavelengths, the frequency-dependent relative permittivity $\varepsilon_r(\omega)$ can be described by a Lorentz-Drude model eq 3.3.

$$\varepsilon_r(\omega) = \varepsilon_\infty - \frac{\omega_{pD}^2}{\omega^2 - j\omega\Gamma_D} + \frac{\omega_{pL}^2 \Delta\varepsilon_L}{\omega_L^2 - \omega^2 + j\omega\Gamma_L} \qquad (3.3)$$

Where ω_{pD} is the plasma frequency, Γ_D is the damping coefficient for the Drude model, $\Delta\varepsilon_L$ is a weighting factor, ω_{pL} is the resonance frequency and Γ_L the spectral width of the resonance. Away from resonances we can model the dielectric function of plasmonic material with polynomials fitted using literature data [29] figure 3.3. This allows to obtain a more accurate description of the dielectric index as a function of frequency at the particular spectral range of interest. In non-conducting material the dielectric material model sets the refractive index at a real constant value. This approximation is valid for dielectric material with almost zero dispersion at the wavelength of interest (λ ~1.55 μm). The dielectric index strength for the material used is chosen from experimental values [30]–[32]

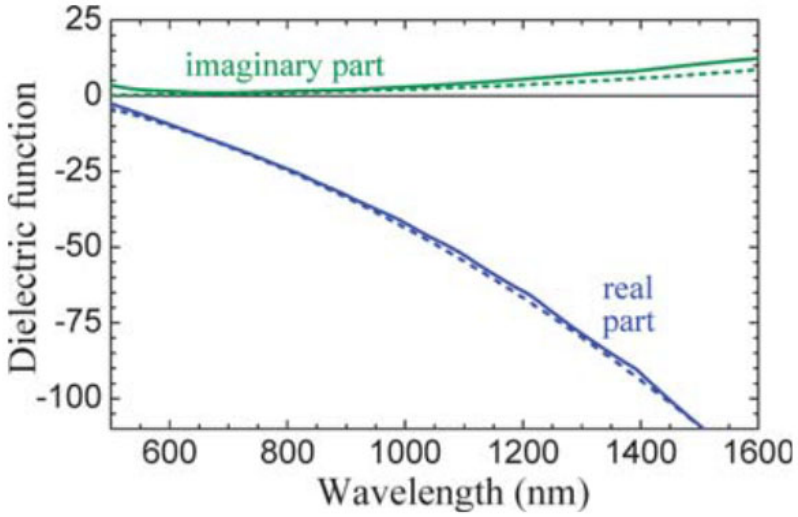

Figure 3.3 Dielectric function of gold taken from [Johnson1972] (solid curves) and compared with the Drude model approximation (dashed curves). [Myroshnychenko2008]

$$n_{Si} = 3.47, n_{SiO_2} = 1.44,\ n_{Si_3N_4} = 2, n_{Al_2O_3} = 1.74,\ n_{Au} = 0.53,\ k_{Au} = 10.81\ at\ \lambda = 1550\ nm\ .$$

For graphene we follow the approach of the surface conductivity σ [23] model explained in detail in previous a chapter about graphene under the optical properties section. In order to use the 2D surface conductivity expression in a 3D FDTD simulation an equivalent volumetric permittivity model is required. To turn the surface conductivity of a graphene layer into a uniaxial anisotropic permittivity, two additional parameters must be therefore introduced: Δ the layer thickness and ε_r the background relative permittivity index. Using these two parameters, the two parallel (or in-plane) components and the perpendicular (or out-of-plane) component of the permittivity tensor are given by

$$\varepsilon_{\parallel}(\omega, \Gamma, \mu_c, T) = \varepsilon_r + i\frac{\sigma(\omega,\Gamma,\mu_c,T)}{\varepsilon_0 \omega \Delta}\ ,\ \varepsilon_{\perp} = \varepsilon_r \qquad (3.4)$$

Where ω is the angular frequency Γ the scattering rate, μ_c the equilibrium chemical potential and T the electronic temperature. The above uniaxial anisotropic material description can be introduced into a simulation in FDTD.

3.4 Photonic-plasmonic coupling methods

Plasmonic waveguides achieve wave propagation that is characterized by small modal sizes, of the order of their slot dimensions, characterized by light confinement beyond the diffraction limit and high propagation losses. To harness this high intensity light for photodetection applications in photonic integrated circuits PICs, co-integration with low loss dielectric waveguides is required to mitigate the excessive optical loss coming from plasmonic structures while fully exploiting their functional benefits [33], [34]. We will investigate coupling solutions for graphene photodetection applications on hybrid dielectric-plasmonic waveguide platforms. The basic principles of directional

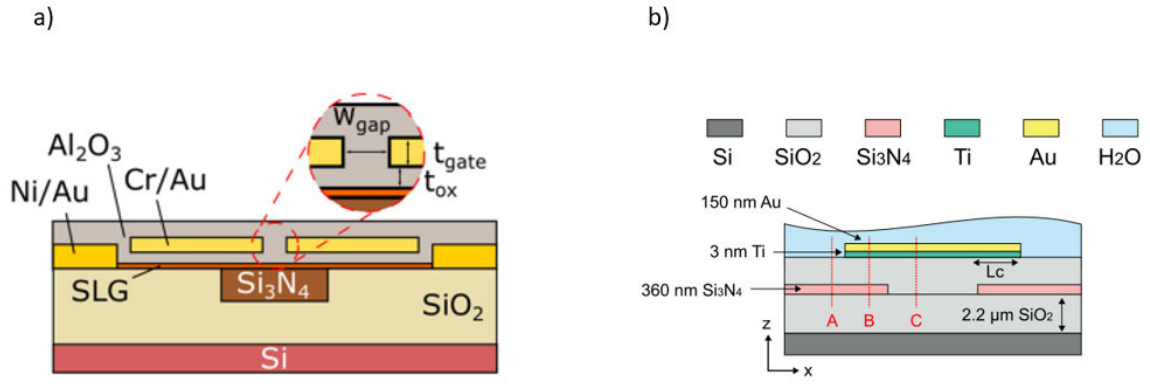

Figure 3.4 a) Depiction of the hybrid region for a Si_3N_4 embedded in SiO_2 dielectric with Au - Al_2O_3- Au MIM plasmonic slot WG system used in photodetection applications [3]. b) Side view of a Si_3N_4 embedded in SiO_2 with Au - H_2O- Au plasmonic slot WG coupling scheme [33]. The space is partitioned in three regions A dielectric, B hybrid and C plasmonic.

coupling are presented here while the actual implementation on the particular device geometry is presented alongside the results of this thesis. Coupling between two waveguiding structures is in general the process where the light propagation is transferred from one wave guiding structure to another. The success of this process is accessed by figures of merit such as the insertion loss $IL =$

$-10\log(\frac{T}{I})$ and coupling efficiency $CE = \frac{T}{I}$ where I, T are the source normalized incident and transmitted powers. The coupling strategies employed are application dependent and exhibit a range of CEs. The plasmonic waveguide is comprised of metal-insulator-metal MIM often called simply slot waveguide with small cross-section of the order of ~100 nm. The small WG cross-section is crucial as it squeezes the light, offering strong evanescent fields ideal for graphene photodetection applications. This kind of structures have been realized experimentally in the case of Si_3N_4 WG using gold and Al_2O_3 in the metal-insulator-metal MIM slot waveguide configuration employing taper assisted vertical coupling by Muench et al [3] figure 3.4a for photodetection or by using water as the cladding insulator employing vertical directional coupling by Dabos et al figure 3.4b for bio-sensing [33].Taper assisted end to end alignment has demonstrated a 0.6 dB insertion loss in similar Si-plasmonic [35] and Si-hybrid couplers [36]. WG tapering methods complicate fabrication requirements while offering similar coupling efficiencies with optimized vertical coupling strategies. For the Si WG there have been examples of vertical directional coupling in plasmonic ferroelectric optical modulation applications [37] with some of the advantages being ease of fabrication and low insertion losses, of the order of 1.4 dB as reported in li et al [34].

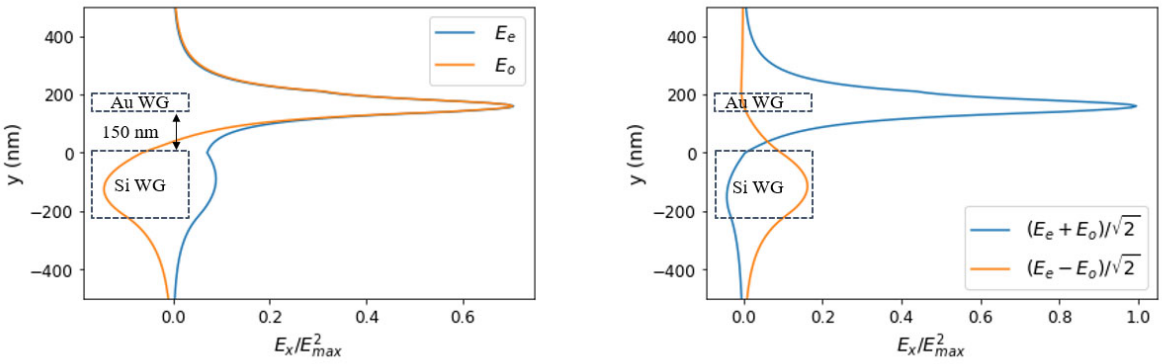

Figure 3.5 Hybrid region for Si- Au slot WG in the vertical coupling scheme for Hc = 150nm. Left figure shows the primary electric field component (Ex) for the eigenmodes along the vertical y direction at x = 0, normalized with $|E_{max}|^2$, exhibiting even and odd symmetry with respect to the xz plane. Right figure showing qualitatively how localized states can be formed in either WG by superposition of the eigenmodes.

The physics of light energy being transferred from one structure to another aren't so intuitive as the end-to-end alignment. The device can be sectioned in three distinct regions based on the structures present. Those are I dielectric, II hybrid and III plasmonic figure 3.4b. Initially a parametric sweep is needed in regions I, III varying the geometric features of both WGs calculating the corresponding the

effective indices eventually adopting geometrical features that map both structures to a common effective index. When the vertical separation distance, commonly referred to as coupling height Hc, in the hybrid region tends to infinity the electric field is either in the initial Ψ_I or final state Ψ_{III}. For intermediate coupling heights the general solution in the hybrid region is a superposition of even and odd eigenmodes $\Psi_{II} = C_1 \Psi_e + C_2 \Psi_o$, having a propagation constant $\beta_{e,o} = \frac{2\pi n_{e.o}}{\lambda_0}$. The even and odd refer to the symmetry of the two eigenmode fields with respect to the halfplane separating the two WG structures figure 3.5. As the orthogonal modes propagate in the hybrid region their relative phase changes. In order to maximize the field strength at the plasmonic WG the two states must be in constructive interference above the halfplane and this is achieved for a difference of phase π between the two, eq 3.5 enforces this rule by prescribing the propagation length in the hybrid region.

$$L_c^{Th} = \frac{\pi}{\Delta\beta},\ \Delta\beta = \beta_e - \beta_o \qquad (3.5)$$

Thus, to achieve maximum coupling efficiency for a given Hc we have to engineer the length of this overlap region commonly referred to as coupling length such that it abruptly ends at that point where this condition is satisfied. In reality this is an ideal case as we have phenomena such as reflections from the wave traveling from region II to III and imperfect constructive-destructive interference so the actual optimal point of coupling will be eventually determined by 3D FDTD simulations and the theoretical coupling length shall be used as a rough estimate.

4 Electrostatics

4.1 Gating architecture

The split gate architecture allows for the independent control of the surface charge density and in extension the fermi energy in the left-right half of the channel figure 4.1. Since the thermodynamic quantities of graphene (Seebeck, thermal-electrical conductivity, electronic heat capacity) are a function of fermi energy affecting the photo thermoelectric effect responsible for current generation it is important to know the exact form of the fermi energy inside the channel.

4.2 Poisson equation

Electrostatics refers to the branch of electromagnetic theory that deals with static charge

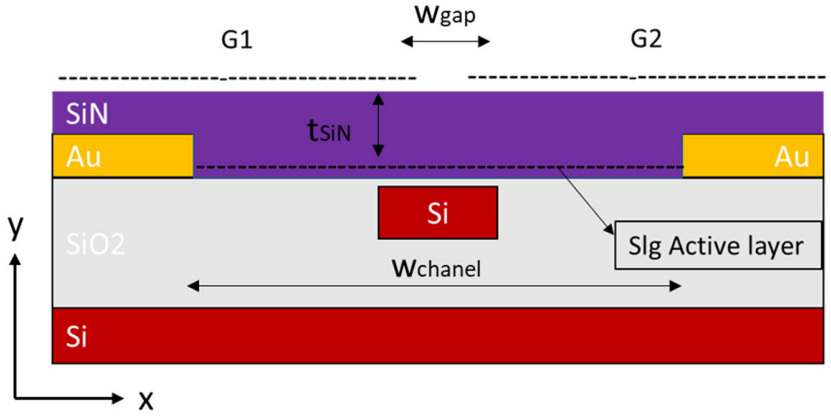

Figure 4.1 Front view of a device with graphene gates and Si_3N_4 as the gate dielectric. The two gates $G_{1,2}$ can independently control the voltage in the left/right half of the channel away from the gap.

distributions, such is the case when we apply voltage difference between two graphene sheets. A positive surface charge distribution is created in one sheet and a negative one in the other. In the simplest of cases (two parallel graphene sheets) the parallel plate capacitor is a very good approximation, for more complex geometries a common approach is to solve for the potential forfeiting some degrees of freedom for the problem to admit to a solution. The electric field can be written as the divergence of a scalar potential $\boldsymbol{E} = -\boldsymbol{\nabla} V$. This is a special case of the more general Helmholtz theorem for the decomposition of a vector field combined with the fact that $\mathbf{E}$ is a conservative field $\nabla \times \mathbf{E} = \mathbf{0}$. We also know that in dielectric media such as the oxide layers, charges are induced due to polarization and in the linear approximation (low intensity fields) this is

proportional to the external electric field $\boldsymbol{P} = x_e\, \boldsymbol{E}$. The total field inside the material is called displacement $\boldsymbol{D} = (1 + x_e)$ E. We can write Gauss's law as eq 4.1. Inside a uniform medium eq 4.1 transforms to eq 4.2 namely the Poisson equation.

$$\nabla \boldsymbol{E} = \frac{\rho}{\varepsilon_r \varepsilon_0} \rightarrow \nabla(-\varepsilon_0 \varepsilon_r \nabla V) = \rho \quad (4.1)$$

$$\nabla^2 V = \frac{\rho}{\varepsilon_r \varepsilon_0} \quad (4.2)$$

In general, ρ is a function of space f (x, y, z). In this specific problem we do not know the surface charge distribution at the graphene gates but we do know the solution to the potential. We also know that there are no free charges at the rest of the materials so the equation reduces to the Laplace $\nabla^2 V = 0$ everywhere else. To get the fermi energy we need to obtain the surface charge density σ from eq 4.3 by enforcing the boundary conditions for the displacement field at the gate-dielectric interface and use the 2D energy-charge density relation eq 4.4

$$\boldsymbol{n}\,(\boldsymbol{D}_2 - \boldsymbol{D}_1) = \sigma \quad (4.3)$$

$$\sigma = \frac{E_F^2}{\pi V_F^2 \hbar^2} \quad (4.4).$$

4.3 Semi - analytic solution method

Away from the gap $|x| \gg \frac{w_{gap}}{2}$ the field resembles that of the infinite parallel plate capacitor and an analytic solution can be obtained as $Q = C\, V_g\,, e\sigma = \frac{\varepsilon_0 \varepsilon_r V_g}{t_{SiN}}$. The Fermi energy will then be $E_F = \hbar V_F \sqrt{\frac{\pi \varepsilon_0 \varepsilon_r V_g}{e}}$. Close to the gap, the problem can be solved numerically. For this purpose, an equivalent mathematical model is created for the device geometry and boundary conditions are prescribed at the ends of the computational box. The solution should converge to the analytic one at the left and right edges. At the left-right boundary points figure 4.2 Von Neuman boundary conditions $\frac{\partial V}{\partial n} = 0$ are used, while at the top-bottom Dirichlet $V = 0$ so that the solution decays properly. The equation can be solved in 2D due to symmetry reducing to $\nabla^2 V = V(x, y)$ using discretized finite difference approximation for the derivatives. After some algebra we arrive at the final expression for the voltage true for any point i, j in space eq 4.5.

$$V_{i,j} = 0.25\,(V_{i+1,j} + V_{i,j+1} + V_{i-1,j} + V_{i,j-1}) \quad (4.5)$$

The solution is obtained by successively updating the values of the potential for every point in the grid until the solution stops changing within some margin of error. This is a very popular numerical method called relaxation because the solution converges (relaxes) at its true form. The code is presented in the appendix code section

4.4 Simulation

Running the algorithm with some typical geometric parameters reveals the form of the form of the electric field and potential figure 4.3. Away from the gap the potential decreases from the top gates to the bottom while the field remains constant both in direction and magnitude reminiscent of the infinite parallel plate capacitor solution. Closer to the gap the field is similar to that of a dipole field (because in this example we used opposite sign and equal magnitude voltages on the gates). Finally, now that we have the voltage everywhere we can generate the surface charge distributions and the fermi energy (figure 4.4).

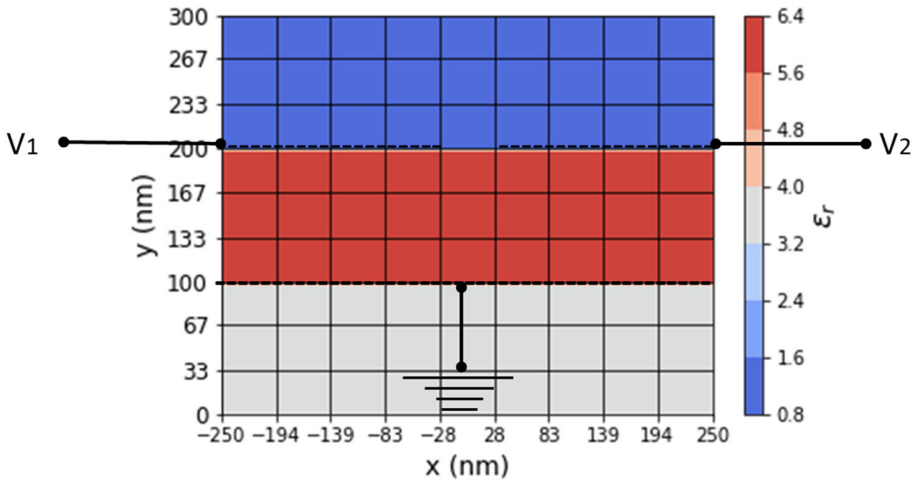

Figure 4.2 Mathematical model of space near the gap. The different material regions have different dielectric indices. Two different voltages are applied to the top gates while the bottom graphene is grounded.

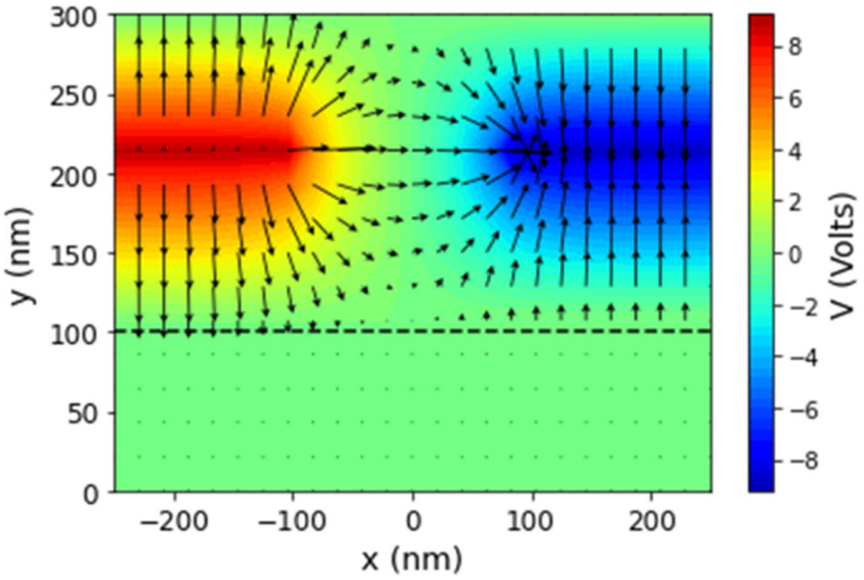

Figure 4.3 shows a computational box 500 x 300 nm, leaving d = 100 nm of free space between the top and bottom graphene sheets so that the fields properly. The gates are separated from the active layer by a dielectric spacer (Si_3N_4) 100 nm thick. The voltage applied to the gates VG1, VG2 correspond to fermi energies of EF1,2 = ± 0.2 eV. The color represents the magnitude of the potential while the arrows represent the direction and magnitude of the electric field.

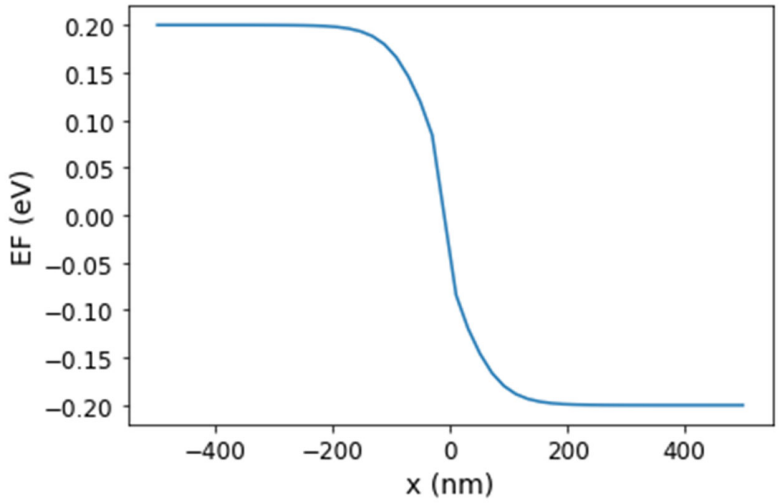

Figure 4.4 shows the Fermi energy distribution across the source-drain direction.

5 Thermoelectrics

5.1 Photo-thermo-electric phenomenon

The photo-thermo-electric effect (PTE) is the dominant current generating mechanism that characterizes the photo-response of graphene [38]–[42]. Multi-carrier production results from impact ionization and Auger-type processes induced by photoexcited carriers. Electron-electron scattering dominates the initial relaxation process confirmed by ultrafast dynamics, tens to hundreds of femtoseconds, observed in pump probe studies [43], [44] creating an electronic distribution of hot carriers out of equilibrium with the lattice figure 5.1 Phonon relaxation is impeded by high optical phonon frequency of graphene $\omega_0 = 200\,meV$ which suppresses the optical phonon relaxation

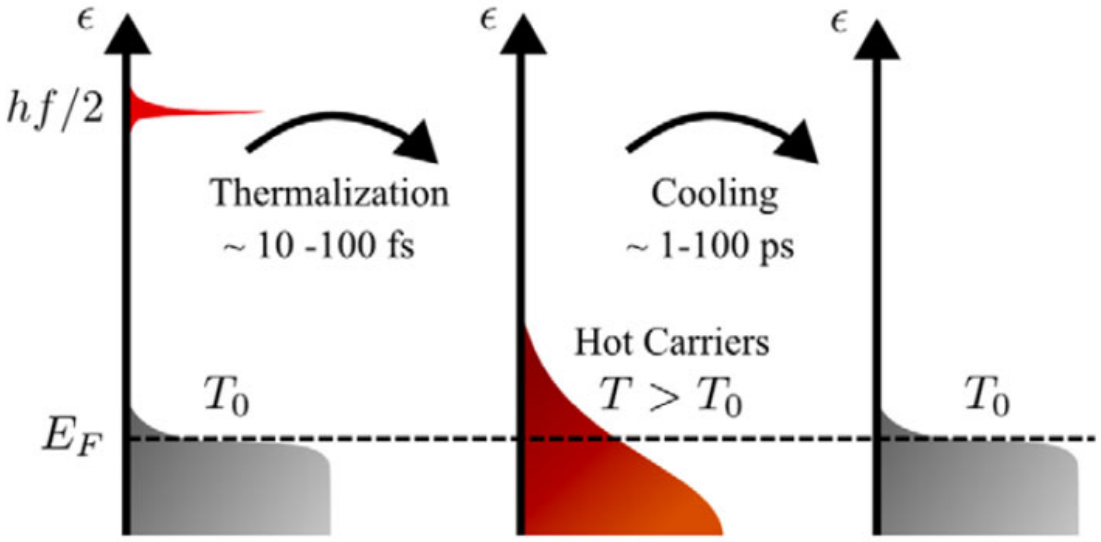

Figure 5.1 Energy relaxation of hot carriers. In the first figure excited electrons cascade to lower energy's, losing energy via Auger-type processes and phonon emission leading to downstream carrier thermalization in timescales of tens to hundreds of femtoseconds. In the second figure slow electron - lattice cooling takes place in time scales of picoseconds slowly dissipating the energy into heat returning eventually to thermal equilibrium with the lattice [32]

pathway. At the same time the generally weak scattering between electrons and long wave acoustic phonons is further constrained by a large mismatch between the fermi velocity and sound velocity. Slow electron-lattice relaxation serves as a bottleneck for electron cooling leaving most of the energy trapped in the electronic system characterized by a different electronic temperature Te, much higher than the lattice Tl a direct consequence of the smaller electronic Capacitance $C_e \sim 10^{-3}\ C_{lattice}$. This thermal decoupling leads to large diffusion lengths $0.1 - 1\,\mu m$ and carrier multiplication affecting the quantum efficiency of the system, namely the number of electrons arriving at the contacts per

photon absorbed. In device applications like dual gate p-n junctions and photodetectors the PTE manifests itself in the six-fold pattern of the voltage distinguishing it' s origin from the photovoltaic effect (PV). This pattern can be traced to the nonmonotonic dependence of the Seebeck coefficient to the μ controlled by the gate. In particular as we independently sweep the gate voltages for a given non zero value of μ1 S1 features two polarity changes.

5.2 Numerical solution to the thermoelectric equation

To calculate the elevated temperature distribution, we will consider a two-temperature model and solve the heat dissipation [41] equation 5.1 in the steady state assuming a constant heating rate and unbiased operation.

$$-\nabla(\kappa_e \nabla T_e) = -\nabla \Pi \, \boldsymbol{j}_q - \frac{C_e \Delta T}{\tau_{e-ph}} + a \, P_{in} \qquad (5.1)$$

Where $\boldsymbol{j}_q = -\sigma S \nabla T_e$ is the thermoelectric current, $\Pi = S T_e$ is the Peltier coefficient, S is the Seebeck coefficient, $\sigma \; and \; \kappa_e$ is the electrical and thermal conductivity, $\Delta T = T_e - T_l \; \tau_{e-ph} \sim ps$ [40], [44], [45] is the electron-phonon relaxation time approximated as a constant function of energy

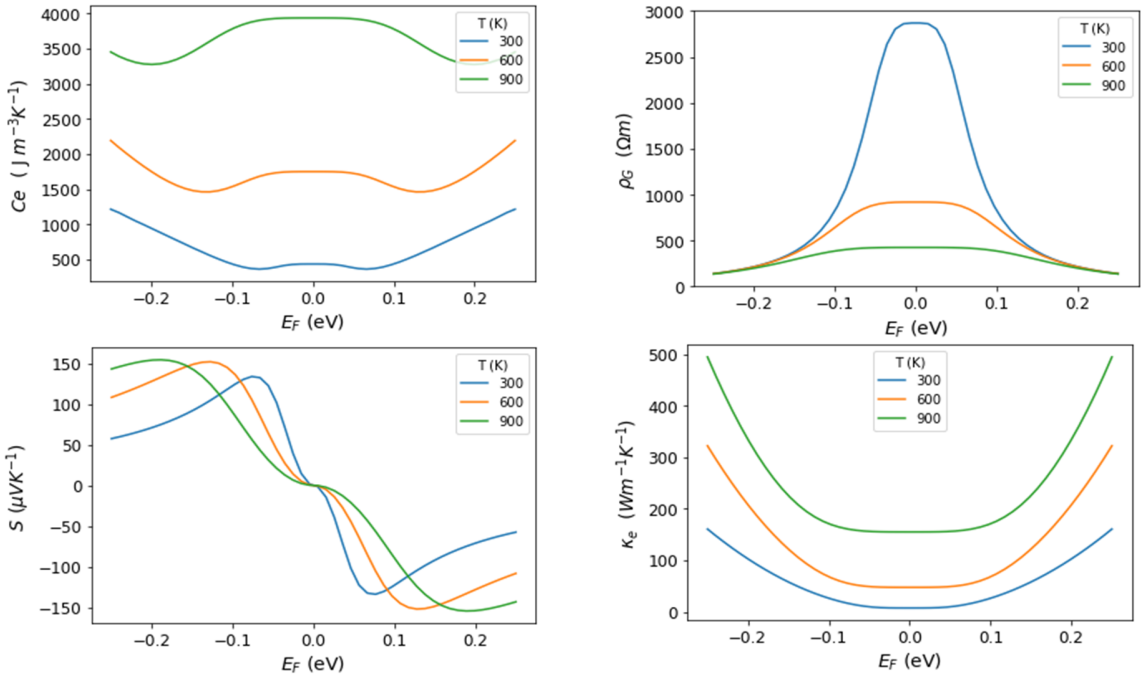

Figure 5.2 Effects of fermi energy and temperature on the thermodynamic quantities relevant to the PTE.

[41], [42] and aP_{in} is the absorbed optical power distribution. Because of the lattice large heat capacity

compared to the electronic system the lattice temperature remains close to room temperature at $T_0 = 300\,K$ in the low power limit $P_{density} < 10^9 \frac{W}{m^2}$ [46]. The graphene thermodynamic quantities $F_k(E_F,T) : \{\sigma(E_F,T), \kappa_e(E_F,T), S(E_F,T), C_e(E_F,T)\}$ vary spatially due to Fermi energy and temperature fluctuations in the channel figure 5.2. The spatial Fermi energy profile is calculated by the solution of the electrostatic model featuring the geometric characteristics of the gating architecture. Thermodynamic quantities for every grid in the graphene plane. $F_k(E_F,T)$ are statistically averaged quantities calculated with numerical integration using the Fermi Dirac statistical distribution $f(\varepsilon,\mu,T) = \frac{1}{e^{\frac{\varepsilon-\mu}{k_bT}}+1}$. Since we know the fermi energy of graphene, the equilibrium chemical potential before excitation can be obtained by solving eq 5.7 and the electrical conductivity from 5.8 described in the theory of graphene section. Mobility and residual charge values are assumed to be $\mu_e \sim 10^4 \frac{cm^2}{V}$ for electrons-holes and $n_0 \sim 10^{11}\ cm^{-2}$ typical for graphene devices. The Seebeck coefficient also known as thermopower $Q = \frac{\nabla V}{\nabla T} = < \frac{(\varepsilon-\mu)\tau}{eT_e<\tau>} >$ given by eq 5.2. while the electronic thermal capacity is given by eq 5.3.[47], [48]

$$S(\mu,T) = -(|e|T\sigma)^{-1} \int_{-\infty}^{\infty} (\varepsilon-\mu)\sigma(\varepsilon)\partial_\varepsilon f(\varepsilon,\mu,T)\, d\varepsilon \qquad (5.2)$$

$$C_e(\mu,T) = \partial_T \int_0^{\infty} g(\varepsilon)\varepsilon[f(\varepsilon,\mu,T) + f(\varepsilon,-\mu,T)]\, d_\varepsilon \qquad (5.3)$$

Finally thermal conductivity is calculated from the Wiedemann-Franz law $\kappa_e = L_0\sigma T_e$ where $L_0 = 2.44\ 10^{-8} \frac{W\Omega}{K^{-2}}$ is the Lorentz number. Knowing $F_k(E,T)$ all the factors C_k can calculated and the discrete 2D heat Equation can be formed. The final solution is obtained using a relaxation algorithm for the equilibrium temperature distribution $\Delta T(x,z)$. Central difference approximation is used for the first and second derivative operators in eq 5.4.

$$\partial xT = \frac{T_{i+1,j}-T_{i-1,j}}{2h}, \partial zT = \frac{T_{i,j+1}-T_{i,j-1}}{2h}, \partial_x^2 T = \frac{T_{i+1,j}-2T_{i,j}+T_{i,j-1}}{h^2}, \partial_z^2 T = \frac{T_{i,j+1}-2T_{i,j}+T_{i,j-1}}{h^2} \qquad (5.4)$$

Subscripts i,j denote the indices of the rectangular grid in the x,z derection and h is the distance separating two neighboring grid points. Reorganizing terms, an explicit expression for T_{ij} can be written eq 5.5 , where by the temperature at any point is dependent upon the values of the factors C_k and the values of neighboring temperature grids represented as $T_c, T_r, T_l, T_d, T_u = T_{i,j}, T_{i+1,j}, T_{i-1,j}, T_{i,j+1}, T_{i,j-1}$.

$$T_c = \frac{2T_0c_4h^2 - T_dc_1h - 2T_d + T_lc_1h - 2T_l - T_rc_1h - 2T_r + T_uc_1h - 2T_u - 0.5c_3(T_d - T_l + T_r - T_u)^2 - 2c_5h^2}{T_dc_2h - T_lc_2h + T_rc_2h - T_uc_2h + 2c_4h^2 - 8} \qquad (5.5)$$

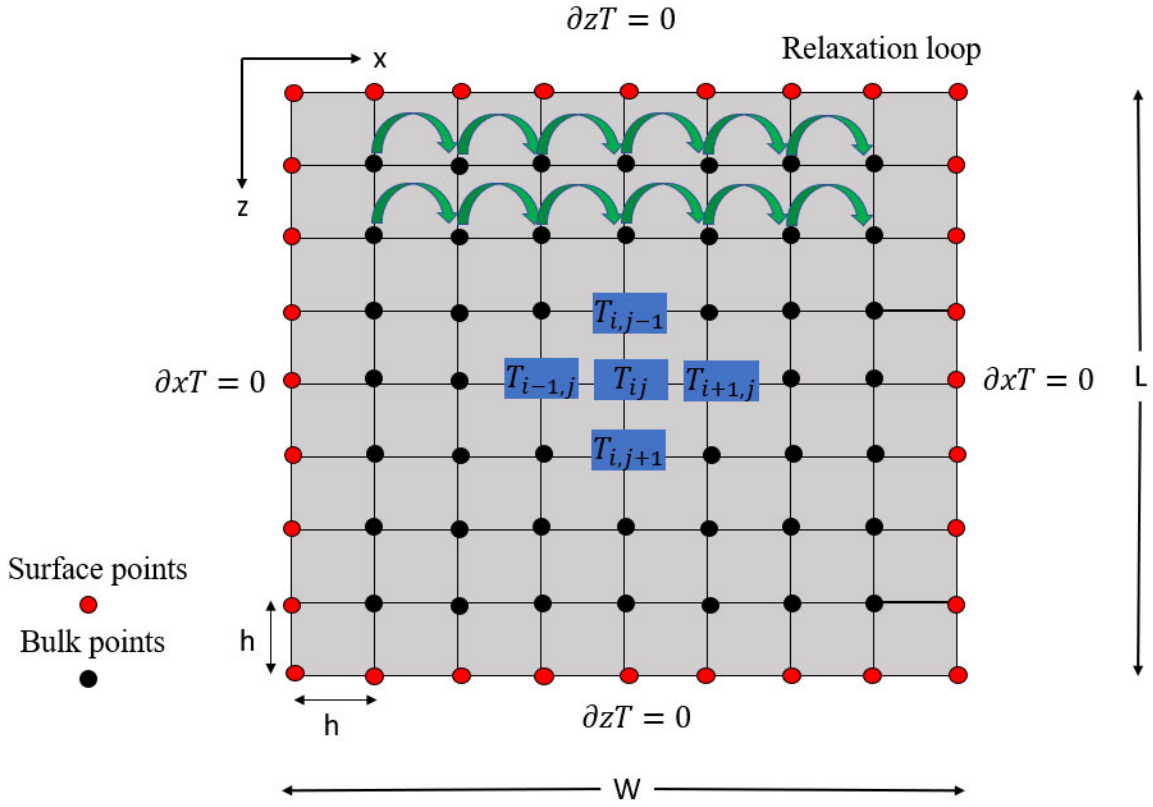

Figure 5.3 Temperature relaxation algorithm in a 2-dimensional grid using central differences

The relaxation algorithm works by updating the values of all grid points using Eq 5.5 until the change in temperature distribution is below some predetermined tolerance figure 5.3. At the boundary we use Von Neuman boundary conditions. In the weak heating regime $\Delta T \sim 1\ K$ we can safely assume that the thermodynamic quantities F_k and in extent the factors of the Eq 5.3 do not change during the relaxation loop thus no update of the factor C_k matrices is necessary. If the heating is stronger eg temperature $\Delta T > 100\ K$ the need for frequent updating of the factor matrices C_k is unavoidable. For the size of a typical device ~ 5 x 50 um and the size of the grid spacing 5x5 nm creates a number of integral calculations in the order of millions rendering the algorithm slow and unpractical. A workaround to this problem is to estimate the value of $C_k(E_{i,j}, T_{i,j})$ form tabulated matrices in the ranges of intrest $(E_{min}, E_{max}), (T_{min}, T_{max})$ [46] and the use of taylor expansions for increased accuraccy. The temperature difference between the hotspot at the center of the channel and the contacts creates a thermoelectric voltage eq 5.4 where W is the distance between source-drain and L

$$V_{PTE} = L^{-1} \int_0^L \int_0^W S \nabla T_e dx dz \qquad (5.6)$$

is the length of the device along the wave propagation axis. The thermo-electric current is $I_{PTE} = \frac{V_{PTE}}{R_D}$ where R_D is the total resistance of the device and it is calculated as $R_D = R_C + 2R_G$ where: $R_C = \rho_c L_{contact}$, $\rho_c \sim 1000\ \Omega\mu m$, $R_G = \int_0^L \int_0^W \sigma(x,z)^{-1} dxdz$ are the contact resistance, contact resistivity and graphene sheet resistance. Figures of merit detailing the device performance are, $R_V = \frac{V_{PTE}}{P_{in}}$ and $R_I = \frac{R_V}{R}$ voltage and current responsivity, corresponding to power efficiency and $NEP = \frac{I_j}{R_I}$ measured in $\frac{A}{\sqrt{Hz}}$ corresponding to device sensitivity, where I_j is the Johnson noise current [9]. Other assumptions that we make are that the Fermi energy transitions linearly to the fermi level of the metal near the contacts $d_{trans} \sim 40\ nm$ and that the τ_{e-ph} takes a bulk value $\tau = 3\ ps$ away from the boundary and an increased cooling surface value of $\tau_s = 0.5\ ps$ near the boundary regions [12] (~ 20 nm skin depth) due to increased scattering from surface atom states and electron reflection at the edge of the graphene sheet.

6 Split gate graphene photodetectors

6.1 Device setup

The design of the photonic split gate graphene photodetector figure 6.1 consist of an integrated Si WG embedded on a SiO2 substrate with variable WG cross sectional parameters w, h. The active layer graphene channel is situated atop the WG cladding at a distance of 20 nm a common choice of similar fabricated devices in the literature [3], [4], [13]. Further decreasing this distance would increase evanescent field strength but this is subject to fabrication constraints. Two gold electrodes are placed symmetrical to the WG in order to collect the photocurrent with a thickness of 50 nm in a 1D contact [12] configuration in order to minimize the heat dissipation effects of the contacts and device resistance [10]. The channel width - length W, L are variables that can be optimized based on the target application, affecting device resistance and peak temperature inside the channel. For RV optimized devices resistance is unimportant while temperature gradient plays a crucial role. Channel width W = 3 μm is chosen to allow the temperature to decay properly while channel length is left to

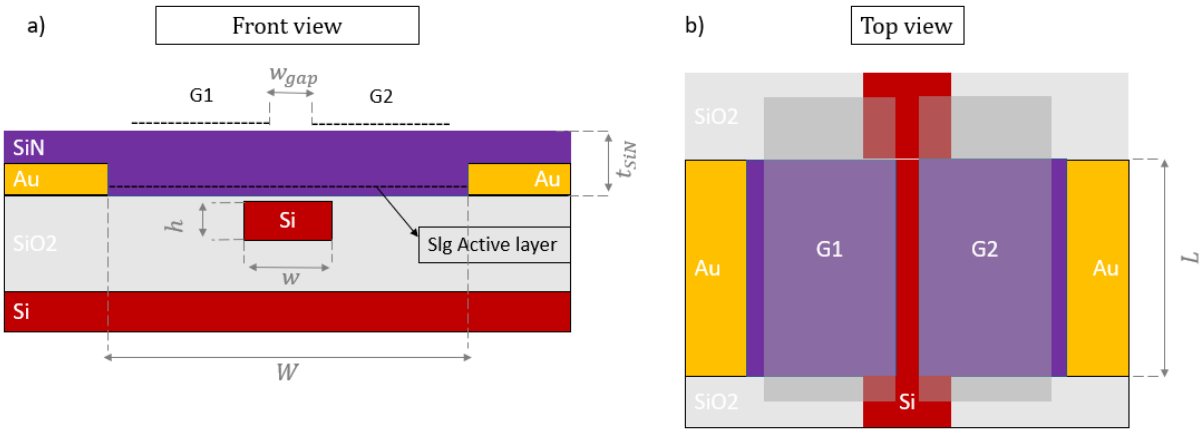

Figure 6.1 a) Front view schematic diagram of the graphene PD showing the key variable dimensions of the top and bottom graphene structures. b) Top view schematic diagram

be optimized by further simulations. For RI optimized devices long device setups are favored as they lower resistance and maximize the total absorbed power. $L = 50\ \mu m$ is chosen close to similar device setups in the literature as the relationship between device length and RI is well understood while leaving W to be optimized because of its dynamic effects on parasitic loss, temperature decay and resistance. The thickness of the spacer t_{SiN} and w_{gap} are considered free variables set to 100 nm and 150 nm, for all simulations while studying their individual effects and adjusting when needed as the optimization process proceeds.

6.2 Photo-thermoelectric analysis and device parameter optimization

The device consists of three different absorbing materials active layer graphene, gates and contacts. In order to decompose the intricate dissipative processes, a simpler device is first constructed absent of gates and contacts to study the effects of cross section on the evanescent modal fields. The cross-sectional parametric study is carried out using the 480 x 220 Si WG as a reference varying one of the dimensions while holding the other pinned at reference value. This albeit not indicative of maximum performance reduces the complexity of mode shape evolution, furthering the understanding behind the origins of performance enhancement, offering flexibility to different fabrication limitations of the device. Lumerical eigen mode solver is used to find the imaginary part

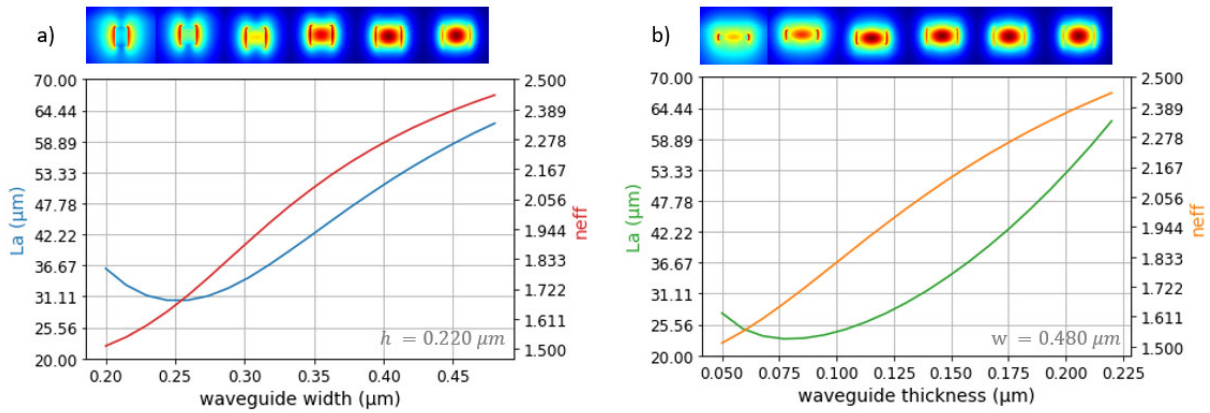

Figure 6.2 Absorption length La and neff as a function of WG (a) width and (b) thickness. (Top of the figures) Progressive pictures of the magnitude square of the electric field. The fields around graphene increase as the cross section decreases and light is squeezed outside of the waveguide until field density starts decreasing in the space outside the WG.

of the effective index k_{eff} as a function of h, w and then calculate the absorption length $L_a = \frac{\lambda_0}{4\pi k_{eff}}$ which is a measure of how long the mode has to travel until the power drops to 1/e of its original strength figure 6.2. The absorption length shows a non-monotonic shape characterized by the evanescent field strength outside the WG. As the size of the core decreases the strength of the evanescent fields increases until enough of the mode is outside the WG causing it to inflate and lose intensity once again. Full wave 3D FDTD simulations are performed for the fundamental TE mode

at 1550 nm (optical communications band) in order to capture the individual effects of each absorber

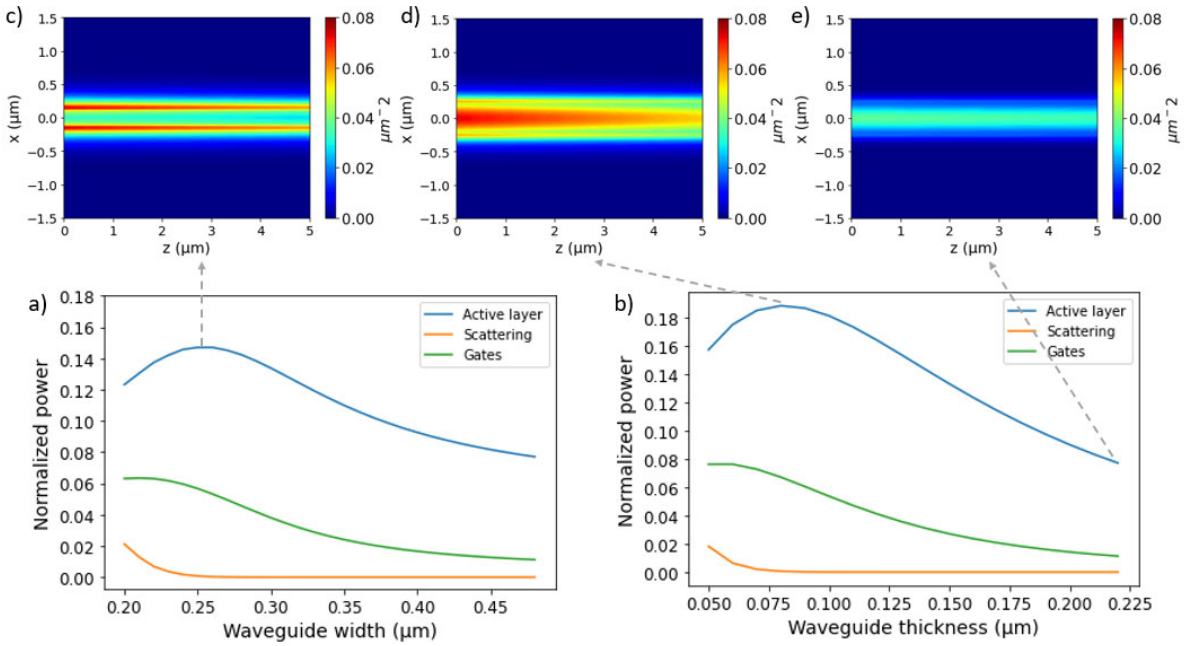

Figure 6.3 (a-b) Normalized power fraction distribution for all the loss processes as a function of WG width - thickness. (c-e) Absorption density distributions at the active layer graphene showcasing variance in regards to width, thickness and reference cross sectional parameters.

and the scattering effects accompanied by such evanescent modes. Figure 6.3 a-b shows the fraction of source normalized power that is expended at each dissipative process as the modes change from localized modes inside the WG to leaky evanescent ones. There is to a certain extend good agreement in regards to the optimum with the 2D eigenmode solver indicating the perturbative nature of the gates and scattering/contacts (parasitic loss). The loss process is dominated by graphene absorption with the gates absorbing proportionally to active layer in relatively confined modes. Both parasitic and gate losses increase for more evanescent modes, more so in the case of WG thickness which is something to be expected as we squeeze the light directly towards the direction of the gates-contacts. Figure 6.3 shows the absorption density of graphene for different WG dimensions corresponding to the peaks of (c) width, (d) thickness curves and (e) reference cross section. For the width squeezing cross section light concentrates in narrow strips at the edges of the WG reaching absorption densities of $0.06\,\mu m^{-2}$. For the thickness squeezing cross section we have similar magnitude absorption densities but broader in area localized at the center of the WG. The second part of the parametric analysis is to investigate how these different absorption densities impact the solution to the thermoelectric equation. For this purpose, the absorption densities generated from photonic

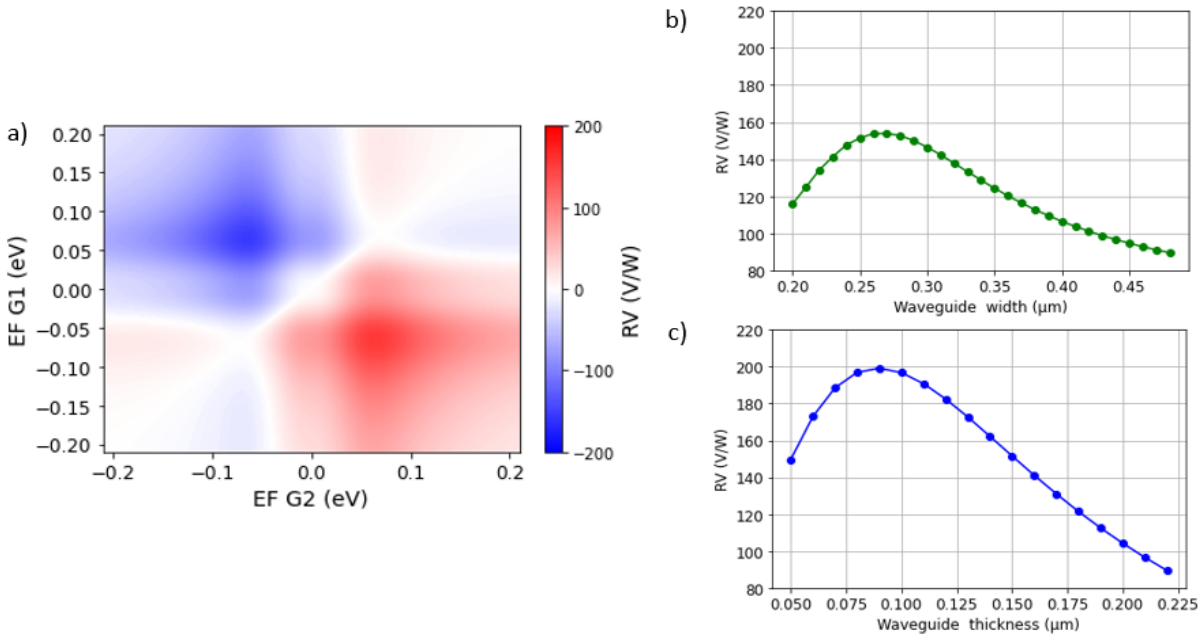

Figure 6.4 (a) Voltage responsivity heatmap RV as a function of Fermi energy induced by the dual gates. (b-c) RV as a function of WG width-thickness featuring a 1.5fold and 2fold increase in RV for corresponding cross sections of 270 x 220 and 480 x 90. Reference values for RV is the last data point in each graph representing the 480 x 220 Si WG cross section.

simulations are used as input to solve the 2D thermoelectric equation according to the methods detailed in the thermoelectric section in the weak heating regime $P_{in} = 1\,\mu W$. In figure 6.4 (a) heatmap of RV versus Fermi energy is generated for a candidate cross section. As the dual gates independently control the p – n type of each region a six-fold pattern emerges in the voltage responsivity a characteristic of the PTE [3], [4], with the maximum values of RV attained at $EF_{1,2} = \pm\, 0.07\, eV$. Simulations are then run for every cross section assessing the impact of different absorption density distributions on the voltage responsivity. Figure 6.4 b-c shows that a 1.5fold and 2fold increase in RV is achievable for corresponding cross sections of 270 x 220 and 480 x 90. Figure 5 a-d illustrates the individual thermodynamic quantities that play an important role in the PTE for the two optimized and reference device cross sections. The temperature difference figure 5a and temperature gradient 5b correspond to different heating distributions. While the temperature distribution away from the gap follows the expected hyperbolic behavior shown in previous theoretical work [39] closer to the gap where the fermi energy and in extension the coefficients of the thermoelectric equation vary, the solution takes a different form dependent on the spatial distribution of heating. The fermi energy obtained from the solution of the electrostatic model figure 5c forms a sigmoid pattern, from p region to the n region, passing in the interim from 0. In practice this means

that the thermal conductivity and Seebeck coefficient are at the lowest at this point facilitating the buildup of carriers by the inability to transport energy away by diffusing/accelerating carriers away. A symmetric distribution with maximum absorption density at the center (x = 0) would take advantage

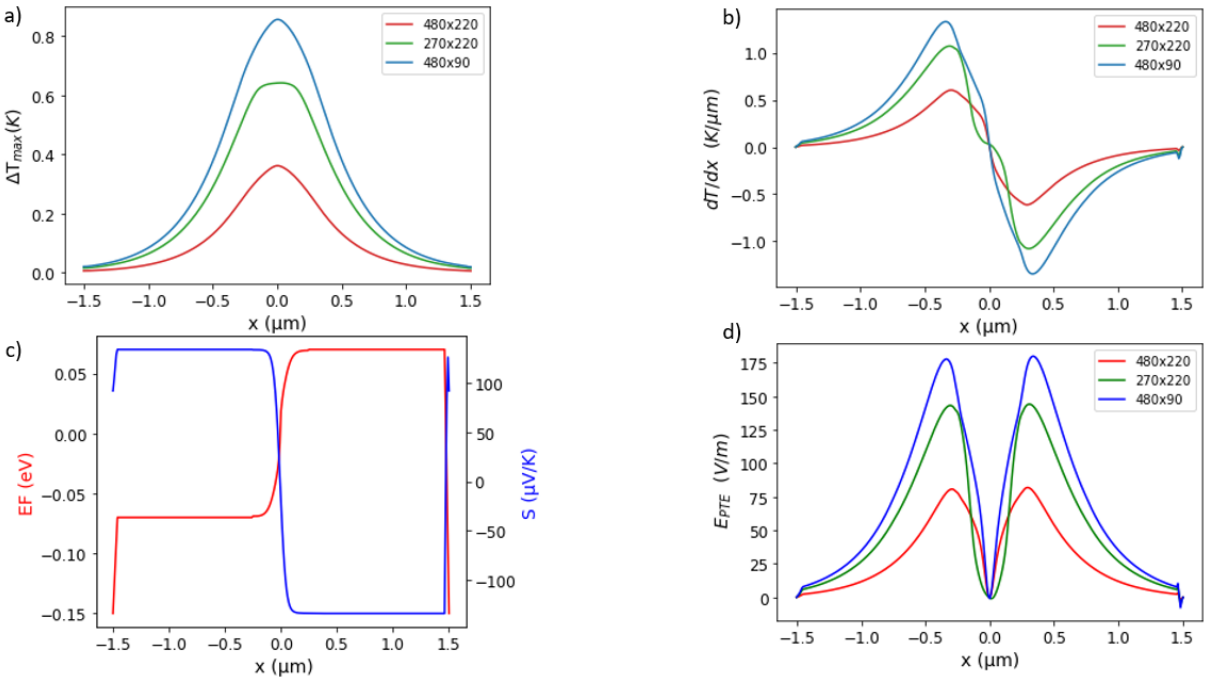

Figure 6.5 (a) Temperature difference profile along the source-drain direction (x-axis) for 3 WG cross sections. (b) Temperature gradient profile across the x-axis. (c) Fermi energy and Seebeck across the x-axis. (d) Thermoelectric field strength across the x-axis. All quantities are evaluated at the same z where temperature difference is maximized

of this raising the temperature and thus the thermoelectric voltage. Figure 6.5 a-b depict the effects of these aforementioned dynamics. In figure 6.5d the thermoelectric field is formed across the source drain direction inside the channel. This field is responsible for generating current from temperature differences, $E_{PTE} \sim S\frac{dT}{dx}$ affected both by changes in temperature distribution and doping profile. The symmetric double lobe-shape arises from the simultaneous sign change in Seebeck coefficient and temperature gradient maximizing the area under E_{PTE} and thus V_{PTE}. From figure 6.5(b) we can see that there is variance across devices in $\frac{dT}{dx}(x)$ prompting the study of the effects of W_{gap} on RV figure 6.6 a. The results confirm that devices with heating distributions that produce larger temperature gradients closer to the areas of low Seebeck are affected the most. In order to severely impact performance w_{gap} must extend to the areas of high temperature gradient expected to be close to FWHM for gaussian like distributions. We can generalize this to the conclusion that as long as w_{gap} << FWHM there is not significant impact on performance. The Fermi energy distribution tends to

get stretched tending towards a diagonal line shape figure 6.6 b. Another parameter affecting modal shape and loss is spacer thickness $tSiN$.

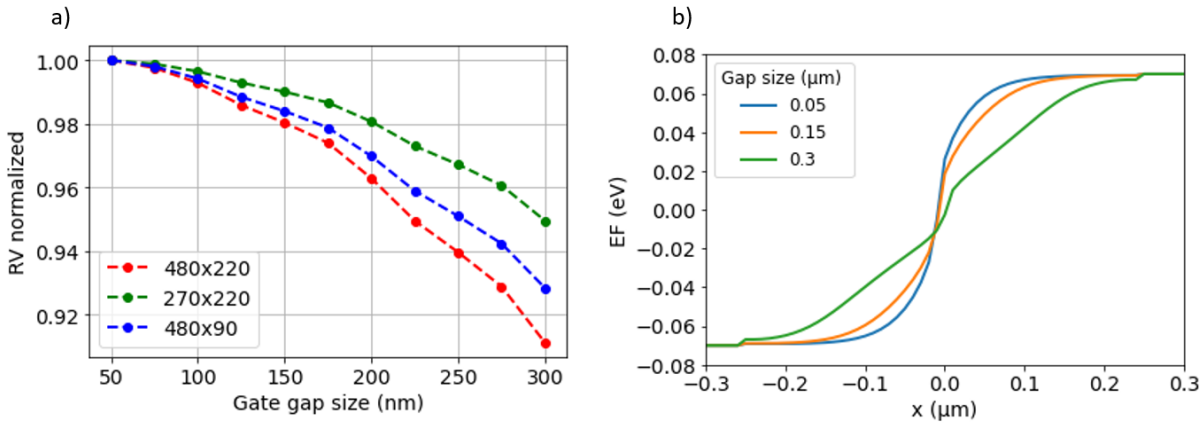

Figure 6.6 (a) RV as a function of gate gap size (b) Fermi energy distribution along the source drain direction (x) for different gap sizes.

The thickness of the spacer acts in two ways demonstrated in figure 6.7 a. One effect is that it alters the dielectric environment on top of the WG providing a higher effective index to the mode allowing it to be more evanescent on top benefiting active layer absorption. At the same time the lowering of

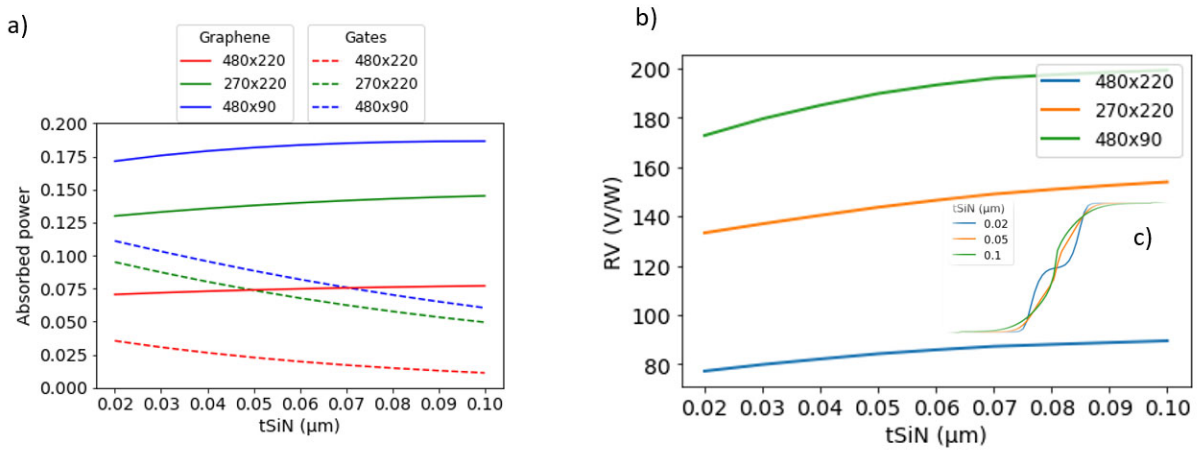

Figure 6.7 (a) Absorbed power (b) RV as a function of gate dielectric thickness (tSiN) for active layer graphene (dotted line) and the gates (solid line) in different WG cross section configurations. (c) Fermi energy as a function of thickness near the gap region.

the gates leads to greater losses. Active layer absorption is ultimately decided by the density of the EM fields saturating around 100 nm. Distancing the gates from the active layer results in shape wise changes to the Fermi energy distribution figure 6.7 c. The combined effects of absorption and fermi

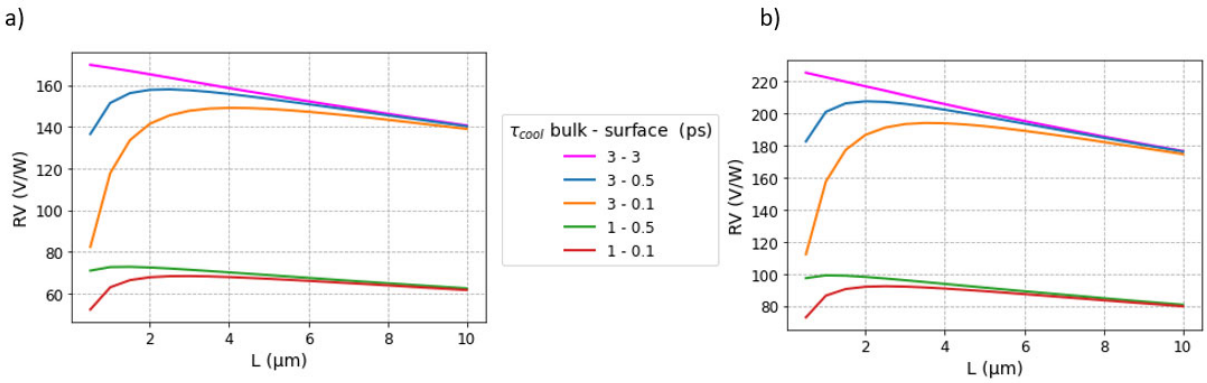

Figure 6.8 RV as a function of length and different surface-bulk cooling times for WG cross-section a) 270x220 b) 90x480

energy appear to have the greatest impact on RV 6.8b when $\frac{t_{SiN}}{w_{gap}} \ll 1$. Without some artificial boundary conditions voltage responsivity appears to be ever increasing as device length gets smaller due to increased average absorption densities, something that conflicts empirical evidence. By including a different cooling time $\tau_{surface}$ for points near the boundary of graphene a more accurate description can be achieved as evident in figure 6.8. With decreasing size, the cooling mechanism transitions form bulk dominant (convergent lines) to surface dominant scattering (divergent lines) increasing the cooling capacity per unit length of the device. When the difference between the bulk and surface cooling times is sufficient there comes a point where the increase in absorption density per unit length is matched by an equal increase in cooling resulting in peak RV. Thus, the point of this trend reversal in RV is a macro quantity indirectly probing the relative strength of electron phonon interactions in the bulk-surface regions in graphene. In any case a value of at least 70 V/W appears to be a realistic lower performance limit of optimized graphene split gate PDs. For some applications current responsivity RI is more important than voltage. RI is given by voltage responsivity divided by resistance. Resistance scales down with increasing device length while total absorption peaks. These mechanisms make it clear that the length of the device should be such that almost all of the available power is absorbed. The width of the device W affects sheet resistance, parasitic losses and temperature relaxation. To investigate all these effects 3D FDTD simulations are run for devices at L = 50 μm and W = 1-3 μm using the fundamental TE mode at 1550 nm. Figure 6.9 a-c illustrates the absorption density at W = 1.5 μW for three WG cross sections featuring different degree of plasmonic losses affected by both the evanescence of each mode and the distance from contacts (W). Figure 6.9 d features the power makeup between the different absorption-loss processes. Plasmonic-gate losses affect mainly the RV optimized cross sections due to their evanescent character. After W = 2 μW no

significant change in graphene total absorption occurs. In order to evaluate channel resistance and temperature decay thermoelectric simulations are performed. Figure 6.10 a confirms the same

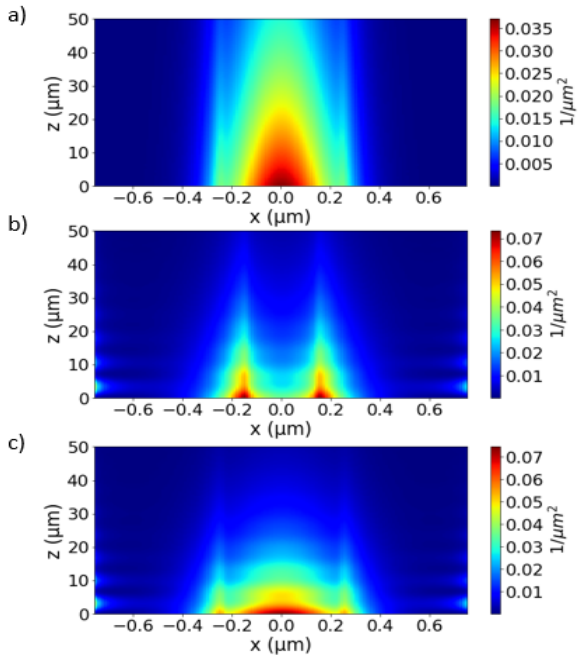

d)

Waveguide Cross section (nm x nm)	W source-drain	Active layer graphene	Scattering-contacts	Gates	Transmission
480x220	1 1.5 2 2.5 3	0.52 0.52 0.52 0.52 0.52	0.02 0 0 0 0	0.08 0.08 0.08 0.08 0.08	0.38 0.4 0.4 0.4 0.4
270x220	1 1.5 2 2.5 3	0.48 0.62 0.65 0.66 0.66	0.32 0.08 0.01 0 0	0.18 0.21 0.22 0.22 0.22	0.02 0.09 0.11 0.12 0.12
480x90	1 1.5 2 2.5 3	0.5 0.67 0.71 0.72 0.72	0.31 0.07 0.01 0 0	0.17 0.21 0.22 0.22 0.22	0.01 0.05 0.06 0.06 0.06

Figure 6.9 Absorption density distributions at L = 50 μm and W = 1.5 μm for WG cross sections (a) 480 x 220 (b) 270 x 220 (c) 480 x 90. (d) Table describing the power absorption-loss for a range of device widths W = 1-3 μm at L = 50 μm.

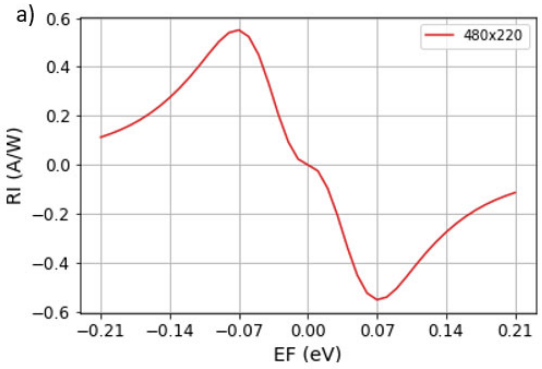

b)

Waveguide Cross section (nm x nm)	W (μm) source-drain	RV (V/W)	R(Ω)	RI (A/W)	NEP ($pW/\sqrt{Hz}$)
480x220	1 1.5 2 2.5 3	33 49 57 60 62	73 88 103 118 133	0.45 0.56 0.55 0.51 0.46	33 24 23 23 24
270x220	1 1.5 2 2.5 3	9 42 63 69 72	73 88 103 118 133	0.12 0.48 0.61 0.58 0.54	116 28 21 20 20
480x90	1 1.5 2 2.5 3	11 48 69 76 78	73 88 103 118 133	0.15 0.54 0.67 0.64 0.59	100 25 19 18 19

Figure 6.10 (a) RI as a function of fermi energy in the antisymmetric gating configuration. (b) Table containing figures of merit along with parameters of the thermoelectric study of W.

optimum, $EF_{1,2} = \pm 0.07$, for RI in terms of fermi energy pointing to RV maximization rendering any performance gain from resistance reduction at smaller EF irrelevant. Figure 6.10 b is a table containing figures of merit and parameters associated with integrated PD. Results show RV increasing asymptotically event beyond the point of saturating absorption pointing to an increase in $\frac{dT}{dx}$ in the source-drain direction resulting from more efficient cooling. RI increases albeit increased resistance peaking at W = 2 μm. At the infinite length limit device resistance is minimized thus the device that more efficiently eliminates losses would be the optimum.

6.3 Effects of input power

Since there is a wide range of input power used in experimental measurements of RV for different devices, in order to make accurate quantitative comparisons between different experimental set ups it is important to know the effects of input power. For this purpose, thermoelectric simulations

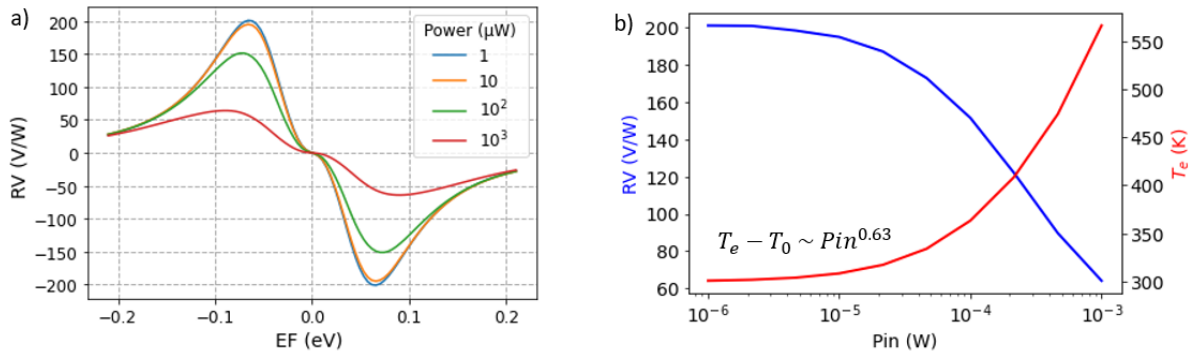

Figure 6.11 (a) RV as a function of energy and EF (b) RV and electronic temperature as a function of input power at $EF_{1,2} = \pm 0.07$, $A_{density} = 0.07 \frac{1}{\mu m}$

are performed at different input power levels. Qualitative and quantitative changes are observed for RV. Voltage responsivity drops significantly for increased heating $Pin > 10\ \mu W$ while the maximum value is displaced to larger Fermi energies experiencing peak broadening indicating to a change in dynamics figure 6.11 a. This is a direct consequence of an exponential increase in electronic temperature $T_e - T_0 \sim P_{in}^{0.63}$ figure 6.11 b affecting thermodynamic quantities. At power levels up to $1\ mW$, RV reduces to 30% of its original value. In order to better understand the mechanisms driving this reduction in performance the exact changes in the thermodynamic quantities most affected by increased heating must be explored figure 6.12 a. At increased heating both C_e and κ_e increase by 4

fold in magnitude but thermal conductivity changes behaviour inside the split gate region now increasing as we move closer towards the center. At the center of the chanel is where most of the heating takes place, a relative increase in thermal conductivity will shift the dynamics towards a more diffusive regime facilitating energy transport away from the center. To truly unravel the interplay

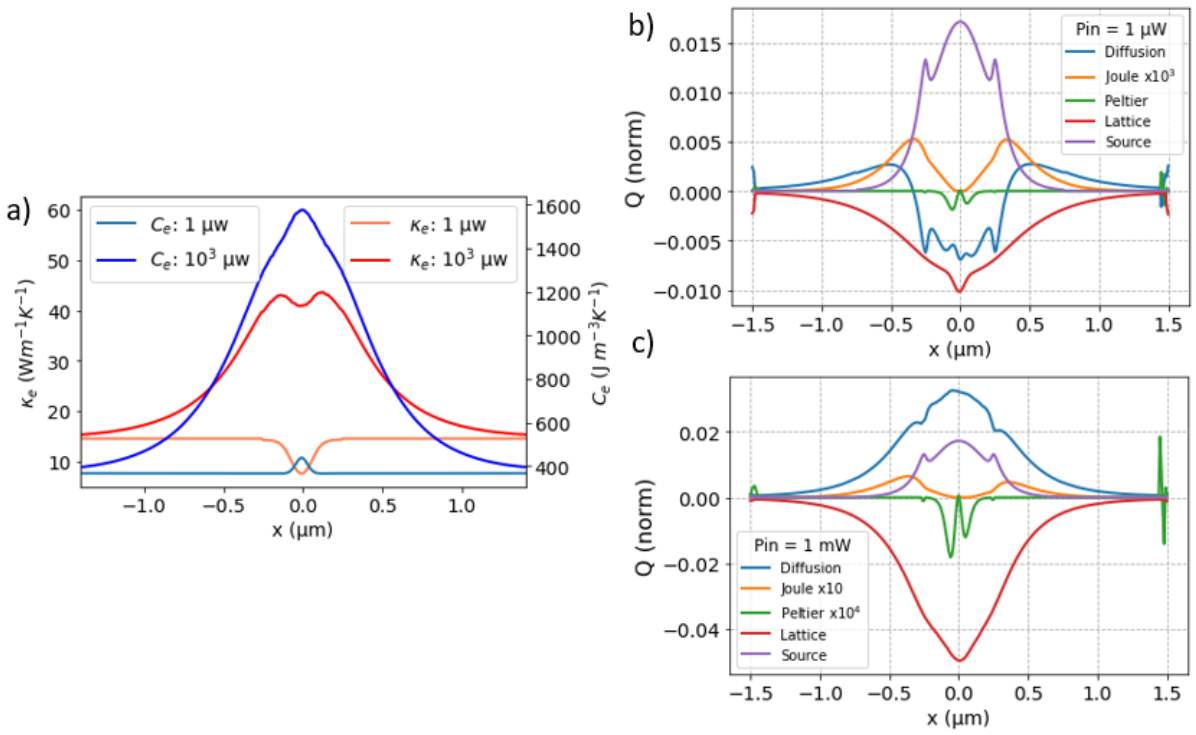

Figure 6.12 (a) Electronic heat capacity C_e and electronic thermal conductivity κ_e (b-c) Local energy flux equilibrium representing energy inflows (Source), outflows (Lattice) and transport terms at low and high heating intensity.

between the different heating, cooling and transport mechanisms one must look at the local energy flux inside the channel measuring the individual contributions of different thermoelectric phenomena figure 6.11 . At the low power limit Pin = 1 μW b we have diffusion and lattice as the bigest cotributers in removing energy from the central regions of the device where peak heating occurs with diffusion fliping sign while moving towards the boundary regions. Joule heating $\sim \frac{J^2}{\sigma}$ remains minimal , about three orders of magnitude smaller, while the peltier $\sim T\,\boldsymbol{J}\,\nabla S$ provides cooling at the gap region. The relative strength of the source over cooling mechanims as well as efficient cooling away from the center facilitate the formation of large temperature gradients enhancing the PTE. At larger temperatures cooling is dominated by lattice relaxation while difusion has positive flows everywhere to compensate for lattice. We also notice that peltier doesn't scale well with temperature , being about

4 orders of magnitude smaller ,while Joule increases in strength, heating with equivalent power of $1/20^{th}$ of the source. Thus we have identified the shift in cooling dynamics responsible for the reduction in PD efficiency at higher input power levels. In experimental literature weak heating , linear voltage-power equation, is often assumed for low input power, but the extend to witch this linearity holds and the relationship between relaxation and graphene quality is unknown.

7 Plasmonic slot gate graphene photodetectors

7.1 Device set up

The device consists of a Si WG with a variable cross section to be determined by coupling methods, embedded in a SiO2 substrate. The dielectric WG guides the light to the partially overlapping vertically aligned plasmonic structure the slot WG figure 7.1 a. The slot WG is situated on top of the dielectric WG at a distance of Hc and overlaps for a distance Lc. The Au arms forming the MIM slot WG also serve as gates for the graphene channel which is positioned as close as possible ~ 10 nm below the gates with interim space filled with the AlO completing the dielectric gate. Similar FET devices recently experimentally realized [49] featured a breakdown voltage of 0.8 V/nm enough for the gating purposes of this application. AlO is also added in the gap and further 40 nm on top of the gates to fully encapsulate the device [3]. At either ends of the graphene channel figure 7.1 two gold

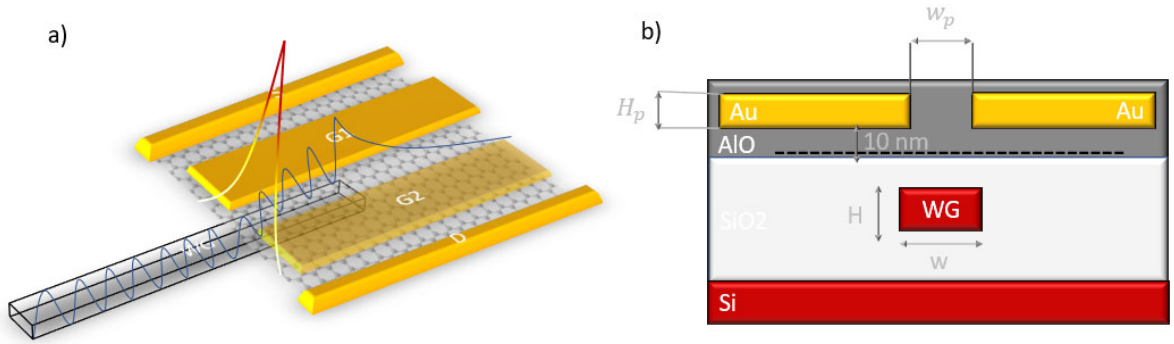

Figure 7.1 (a) Schematic of the full device set up. (b) Profile of the device laying out fixed and variable parameters. The black dotted line represents the graphene active layer situated 10 nm below the gates. Between graphene and the gates and up to 40 nm above them the space is filled with AlO.

pads form a 1-D contact with the graphene completing the electrical circuitry of the device. The width Wp and height Hp of the slot WG are the most important geometric parameters as they determine the coupling strength to the dielectric WG, the intensity of the evanescent fields at the graphene plane, as well as the profile of the Fermi energy adding several layers of complexity to the device optimization process. The length of the graphene is chosen as L = 3 μm for the majority of simulations until other parameters are finalized. The width of the channel is chosen W = 2.5 μm given the localization of the absorption density and further reviewed when we obtain temperature distributions.

7.2 Photo-thermoelectric analysis and device parameter optimization

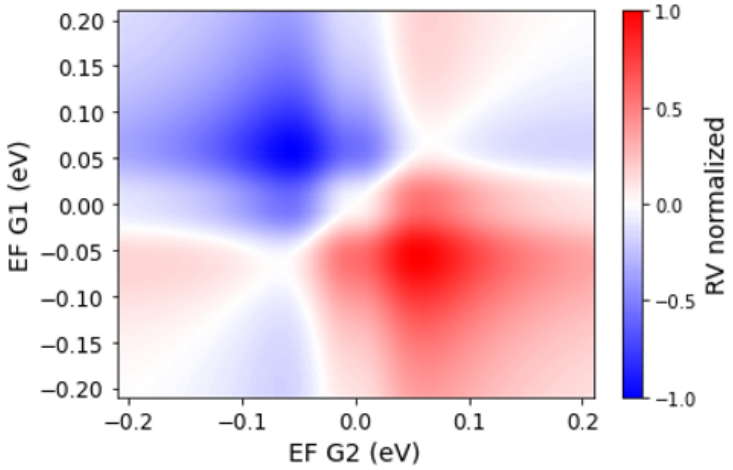

Figure 7.2 Normalized RV as a function of fermi energy induced by the two gates G1, G2. The maximum is observed around $EF_{1,2} = \pm 0.06\, eV$

3D FDTD simulations are performed by directly injecting the slot WG with the fundamental TE eigenmode at 1550 nm, changing one of the cross-sectional parameters Wp, Hp while holding the

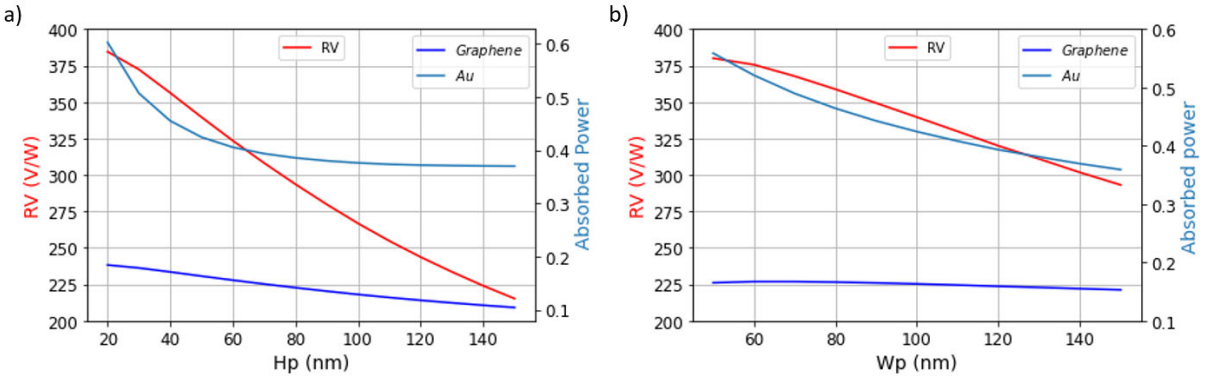

Figure 7.3 RV (left y axis) and total absorbed power among different absorbers (right y axis) as a function of (a) Wp for Hp = 50nm and (b) Hp for Wp = 100 nm.

other one fixed. Thermoelectric simulations reveal optimal $EF_{1,2} = \pm 0.06\, eV$ in terms of RV figure 7.2. Photonic absorption data, $\mathrm{A(Wp, Hp = 50\ nm)}$ and $\mathrm{A(Wp = 100\ nm, Hp)}$, combined with corresponding thermoelectric simulations for different slot cross sections are shown in figure 7.3 a and 7.3 b. The lower ranges for the slot dimensions are determined based on estimated fabrication limitations. In figure 7.3 a shifting towards smaller W_p leads to increased absorption from the gates,

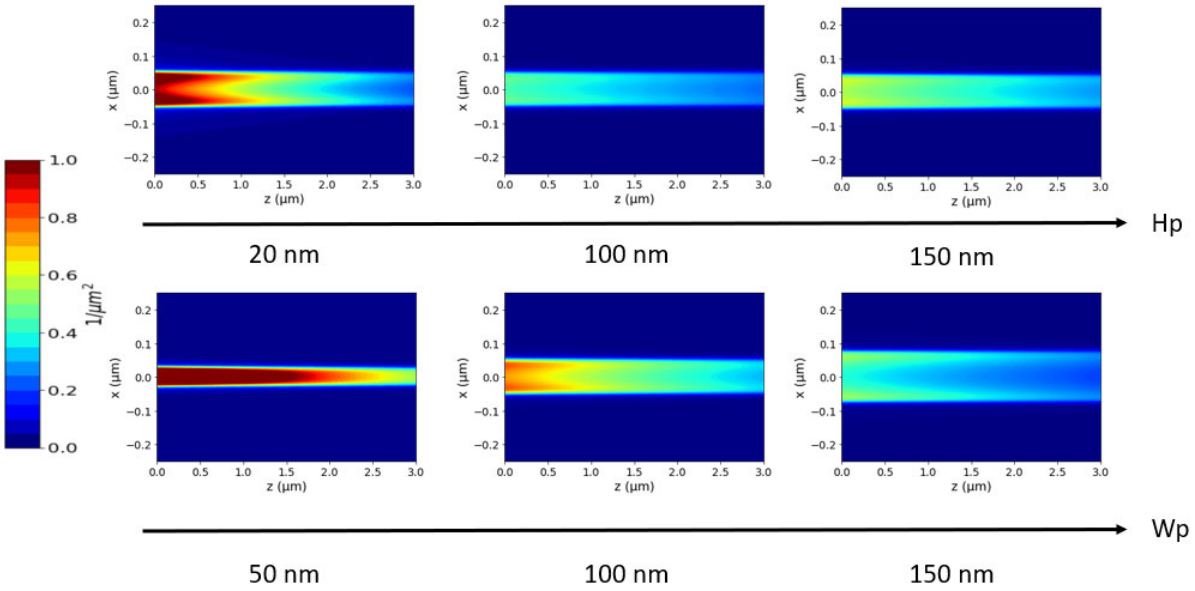

Figure 7.4 shows heatmaps for 3 different Hp (top) and 3 different Wp (bottom). The color bar (left) shows the magnitude of the absorption density in graphene measured in $\frac{1}{\mu m^2}$

but the absorption in graphene peaks around Wp = 75 nm indicating competing mechanisms. One of those mechanisms increasing RV is doping profile dependent similar to what was observed in figure 6.6 a in the case of the split gate device discussed in chapter 6. In figure 7.3 b the effects of reducing the thickness Hp lead to a monotonic increase in graphene absorption coupled with exponential increase in gate absorption for sub 50 nm dimensions. Figure 7.4 shows absorption density distribution of 6 cross sections. In the transition from bigger to smaller Wp the absorption density increases but the absorption area decreases in a similar fashion, so there comes a point where increase in absorption density cannot compensate for the reduction in area something that the Hp dimension squeeze isn't affected by. Further we plot the basic thermodynamic quantities like E_F , $S, \Delta T, \frac{dT}{dx}, E_{PTE}$ as a function of position along the source drain direction (x axis) figure 7.5. Figure 7.5 a show the Fermi energy and the Seebeck coefficient in the vicinity of the gap. The increased gap width increases the area where the Seebeck coefficient is 0 and therefore the area where there is no thermoelectric voltage. Figure 7.5 b-d show the difference in temperatures ΔT and temperature gradient $\frac{dT}{dx}$ along the x axis, looking at the temperature gradient in conjunction with the fermi energy we can identify three key regions. In Region I where EF is constant at the gate value, we have hyperbolic decay of the

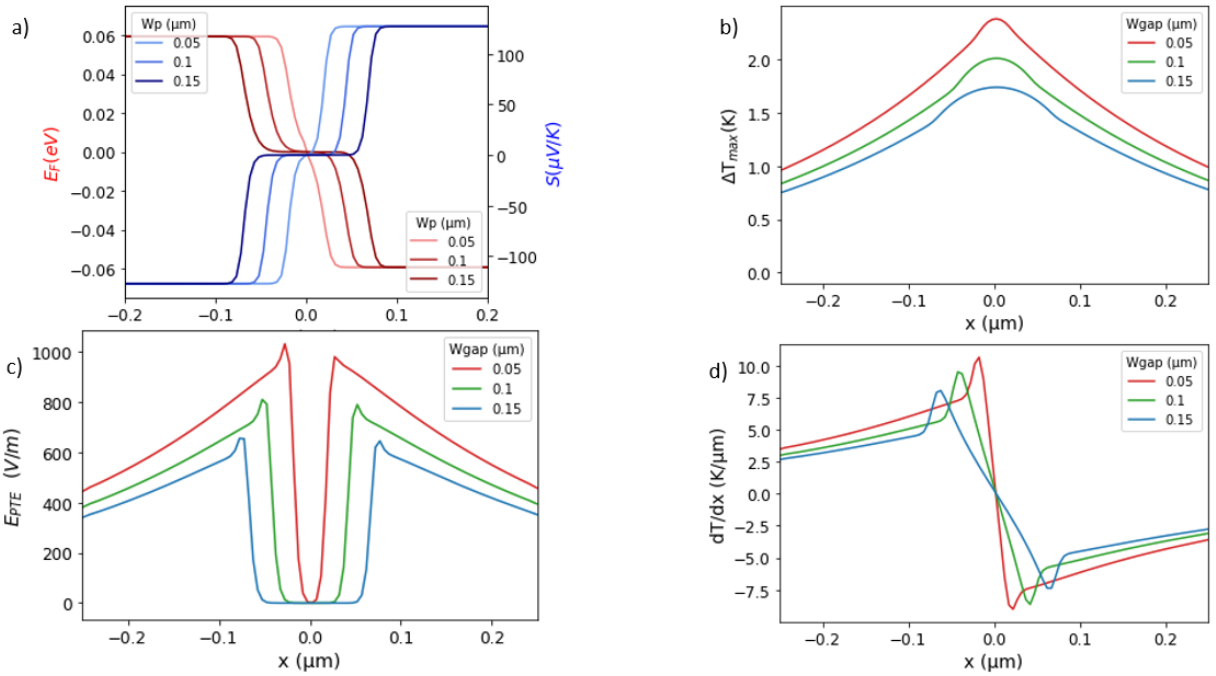

Figure 7.5 (a) Fermi energy and Seebeck coefficient profile across source-drain direction (x axis). (b-d) Temperature difference-gradient profile across the x axis. (c) Thermoelectric filed profile across the x axis.

temperature. Region II near the edge of the gap where EF starts to decrease while temperature gradient peaks corresponding to accelerating changes in conductivity and Seebeck. And finally, Region III the middle where we have EF~0 coinciding with peak in temperature and thus 0 temperature gradient. Figure 7.5 c shows the thermoelectric field expressed by the product of Seebeck and temperature gradient.

7.3 Optimization of coupling for efficient photodetection

Following the methods laid out in the coupling methods section we chose the smallest possible thickness Hp = 20 nm for the plasmonic WG and the commercially available thickness of the Si WG h = 220 nm and use the widths as free parameters to match the effective indices of the plasmonic WG figure 7.6 a with that of the dielectric WG figure 7.6 b. 2D eigenmode simulations are performed for the two WGs cross section to obtain the effective indices of the fundamental TE modes at 1550 nm figure 7.6 d. For the smallest possible Wp = 50 nm a corresponding w ~ 450 nm is chosen for the dielectric WG. Once the geometric parameters of the structures in dielectric-plasmonic region (I-III) have been specified figure 7.6 a-b, 2D eigenmode simulation are performed at the hybrid region (II)

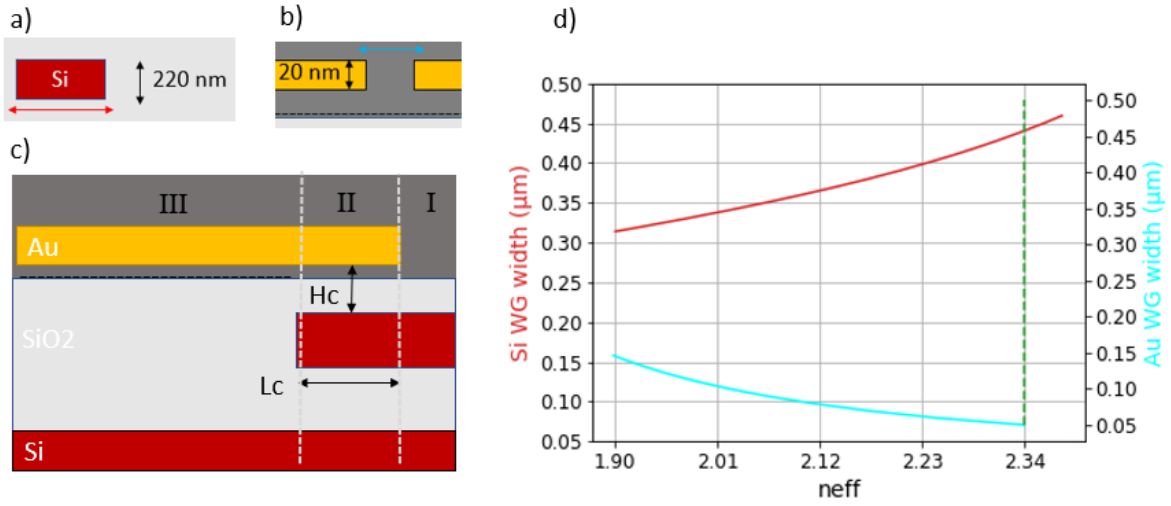

Figure 7.6 (a-b) Dielectric-plasmonic WG cross section. (c) Side view schematic depicting the 3 regions of the device separated by the white dotted line. (d) Neff as a function of cross section width in the cyan for the plasmonic and red for dielectric WG. The green vertical dotted line shows the selected values.

figure 7.6 c to determine the coupling height - length free parameter. Figure 7.7 shows even-odd mode effective index as a function of coupling height. Figure 7.7 b is a calculation of coupling length estimated from analytic formula eq 3.5 based on the phase difference of even-odd modes. The green dotted line represents the degenerate neff of the individual WGs. The increase in coupling height creates weaker interaction between the two WG structures leading to smaller index perturbations for each hybrid mode index. This pushes the hybrid modes closer to their original individual degenerate

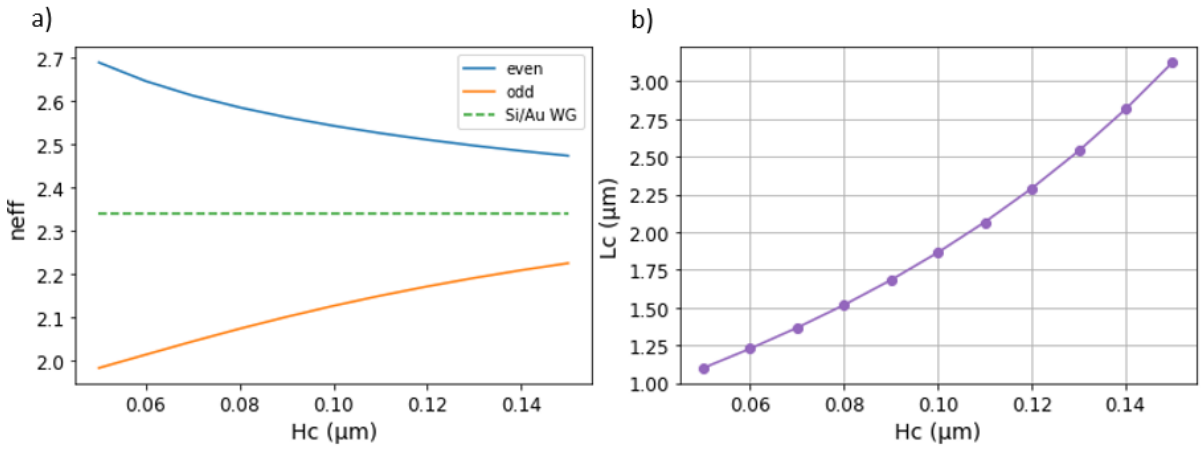

Figure 7.7 (a) Even-odd mode effective index as a function of coupling height. (b) Coupling length estimated from analytic formula eq 3.5. The green dotted line represents the degenerate neff of the individual WGs.

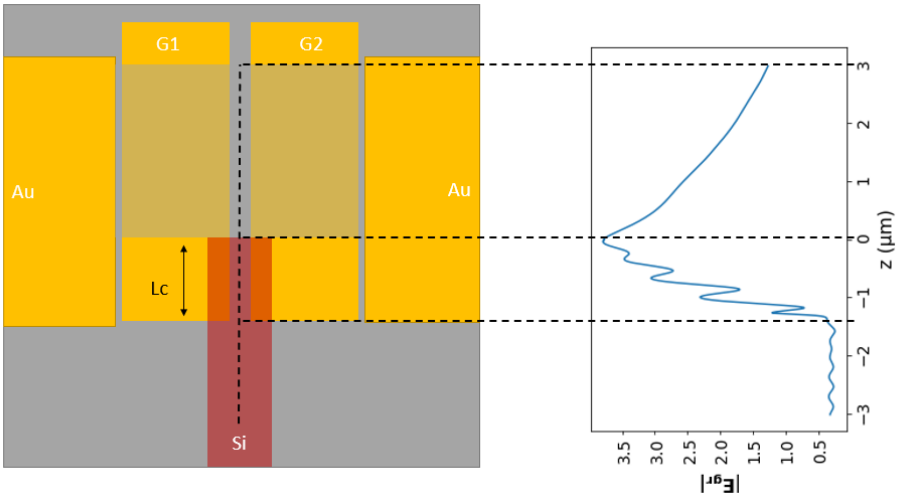

Figure 7.8 (Left) top view of the device, dotted horizontal lines separating regions I-III. (Right). Maximum value of electric field norm on the graphene plane sampled at the middle point going across the device (doted vertical line).

states, decreasing differences between the even-odd effective indices,1 decreasing the rate of phase evolution and subsequently increasing the length required for full constructive interference. The Lc obtained from the eigenmode analysis is approximate as discussed in the coupling methods chapter because of interference with counter propagating reflected modes. In addition to that it is important to precisely account for the reduction in initial reflection losses and increase in plasmonic loss as the WG structures move further apart and overlap length Lc increases. To elucidate upon these effects full wave 3D FDTD simulations are performed by injecting the fundamental TE mode at 1550 nm in the dielectric WG. Measuring the electric field strength at the center of the graphene plane in the 3 regions across the middle a general intuition can be established about the nature of the electric field at each section of the device figure 7.8. In region I the wave nature of the electric field is owed to reflections inside the WG at the interface of regions I-II and II-III. At region II the light intensity starts to increase as more power couples to the plasmonic WG situated close (10 nm) to the graphene plane. The interference pattern emerging in this region stems mainly from reflections happening at the II-III interface on the plasmonic WG. The confirmation of these reflections necessitates the search for the optimum coupling length by means of 3D FDTD simulation using application specific (RV) and more general (coupling efficiency, $|\boldsymbol{E_{max}}|$) figures of merit to evaluate the optimum coupling height-length pair for this device. Five sample coupling heights are chosen $H_c = [30,60,90,120,150]\ nm$ each corresponding to a range of coupling lengths near the theoretical value.

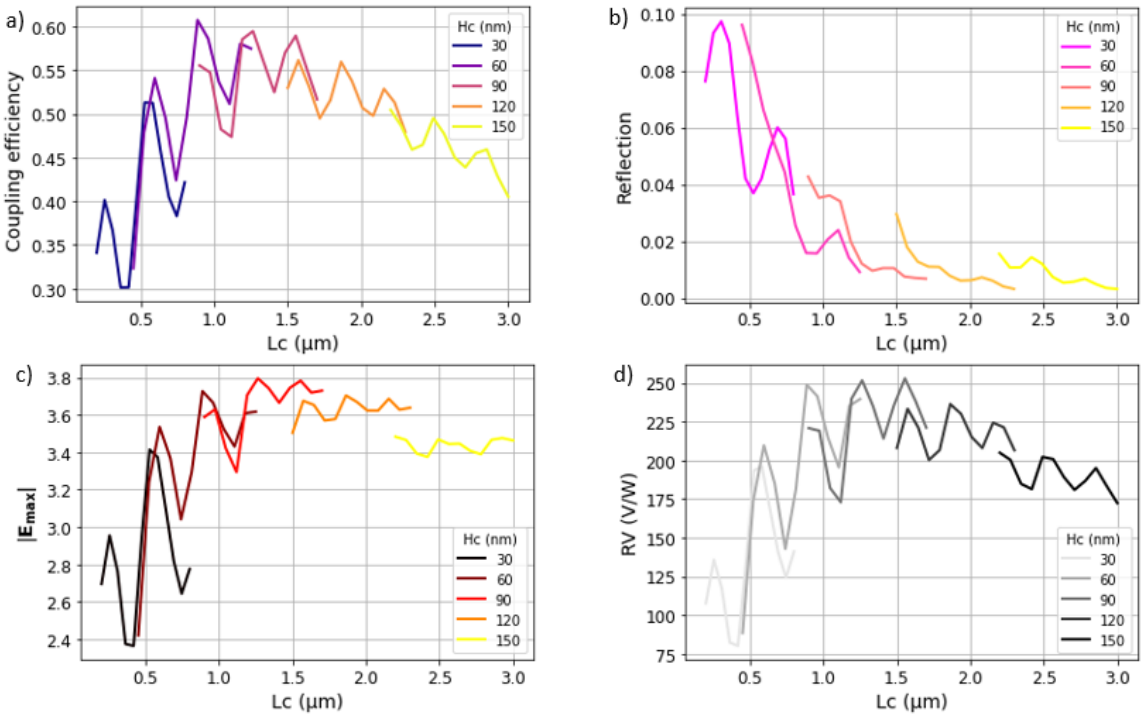

Figure 7.9 (a) Coupling efficiency (b) reflected power (c) maximum electric field strength attained across the center of the graphene plane (x = 0) (d) RV. Each curve represents fixed value of Hc for a range of Lc.

Figure 7.9 shows the total reflection curves for different Hc as a function of Lc. Hc affects both the reflected power during the transition from the pure WG modes (region I, III) to the states of the hybrid region ($\Psi_e - \Psi_o$ *and* $\Psi_e + \Psi_o$) as well as the phase evolution during. The general trend is indicative of the minimization of measured reflections as the hybrid mode effective indices approach the common neff with increasing Hc and as power absorption from the plasmonic WG reduces the backward propagating power. Coupling efficiency maxima coincide with reflection local minima reaching maximum values of 60% around Hc = 90 nm and Lc ~ 1.5 μm when reflections have essentially gone to 0. Further increasing the coupling length just adds plasmonic losses at the hybrid region and thus coupling efficiency decreases. The maximum electric field strength figure 7.9c exhibits similar behavior with smaller changes relative to the coupling efficiency. The voltage responsivity figure 7.9 d shows a mixed correlation with contributions of both the coupling efficiency, affecting graphene total absorption and the maximum electric field affecting absorption density. All data indicate that a large portion of power is dissipated in the hybrid region while maximum electric field strength is reached at the interface between region II-III. In order to harness this power, the placing of graphene should be at the interface between regions II-III capturing only the strongest of electric

fields. Fixed bulk-surface relaxation time has been used for all simulations but in reality, relaxation times are substrate dependent and change around the boundary. Figure 7.10 reports thermoelectric simulations for coupling parameters Hc =120 nm, Lc = 2 μm, having the graphene channel centered at the II-III interface and symmetrically reducing the total length L of the device for a variety of relaxation time combinations. The reduction of length leads to larger average absorption densities as the device gets smaller, absorbing only the strongest part of the electric field. Peak RV values vary from ~ 0.5 to 1.5 μm dependent on the magnitude of the difference between the bulk and surface values of relaxation time. As the length increases the curves eventually converge indicating the

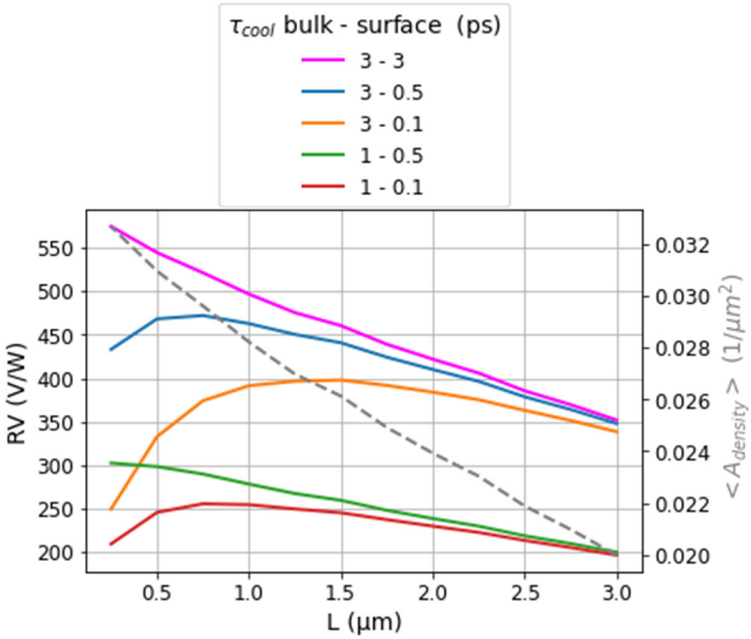

Figure 7.10 RV as a function of device length and surface-bulk cooling times (left y axis) and Average device absorption density (right y axis)

dominance of the bulk relaxation time at larger device lengths. Even with the lowest estimates available for τ a value of RV above 250 V/W is a remarkable result outperforming the current state of the art PD devices by at least a factor of 2.5.

8 Model accuracy

8.1 Simulation of experimentally realized devices

This section of the thesis describes an attempt to leverage all the tools presented in previous sections to create accurate models of experimentally realized devices and assess the accuracy of the model by comparing simulated and measured quantities. Table 1 provides information on the setup of simulated reference devices. Figure 8.1 is a graph of simulated vs measured voltage responsivities. The variation in result fidelity is attributed different electron-phonon interactions based on substrate -superstrate material. This is encouraged by the fact that the most accurate of reference is the one featuring full hBN encapsulation[13] while the next most accurate features single layer hBN between the device and Si3N4 spacer[4] while the most inaccurate is the one lacking any hBN protection [3]. Using a unified relaxation time and accounting for power effects provides a universal measure of device performance processing good predictive capability in spite of variation in experimental device setups.

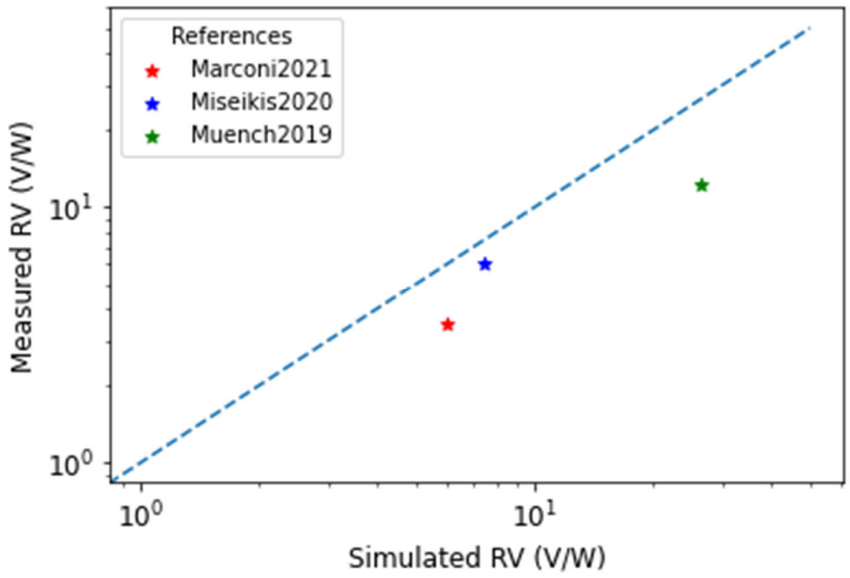

Figure 8.1 Measured vs simulated voltage responsivity, τ = 1 ps

Table 1 Device setup and simulated-experimental results

References	*Marconi 2021*	*Miseikis 2020*	*Muench 2019*
Gate dielectric thickness t_g	0.1	0.12	0.03
Split-gate gap w_{gap}	0.15	1	0.05
S-D distance W	1.5	10	5
Device length L	50	80	3
SLG - WG coupling distance t_{WG}	0.025	0.025	0.03
WG – spacer – gate materials	Si-Si3N4-Gr	Si3N4–PVA-Gr	Au-Al2O3-Au
WG thickness h	0.22	0.26	0.06
WG width w	0.48	1.2	0.11
Source	TE 1550 nm	TE 1550 nm	TE 1550 nm
Bulk electron cooling time τ (ps)	1	1	1
Surface electron cooling time τ_s (ps)	0.5	0.5	0.5
carrier mobility μ ($\frac{cm^{-2}}{VS}$)	3125	16000	2000
residual local charge n^*(cm^{-2})	7.00E+11	8.00E+10	7.00E+12
RV simulated ($\frac{V}{W}$)	6.015	7.48	26.5
RV measured ($\frac{V}{W}$)	3.5	6	12.2
Input power Pin (mW)	1.65	0.7	0.07

8.2 Theoretical solution

In this section a solution is produced for the thermoelectric equation based on purely theoretical means following the logic laid out in recent publications [50]. The goal is to produce a solution that captures the key physical trends of the system and showcases the limitations of such approaches. We begin by solving the 1D heat equation eq 8.1 and prescribing

$$\frac{\partial^2 \Delta T}{\partial x^2} - \frac{1}{\xi^2}\Delta T = \delta(x - x0),\ \frac{1}{\xi^2} = \frac{Ce}{\kappa\tau} \qquad (8.1)$$

boundary conditions figure 8.2. We obtain the solutions to the homogeneous PDE in Region I, II by enforcing boundary conditions and continuity at $x = x_0$.

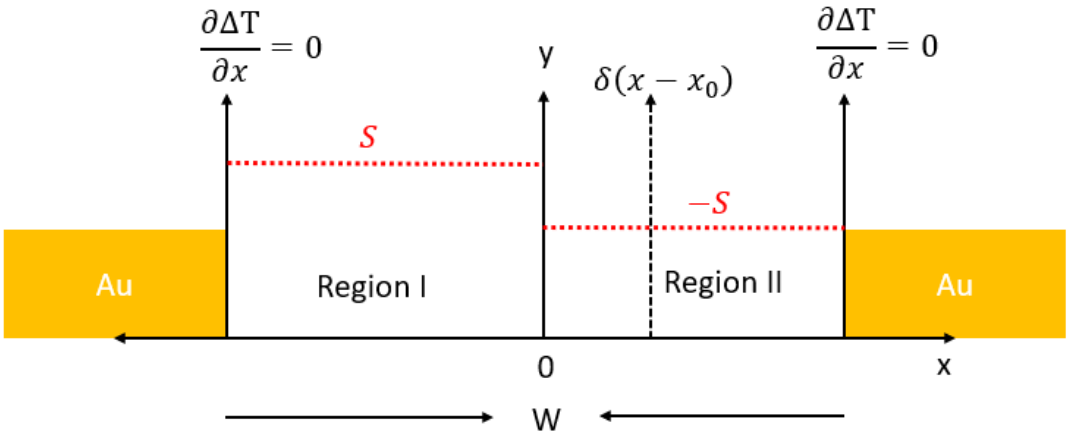

Figure 8.2 Schematic diagram of the problem parameters

$$\Delta T_I = c\, e^{\frac{w}{2\xi}} \cosh\left(\frac{w}{2\xi} + \frac{x}{\xi}\right), \Delta T_{II} = c\, e^{\frac{w}{2\xi}} \cosh\left(\frac{w}{2\xi} - \frac{x}{\xi}\right) \delta(x_0) \qquad (8.2)$$

$$\delta(x_0) = \frac{\cosh\left(\frac{w}{2\xi} - x_0\right)}{\cosh\left(\frac{w}{2\xi} + x_0\right)}$$

In order for the solution to account for the source term $\sim\delta(x - x_0)$, another constraint has to be applied through limit integral equation essentially forcing the discontinuity of the derivative to be proportional to the amplitude of the source term.

$$\lim_{\varepsilon\to 0}\int_{x_0-\varepsilon}^{x_0+\varepsilon} \frac{\partial^2 \Delta T}{\partial x^2}\, dx - \lim_{\varepsilon\to 0}\int_{x_0-\varepsilon}^{x_0+\varepsilon} \frac{1}{\xi^2}\Delta T\, dx = \lim_{\varepsilon\to 0}\int_{x_0-\varepsilon}^{x_0+\varepsilon} \frac{q}{\kappa}\, \delta(x - x_0)\, dx$$

Thus, we finally obtain the last constant $c = \frac{\frac{q}{\kappa}\xi e^{-\frac{w}{2\xi}}}{\beta(x_0)}$, where $\beta(x_0) = \sinh\left(\frac{w}{2\xi} - \frac{x_0}{\xi}\right) + \delta(x_0)\sinh\left(\frac{w}{2} + \frac{x_0}{\xi}\right)$. The Green s function is defined through it's fundamental property $L\, G(x, x_0) = \delta(x, x_0)$, this property can be exploited to solve differential equations of the form $L\ u(x) = f(x)$. Loosely speaking, if such a function G can be found for a linear operator

$$\int L\, G(x, x_0)\, A(x_0)\, dx_0 = \int \delta(x - x_0)\ A(x_0)\, dx_0$$

$$L\ \left(\int\ G(x, x_0)\, A(x_0)\, dx_0\ \right) = A(x)$$

which means that the solution is

$$\Delta T = \int\ G(x, x_0)\, A(x_0)\, dx_0 \quad (8.3)$$

For the heating source $Q_s(x)$ we will approximate the absorption density function with a gaussian $g(x)$, obtaining $\sigma_g = \frac{FWHM}{2.35}$ from the absorption curve, times a fractional term a that represents average power per unit length absorbed based on the absorption length L_a and the length L of the photodetector.

$$g(x) = \frac{1}{(2\pi)^{-\frac{1}{2}}\sigma_g} e^{-\frac{x^2}{2\sigma_g^2}} \quad a = \frac{1 - e^{-\frac{L}{L_a}}}{L}\ \ Q_s(x) = a\ Pin\ g(x)$$

Using eq 8.3 we can then write the solution as

$$\Delta T_s = \int_{-\frac{w}{2}}^{\frac{w}{2}} \frac{dx_0}{\sqrt{2\pi}\sigma_g} e^{-\frac{-x_0^2}{2\sigma_g^2}} \frac{a\ Pin\ \xi}{\kappa\ \beta(x_0)} \times \begin{Bmatrix} \cosh\left(\frac{w}{2\xi} - \frac{x}{\xi}\right)\ x > x_0 \\ \delta(x_0)\cosh\left(\frac{w}{2\xi} + \frac{x}{\xi}\right)\ x < x_0 \end{Bmatrix} \quad (8.4)$$

$L\ = \frac{\partial^2}{\partial x} - \frac{1}{\xi}$ is a linear operator. Exploiting the linearity of the differential operator we can try to incorporate some of the terms of the thermoelectric equation as sources. The final solution will be a superposition of all the minor solutions $\Delta T = \Delta T_s + \Delta T_p$. Expanding some of the terms of the thermoelectric equation we identify the most important terms.

$$\Pi = ST, \qquad j = \sigma S\frac{\partial T}{\partial x}, \qquad j\frac{\partial \Pi}{\partial x} = \sigma S\frac{\partial T}{\partial x}\left(\frac{\partial s}{\partial x}T + S\frac{\partial T}{\partial x}\right)$$

$$T\frac{\Delta S}{\Delta x} \sim 10^5\ \ S\frac{\Delta S}{\Delta x} \sim 10^2$$

Thus, we can approximate the Peltier cooling term as $Q_p(x) = -T_0\sigma S\frac{\partial T}{\partial x}\frac{\partial S}{\partial x}$, with $\frac{\partial S}{\partial x} = 2S\delta(x)$ because S is a step function and $\frac{\Delta T}{\Delta x} \sim \frac{\Delta T_s}{\frac{w_{gap}}{2}}$ for small w_{gap} meaning

$$Q_p(x) = q_p\delta(x),\ q_p = -\frac{4S^2\kappa}{L_0 w_{gap}}\left(\Delta T_s|_{x=0} - \Delta T_s|_{x=\frac{w_{gap}}{2}}\right) \qquad (8.5)$$

The solution for the Peltier source is

$$\Delta T_p = \frac{q_p\xi}{2\,\kappa\,\sinh\left(\frac{w}{2\xi}\right)}\cosh\left(\frac{w}{2\xi} - abs(x)\right) \qquad (8.5)$$

Now extending this solution to the 2D we are expecting a solution form $\Delta T(z) \sim e^{-\frac{z}{\psi}}$ similar to the source term, assuming ψ is much larger then ξ. The thermoelectric voltage can then be calculated as

$$V_{PTE} = \frac{1}{L}\iint S(x)\frac{\partial \Delta T(x,z)}{\partial x}\,dxdz$$

$$V_{PTE} = 2S\left(\Delta T|_{x=0} - \Delta T|_{x=\frac{w}{2}}\right)\frac{\psi}{L}\left(1 - e^{-\frac{L}{\psi}}\right)$$

For small devices where $z = \frac{L}{L_a} \ll 1$, $a(z) \sim La\big(1-(1-z)\big)/z \sim constant$ meaning average absorption per unit length doesn't change and therefore ψ remains much larger than L meaning $\frac{\psi}{L}\left(1 - e^{-\frac{L}{\psi}}\right) \to 1$. The resulting temperature distributions 8.3 a and temperature gradients 8.3 are compared with different heating sources and corresponding numerical results. The delta function heating source represents the upper physical limit solution featuring the standard hyperbolic decay reaching RV = 210 V/W. For a gaussian heating source of FWHM = 0.4 μm the solution starts to resemble the numerical solution reaching an RV = 163 V/W. After we obtain the heating source, we can apply the Peltier cooling for a w_{gap} = 150 nm we obtain the final result of RV = 143 V/W which is unexpectedly close to the numerical 90 V/W considering we have ignored any temperature decay

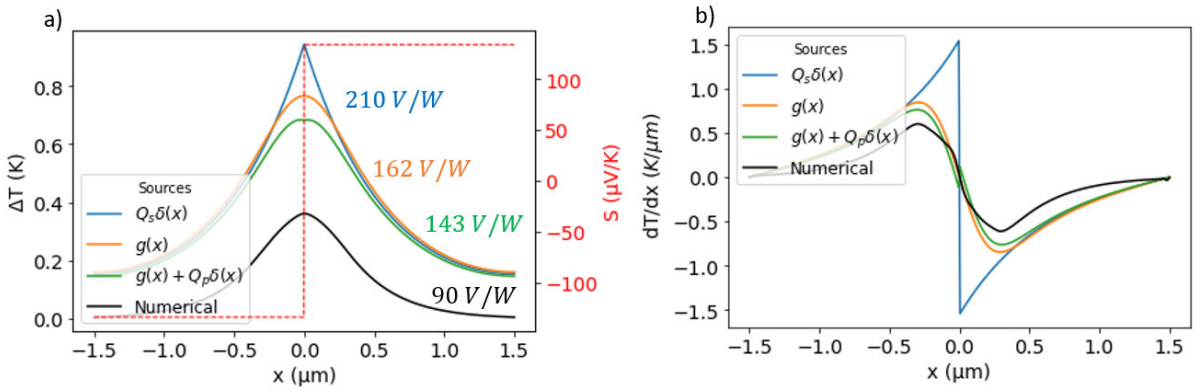

Figure 8.3 Temperature (a) and gradient (b) distributions for different sources approximations (theoretical) and numerical solutions.

in the z and additional cooling effects as well as the Fermi function distribution and the associated changes in cooling length inside the gap area. The theoretical solution shows a linear reduction in cooling as the gap size approaches 0, as expected since $\frac{dT}{dx}$ is linear near x = 0, overestimating the

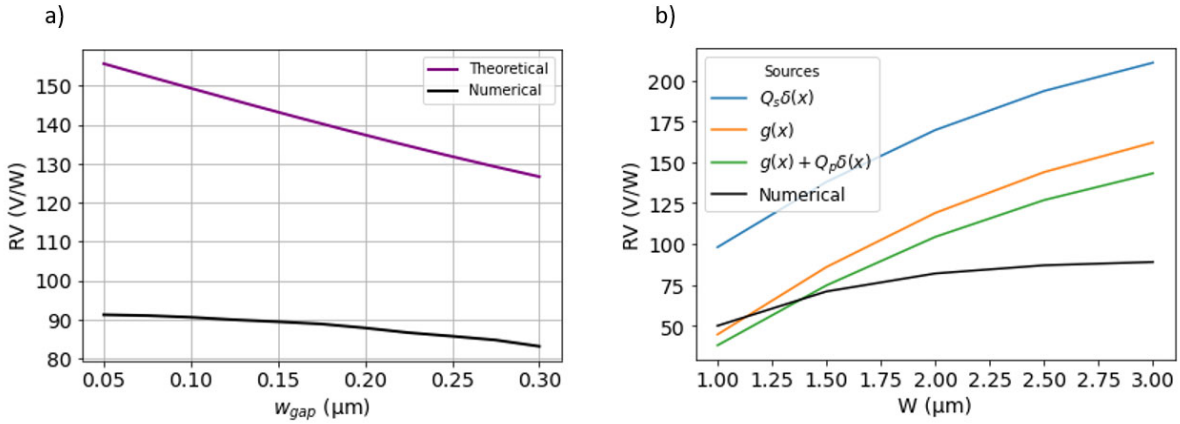

Figure 8.4 (a) RV as a function of gap size. (b) RV as a function of W.

cooling effects. Comparing numerical and theoretical solution for RV as a function of channel width we see that the theoretical solution tends to converge faster due to increased cooling effects.

9 Conclusions

In the split gate graphene device setup WG cross-section manipulation yielded an up to two-fold increase in absorption density. Gap size was shown to affect device performance when $w_{gap} \ll FWHM$ while spacer thickness became relevant for aspect ratios of $\frac{t_{SiN}}{w_{gap}} \ll 1$. The inclusion of a different surface cooling time allowed for a meaningful prediction of device optimum length while offering a way to indirectly probe the relative strength of cooling (τ) in surface-bulk areas by looking at the position of trend reversal from bulk to surface dominated cooling. Channel width affects device performance in three major ways. Mode hybridization with surface plasmon polaritons facilitated by the evanescent character of WG mode, by modulating temperature relaxation and controlling device resistance. For pristine graphene devices, $\tau \sim ps$, and power densities of the order of $70\ \frac{\mu W}{\mu m^2}$ the center of the device reaches temperatures upwards of 500 K and RV reduces by up to ~ 30%. This drop in performance stems from a temperature induced shift in dynamics where by lattice relaxation becomes dominant cooling mechanism while diffusive transport reverses at the hotspot. Simulations regarding the slot gate device showed that reducing cross sectional parameter Wp increased absorption density while decreasing absorption area. These two competing mechanisms led to peak absorption around Wp = 75 nm while RV kept increasing with further reduction due to gap size effects. Si WG-plasmonic slot WG directional coupling achieved coupling efficiency of 60 %. Electric field strength steadily increases in the hybrid region reaching its climax near the interface of regions III-II. Further length optimization, positioning graphene centered on the interface, yielded voltage responsivities of 500-250 V/W a 5 to 2.5-fold increase from the current state of the art graphene PDs. Simulation of experimental devices follows closely experimental results with result fidelity affected mainly by the uncertainty in electron phonon relaxation times. Finally, we produce a purely theoretical solution using Green's functions, eliminating low order terms, incorporating the heating distribution and substituting differential terms with approximate source terms. The aim is to give intuition and showcase the degree of success in such approaches as well as further validation of existing numerical results. The theoretical solution captures the essential physical trends of the system, offering a reliable back test to numerical results.

REFERENCES

[1] M. Casalino, G. Coppola, M. Iodice, I. Rendina, and L. Sirleto, "Near-infrared sub-bandgap all-silicon photodetectors: State of the art and perspectives," *Sensors*, vol. 10, no. 12, pp. 10571–10600, 2010, doi: 10.3390/s101210571.

[2] J. Michel, J. Liu, and L. C. Kimerling, "High-performance Ge-on-Si photodetectors," *Nat. Photonics*, vol. 4, no. 8, pp. 527–534, 2010, doi: 10.1038/nphoton.2010.157.

[3] J. E. Muench *et al.*, "Waveguide-Integrated, Plasmonic Enhanced Graphene Photodetectors," *Nano Lett.*, vol. 19, no. 11, pp. 7632–7644, 2019, doi: 10.1021/acs.nanolett.9b02238.

[4] S. Marconi *et al.*, "Photo thermal effect graphene detector featuring 105 Gbit s−1 NRZ and 120 Gbit s−1 PAM4 direct detection," *Nat. Commun.*, vol. 12, no. 1, pp. 1–10, 2021, doi: 10.1038/s41467-021-21137-z.

[5] I. Goykhman *et al.*, "On-Chip Integrated, Silicon-Graphene Plasmonic Schottky Photodetector with High Responsivity and Avalanche Photogain," *Nano Lett.*, vol. 16, no. 5, pp. 3005–3013, 2016, doi: 10.1021/acs.nanolett.5b05216.

[6] M. Romagnoli *et al.*, "Graphene-based integrated photonics for next-generation datacom and telecom," *Nat. Rev. Mater.*, vol. 3, no. 10, pp. 392–414, 2018, doi: 10.1038/s41578-018-0040-9.

[7] F. Luo *et al.*, "High responsivity graphene photodetectors from visible to near-infrared by photogating effect," *AIP Adv.*, vol. 8, no. 11, 2018, doi: 10.1063/1.5054760.

[8] L. Viti *et al.*, "Thermoelectric graphene photodetectors with sub-nanosecond response times at terahertz frequencies," *Front. Opt. Photonics*, vol. 10, no. 1, pp. 89–98, 2021, doi: 10.1515/9783110710687-007.

[9] S. Castilla *et al.*, "Fast and Sensitive Terahertz Detection Using an Antenna-Integrated Graphene pn Junction," *Nano Lett.*, vol. 19, no. 5, pp. 2765–2773, 2019, doi: 10.1021/acs.nanolett.8b04171.

[10] R. J. Shiue *et al.*, "High-Responsivity Graphene-Boron Nitride Photodetector and Autocorrelator in a Silicon Photonic Integrated Circuit," *Nano Lett.*, vol. 15, no. 11, pp. 7288–7293, 2015, doi: 10.1021/acs.nanolett.5b02368.

[11] P. Ma *et al.*, "Plasmonically Enhanced Graphene Photodetector Featuring 100 Gbit/s Data Reception, High Responsivity, and Compact Size," *ACS Photonics*, vol. 6, no. 1, pp. 154–161, 2019, doi: 10.1021/acsphotonics.8b01234.

[12] I. Vangelidis *et al.*, "Unbiased Plasmonic-Assisted Integrated Graphene Photodetectors," 2022, doi: 10.1021/acsphotonics.2c00100.

[13] V. Mišeikis *et al.*, "Ultrafast, Zero-Bias, Graphene Photodetectors with Polymeric Gate Dielectric on Passive Photonic Waveguides," *ACS Nano*, vol. 14, no. 9, pp. 11190–11204, 2020, doi: 10.1021/acsnano.0c02738.

[14] S. Schuler *et al.*, "High-responsivity graphene photodetectors integrated on silicon microring resonators," *Nat. Commun.*, vol. 12, no. 1, pp. 1–9, 2021, doi: 10.1038/s41467-021-23436-x.

[15] K. S. Novoselov, V. I. Fal'Ko, L. Colombo, P. R. Gellert, M. G. Schwab, and K. Kim, "A roadmap for graphene," *Nature*, vol. 490, no. 7419, pp. 192–200, 2012, doi: 10.1038/nature11458.

[16] P. R. Wallace, "The Band Theory of Graphite," *Phys. Rev.*, vol. 71, no. 9, pp. 622–634, 1947, doi: 10.2208/jsceja.64.452.

[17] A. Maffucci and G. Miano, "Electrical properties of graphene for interconnect applications," *Appl. Sci.*, vol. 4, no. 2, pp. 305–317, 2014, doi: 10.3390/app4020305.

[18] V. P. Gusynin, S. G. Sharapov, and J. P. Carbotte, "Unusual microwave response of dirac quasiparticles in graphene," *Phys. Rev. Lett.*, vol. 96, no. 25, pp. 1–4, 2006, doi: 10.1103/PhysRevLett.96.256802.

[19] M. Wilson, "Electrons in atomically thin carbon sheets behave like massless particles," *Phys. Today*, vol. 59, no. 1, pp. 21–23, 2006, doi: 10.1063/1.2180163.

[20] K. S. Novoselov *et al.*, "Two-dimensional gas of massless Dirac fermions in graphene," *Nature*, vol. 438, no. 7065, pp. 197–200, 2005, doi: 10.1038/nature04233.

[21] L. A. Falkovsky, "Optical properties of graphene," *J. Phys. Conf. Ser.*, vol. 129, 2008, doi: 10.1088/1742-6596/129/1/012004.

[22] Y. W. Tan *et al.*, "Measurement of scattering rate and minimum conductivity in graphene," *Phys. Rev. Lett.*, vol. 99, no. 24, pp. 10–13, 2007, doi: 10.1103/PhysRevLett.99.246803.

[23] G. W. Hanson, "Dyadic Green's functions and guided surface waves for a surface conductivity model of graphene," *J. Appl. Phys.*, vol. 103, no. 6, 2008, doi: 10.1063/1.2891452.

[24] V. G. Kravets *et al.*, "Spectroscopic ellipsometry of graphene and an exciton-shifted van Hove peak in absorption," *Phys. Rev. B - Condens. Matter Mater. Phys.*, vol. 81, no. 15, pp. 1–6, 2010, doi: 10.1103/PhysRevB.81.155413.

[25] Z. Q. Li *et al.*, "Dirac charge dynamics in graphene by infrared spectroscopy," *Nat. Phys.*, vol. 4, no. 7, pp. 532–535, 2008, doi: 10.1038/nphys989.

[26] Lumerical inc., "No Title." https://www.lumerical.com/products/fdtd/

[27] A. Taflove and S. C. Hagness, *The Finite-Difference Time-Domain Method Third Edition*. 2005.

[28] K. S. YEE, "Numerical Solution of Initial Boundary Value Problems Involving Maxwell's Equations in Isotropic Media," 1965, doi: 10.1007/978-3-319-61185-3_17.

[29] P. B. Johnson and R. W. Christy, "Optical Constant of the Nobel Metals," *Phys. Rev. B*, vol. 6, no. 12, pp. 4370–4379, 1972.

[30] K. Luke, Y. Okawachi, M. R. E. Lamont, A. L. Gaeta, and M. Lipson, "Broadband mid-infrared frequency comb generation in a Si3N4 microresonator," *Conf. Lasers Electro-Optics Eur. - Tech. Dig.*, vol. 2015-Augus, no. 21, pp. 4823–4826, 2015, doi: 10.1364/ol.40.004823.

[31] I. H. Malitson, "Interspecimen Comparison of the Refractive Index of Fused Silica*,†," *J. Opt. Soc. Am.*, vol. 55, no. 10, p. 1205, 1965, doi: 10.1364/josa.55.001205.

[32] H. H. Li, "Refractive index of silicon and germanium and its wavelength and temperature derivatives," *J. Phys. Chem. Ref. Data*, vol. 9, no. 3, pp. 561–658, 1980, doi: 10.1063/1.555624.

[33] G. Dabos *et al.*, "Water Cladded Plasmonic Slot Waveguide Vertically Coupled with Si3N4 Photonics," *IEEE Photonics J.*, vol. 10, no. 3, pp. 1–8, 2018, doi: 10.1109/JPHOT.2018.2832461.

[34] Q. Li and M. Qiu, "Structurally-tolerant vertical directional coupling between metal-insulator-metal plasmonic waveguide and silicon dielectric waveguide," *Opt. Express*, vol. 18, no. 15, p. 15531, 2010, doi: 10.1364/oe.18.015531.

[35] J. Tian, S. Yu, W. Yan, and M. Qiu, "Broadband high-efficiency surface-plasmon-polariton coupler with silicon-metal interface," *Appl. Phys. Lett.*, vol. 95, no. 1, pp. 3–6, 2009, doi: 10.1063/1.3168653.

[36] X. Sun, D. Dai, L. Thylén, and L. Wosinski, "High-sensitivity liquid refractive-index sensor based on a Mach-Zehnder interferometer with a double-slot hybrid plasmonic waveguide," *Opt. Express*, vol. 23, no. 20, p. 25688, 2015, doi: 10.1364/oe.23.025688.

[37] A. Messner *et al.*, "Plasmonic ferroelectric modulators," *J. Light. Technol.*, vol. 37, no. 2, pp. 281–290, 2019, doi: 10.1109/JLT.2018.2881332.

[38] J. C. W. Song and L. S. Levitov, "Energy flows in graphene: Hot carrier dynamics and cooling," *J. Phys. Condens. Matter*, vol. 27, no. 16, p. 164201, 2015, doi: 10.1088/0953-8984/27/16/164201.

[39] Q. Ma *et al.*, "Competing channels for hot-electron cooling in graphene," *Phys. Rev. Lett.*, vol. 112, no. 24, pp. 1–5, 2014, doi: 10.1103/PhysRevLett.112.247401.

[40] N. M. Gabor *et al.*, "Hot carrier-assisted intrinsic photoresponse in graphene," *Science (80-.).*, vol. 334, no. 6056, pp. 648–652, 2011, doi: 10.1126/science.1211384.

[41] J. C. W. Song, M. S. Rudner, C. M. Marcus, and L. S. Levitov, "Hot carrier transport and photocurrent response in graphene," *Nano Lett.*, vol. 11, no. 11, pp. 4688–4692, 2011, doi: 10.1021/nl202318u.

[42] E. H. Hwang, E. Rossi, and S. Das Sarma, "Theory of thermopower in two-dimensional graphene," *Phys. Rev. B - Condens. Matter Mater. Phys.*, vol. 80, no. 23, pp. 1–5, 2009, doi: 10.1103/PhysRevB.80.235415.

[43] J. C. Johannsen *et al.*, "Direct view of hot carrier dynamics in graphene," *Phys. Rev. Lett.*, vol. 111, no. 2, pp. 1–5, 2013, doi: 10.1103/PhysRevLett.111.027403.

[44] K. J. Tielrooij *et al.*, "Photoexcitation cascade and multiple hot-carrier generation in graphene," *Nat. Phys.*, vol. 9, no. 4, pp. 248–252, 2013, doi: 10.1038/nphys2564.

[45] K. F. Mak, C. H. Lui, and T. F. Heinz, "Measurement of the thermal conductance of the graphene/ SiO2 interface," *Appl. Phys. Lett.*, vol. 97, no. 22, 2010, doi: 10.1063/1.3511537.

[46] L. Chen, Z. Yan, and S. Kumar, "Coupled electron-phonon transport and heat transfer pathways in graphene nanostructures," *Carbon N. Y.*, vol. 123, pp. 525–535, 2017, doi: 10.1016/j.carbon.2017.07.095.

[47] G. Soavi *et al.*, "Broadband, electrically tunable third-harmonic generation in graphene," *Nat. Nanotechnol.*, vol. 13, no. 7, pp. 583–588, 2018, doi: 10.1038/s41565-018-0145-8.

[48] M. Cutler, "Observation of Anderson Localization in an Electron Gas," vol. 181, no. 3, 1969.

[49] B. Canto *et al.*, "Plasma-Enhanced Atomic Layer Deposition of Al2O3 on Graphene Using Monolayer hBN as Interfacial Layer," *Adv. Mater. Technol.*, vol. 6, no. 11, pp. 21–24, 2021, doi: 10.1002/admt.202100489.

[50] A. Antidormi and A. W. Cummings, "Optimizing the Photothermoelectric Effect in Graphene," *Phys. Rev. Appl.*, vol. 15, no. 5, p. 1, 2021, doi: 10.1103/PhysRevApplied.15.054049.

APPENDIX

Importing python 3 libraries

```
import numpy as np
import matplotlib.pyplot as plt
import scipy.integrate
import scipy.interpolate as interpolate
from sympy import re, im, I
import math
from numba import njit
from numba import jit
import pandas as pd
import seaborn as sns
```

Constants

```
kb = 8.61733*10**(-5)
hbar = 6.582 * 10**(-16)
v_F = 1*10**6
pi = np.pi
ε0 = 8.854187817*10**-12
t_gr = 0.335*10**-9
e = 1.60217662*10**-19
c = 299792458
Lor = 2.44*10**-8
```

Thermodynamic quantities integral calculation

```
def get_mew(nq,temp):

# symbols

ε,μ,T,x = symbols("ε,μ,T,x",real = True)

# constants

kb = 8.61733*10**(-5)
hbar = 6.582 * 10**(-16)
```

```
t_gr = 0.335*10**-9
pi = np.pi
ε0 = 8.854187817*10**-12
e = 1.60217662*10**-19
c = 299792458
v_F = 1*10**6

# we need to solve the equation (EF/pi*habr*vF)**2 = ne(μ,T)+nh(μ,T)
# Calculate the integral numericly and solve the resulting equation for μ


# symbolic expressions
pi = np.pi
β = 1/(kb*T)
FDe = 1/(exp(β*(ε-μ))+1)
FDh = 1/(exp(β*(ε+μ))+1)
g = (2*ε)/(pi*(hbar*v_F)**2)
expr = g*(FDe-FDh)
f_mew = lambdify((ε,μ,T),expr,modules = "numpy")


#
mu1 = -0.5
mu2 = 0.5
nq1,err = scipy.integrate.quad(f_mew,0,np.Inf,args=(mu1,temp))
nq2,err = scipy.integrate.quad(f_mew,0,np.Inf,args=(mu2,temp))

while abs(mu2 - mu1)/mu2 > 10**-5:
muc = (mu1 + mu2)/2
nqc,err = scipy.integrate.quad(f_mew,0,np.Inf,args=(muc,temp))
if nq > nqc:
mu1 = muc
nq1 = nqc
else:
mu2 = muc
nq2 = nqc
#print(muc)
return muc



#limits transform
def integrant(expr,transform):
# symbols
```

```
ε,μ,T,x = symbols("ε,μ,T,x",real = True)
iota = expr.subs(ε,transform)
α = transform.diff(x) # dε/dx = α
expr2 = iota*α

return expr2



# cv = d<ε>/dT and central derivative is [f(T+dT/2)-f(T-dT/2)]/DT
def get_cv(E_F,temp,dT):

# symbols
if E_F ==0 : E_F = 10**-5
ε,μ,T,x = symbols("ε,μ,T,x",real = True)

#constants

kb = 8.61733*10**(-5)
hbar = 6.582 * 10**(-16)
t_gr = 0.335*10**-9
pi = np.pi
ε0 = 8.854187817*10**-12
e = 1.60217662*10**-19
c = 299792458
v_F = 1*10**6


# symbolic expressions
β = 1/(kb*T)
FD = 1/(exp(β*(ε-μ))+1)
FD_ = 1/(exp(β*(-ε-μ))+1)
g = (2*ε)/(pi*(hbar*v_F)**2)
if E_F ==0 : E_F = 10**-5
n0 = E_F**2/(pi*(hbar*v_F)**2)

#dT = temp/10
mew2 = get_mew(n0,temp+dT/2)
mew1 = get_mew(n0,temp-dT/2)

expr= g*ε*(FD+FD.subs(μ,-μ))

f  = lambdify((ε,μ,T),expr,modules = "numpy")
cv2, err = scipy.integrate.quad(f,0,1,args = (mew2,temp+dT/2))
```

```
cv1, err = scipy.integrate.quad(f,0,1,args = (mew1,temp-dT/2))
cv = (cv2-cv1)/dT
cv = cv*e
return cv



def get_cond0(E_F,nres,mobe,mobh):

#constants

kb = 8.61733*10**(-5)
hbar = 6.582 * 10**(-16)
t_gr = 0.335*10**-9
pi = np.pi
ε0 = 8.854187817*10**-12
e = 1.60217662*10**-19
c = 299792458

#  n in 2D materials is in m^-2
n = E_F**2/(pi*(hbar*v_F)**2)
n = n*10**-4 # if nres and mobe are in cm we should convert n in cm too
nstar = np.sqrt( n**2 + nres**2 ) - n
mob_bar = (mobe+mobh)/2
σ0 = e*(mobe*n+mob_bar*nstar)

return σ0


def get_cond(E_F,temp,nres,mob):

# nres and mobilities in cm**-2
pi = np.pi
kb = 8.61733*10**(-5)
e = 1.60217662*10**-19
ε0 = 8.854187817*10**-12
hbar = 6.582 * 10**(-16)
v_F = 10**6
nres = nres*10**4 # cm**-2 --> m**-2
mob = mob*10**-4
if E_F ==0 : E_F = 10**-5
n0 =  E_F**2/(pi*(hbar*v_F)**2)
mew = get_mew(n0,temp)
```

```
ε,μ,T,x = symbols("ε,μ,T,x",real = True)
# symbolic expressions
β = 1/(kb*T)
FD = 1/(exp(β*(ε-μ))+1)
FD_ = 1/(exp(β*(-ε-μ))+1)
g = (2*ε)/(pi*(hbar*v_F)**2)

if E_F < 0 :
mew = -mew

nε = ε**2/(pi*hbar**2*v_F**2)
σε = e*mob*sqrt(nε**2+nres**2)
expr = σε*FD.diff(ε)

f = lambdify((ε,μ,T),expr,modules = "numpy")

sigma, err = scipy.integrate.quad(f,-1,1,args=(mew,temp))

return sigma



def get_seebeck(E_F,temp,nres,mob):

# symbols

ε,μ,T,x = symbols("ε,μ,T,x",real = True)

# nres and mobilities in cm**-2
σ = get_cond(E_F,temp,nres,mob)

kb = 8.61733*10**(-5)
pi = np.pi
ε0 = 8.854187817*10**-12
e = 1.60217662*10**-19
hbar = 6.582 * 10**(-16)
v_F = 10**6
nres = nres*10**4 # cm**-2 --> m**-2
mob = mob*10**-4
if E_F ==0 : E_F = 10**-5
n0 =  E_F**2/(pi*(hbar*v_F)**2)
mew = get_mew(n0,temp)

# symbolic expressions
β = 1/(kb*T)
```

```
FD = 1/(exp(β*(ε-μ))+1)
FD_ = 1/(exp(β*(-ε-μ))+1)
g = (2*ε)/(pi*(hbar*v_F)**2)

if E_F < 0 :
mew = -mew


factor = 1/(-temp*σ)
nε = ε**2/(pi*hbar**2*v_F**2)
σε = e*mob*sqrt(nε**2+nres**2)
expr = (ε-μ)*σε*FD.diff(ε)


f = lambdify((ε,μ,T),expr,modules = "numpy")

S, err = scipy.integrate.quad(f,-1,1,args=(mew,temp))

return factor*S



def get_dielectric(λ,mew,temp,τ):

# symbols

ε,μ,T,x = symbols("ε,μ,T,x",real = True)

# symbolic expressions
ε0 = 8.854187817*10**-12
kb = 8.61733*10**(-5)
pi = np.pi
e = 1.60217662*10**-19
hbar = 6.582 * 10**(-16)
v_F = 10**6

β = 1/(kb*T)
FD = 1/(exp(β*(ε-μ))+1)
FD_ = 1/(exp(β*(-ε-μ))+1)

# constants

hbar = 6.582 * 10**(-16)
Γ = hbar/(2*τ)
hbar_ω = 1240/λ      # λ in nm !
```

```
h = 6.62607004081*10**-34      # now use hbar in SI
hbar = h/(2*pi)


iσinter = (FD_-FD)/((hbar_ω+I*2*Γ)**2-4*ε**2)
iσintra = (-ε*FD_.diff(ε)+ε*FD.diff(ε))
iσinter = integrant(iσinter,x/(1-x))
iσintra = integrant(iσintra,x/(1-x))
fx1 = lambdify((x,μ,T),re(iσinter),modules = "numpy")
fy1 = lambdify((x,μ,T),im(iσinter),modules = "numpy")
fx2 = lambdify((x,μ,T),iσintra,modules = "sympy")
t_gr  = 0.335*10**-9 # graphene thickness
εinfinity  = 6.4
x1,err1 = scipy.integrate.quad(fx1,0,1,args=(mew,temp))
y1,err2 = scipy.integrate.quad(fy1,0,1,args=(mew,temp))
x2,err3 = scipy.integrate.quad(fx2,0,1,args=(mew,temp))

imaginery = hbar*(-2*pow(e, 2)*x2*Γ/(pi*hbar*(pow(hbar_ω, 2) + 4*pow(Γ, 2))) -
pow(e, 2)*(hbar_ω*y1 + 2*x1*Γ)/(pi*hbar))/(e*hbar_ω*t_gr*ε0)
real  =  εinfinity  -  hbar*(-pow(e,  2)*hbar_ω*x2/(pi*hbar*(pow(hbar_ω,  2)  +
4*pow(Γ, 2))) + pow(e, 2)*(hbar_ω*x1 - 2*y1*Γ)/(pi*hbar))/(e*hbar_ω*t_gr*ε0)


return real, imaginery


def get_absorption(λ,mew,temp,tau_ee):

hbar = 6.582 * 10**(-16)
t_gr = 0.335*10**-9
hbar_ω = 1240/λ # λ in nm !
real_diel, imag_diel = get_dielectric(λ,mew,temp,tau_ee)

graphene_absorption = 2*np.pi*t_gr / (1240.0/hbar_ω*10**-9) * imag_diel
return graphene_absorption


@jit(nopython=True)
def Dx(ylist,i,h):
if i == 0 :
derivative = (ylist[i+1]-ylist[i])/h
elif i == ylist.size-1 :
derivative = (ylist[i]-ylist[i-1])/h
else:
derivative = (ylist[i+1]-ylist[i-1])/(2*h)
```

```
return derivative

@jit(nopython=True)
def get_tc(i,j,dhot,dx,dz,imax,jmax,tau_cold,tau_hot):

tau = tau_cold

if i*dx < dhot :
tau = tau_hot
if (imax-i)*dx < dhot :
tau = tau_hot

if j*dz < dhot :
tau = tau_hot
if (jmax-j)*dz < dhot :
tau = tau_hot


return tau
```

Electrostatics and Fermi energy calculation

```
@jit(nopython=True)
def Efermi(dtrans,dx,EF_c,EF_left,EF_right,Ni):
'''
# This function populates the fermi energy with EF_left and EF_right at the
midle and EFtrans
# close to the contacts
# dtrans, the transitional region for fermi matching between the graphene and
metal
# dx grid in the x direction in nm
# EF_c is the fermi energy at the contacts
# Ni is the maximum index in the x direction
'''

EF = np.zeros(Ni)
for i in range(Ni):

imax = Ni

if i < int(Ni/2):
ΔE = EF_c - EF_left
```

```
if i*dx <= dtrans :

EF[i] = EF_c - ΔE*i/(dtrans/dx)
elif (imax-i)*dx <= dtrans :
EF[i] = EF_c - ΔE*(imax-i)/(dtrans/dx)
else:
EF[i] = EF_left

else:

ΔE = EF_c - EF_right


if i*dx <= dtrans :

EF[i] = EF_c - ΔE*i/(dtrans/dx)
elif (imax-i)*dx <= dtrans :
EF[i] = EF_c - ΔE*(imax-1-i)/(dtrans/dx)
else:
EF[i] = EF_right

return EF

@jit(nopython=True)
def Laplace_solution(tox,w,εr,EFl,EFr):
'''
#-------------------------------------------------------------------------
------
#
# solves the 2D Laplace Equation for a split gate geometry
# calculating the fermi energy in the botom graphene sheet
# the model assumes constant voltage values vgl and vgr in the left and right
gates
# and V=0 for the bottom ,solves for the potential and then obtain the
# Fermi level from the surface charge density
#-------------------------------------------------------------------------
-------
'''



def vg_calc(E_F,εr,tox):

ε0 = 8.854187817*10**-12
```

```
e = 1.60217662*10**-19
pi = np.pi
hbar = 6.582 * 10**(-16)
v_F = 1*10**6

n = E_F**2/(pi*(hbar*v_F)**2)
vg = e*n*tox/(ε0*εr)
if E_F < 0 : vg = -vg

return vg

def sigma_to_EF(σ):

ε0 = 8.854187817*10**-12
e = 1.60217662*10**-19
pi = np.pi
hbar = 6.582 * 10**(-16)
v_F = 10**6


EF  = np.sqrt(pi*abs(σ))*hbar*v_F

if σ < 0 :  EF = -EF

EF = -EF

return EF



# PARAMETERS
nm = 10**-9
xl = 500*nm #  legth in the area of interest close to the split
tox = tox*nm  # top-bottom graphene distance
yl = tox
L_sol = xl/nm

w = w*nm # split gate distance
d = 200*nm # domain expansion(bottom top) to let fields decay properly

# find a comfortable dy not too big
# not too small


dy = tox/10
```

```
dx  = dy

dx_virtual = dx/nm

EFbot = 0
EFpin = 0.15


Vgr = vg_calc(EFr,εr,tox)
Vgl = vg_calc(EFl,εr,tox)
Vbot = vg_calc(EFbot,εr,tox)
# domain dimensions (L,H)


L = xl
H = yl+2*d

nx = int(L/dx)  #  structure indices
ny = int(H/dy)

xLmin = 0
xLmax = (xl-w)/2
xRmin = xLmax + w
xRmax = xl

iminL = int(xLmin/dx)
imaxL = int(xLmax/dx)

iminR = int(xRmin/dx)
imaxR = int(xRmax/dx)

iminB = 0
imaxB = int(xl/dx)

jtop = int((yl+d)/dy)
jbot = int(d/dy)


Niter = 100
V = np.zeros((nx,ny))
EF_sol = np.zeros(nx)

# Von neuman boundary conditions dV/dx --> 0 --> Vij+1-Vj = 0 --> Vij+1=Vij
# seting the boundary conditions (capacitor voltage plates)
```

```
# Left gate
for i in range(iminL,imaxL):
V[i,jtop] = Vgl
# right gate
for i in range(iminR,imaxR):
V[i,jtop] = Vgr
#botom graphene
for i in range(iminB,imaxB-1):
V[i,jbot] = Vbot

for n in range(Niter):

for i in range(1,nx-1):
for j in range(1,ny-1):

# Neuman bc next == previus

V[0,:] = V[1,:]
V[-1,:] = V[-2,:]
V[:,0] = V[:,1]
V[:,-1] = V[:,-2]

V[i,j] =0.25*(V[i+1,j]+V[i,j+1]+V[i-1,j]+V[i,j-1])

# force terms

# Left gate
for k in range(iminL,imaxL):
V[k,jtop] = Vgl
# right gate
for l in range(iminR,imaxR):
V[l,jtop] = Vgr
# botom graphene
for m in range(iminB,imaxB):
V[m,jbot] = Vbot


σ = np.zeros(nx)
ε0 = 8.854187817*10**-12
e = 1.60217662*10**-19

res = V

for i in range(nx):
D2 = -εr*ε0*(res[i,jbot+1]-res[i,jbot])/(dx)/e
```

```
D1 = -εr*ε0*(res[i,jbot]-res[i,jbot-1])/(dx)/e
σ[i] = D2-D1


for i in range(nx):
EF_sol[i] =  sigma_to_EF(σ[i])


return EF_sol,L_sol,dx_virtual


def calc_EF(dtrans,dx,EF_c,EF_left,EF_right,Ni,w,tox,εr):
'''
dtrans :  transition region in nm
dx : the step in the x direction in nm
w :  is the gate seperation distance
EF_c :  the fermi level at the contact
Ni : the max x index
EF_left/right : the fermi level at the left/right gate
tox : the thickness of the oxide layer
εr is the dielectric constant of the oxide material

'''

if dx < 10**-3 :
print("dx in nm")
return

EF = Efermi(dtrans,dx,EF_c,EF_left,EF_right,Ni)

EF_sol, L_sol, dx_virtual = Laplace_solution(tox,w,εr,EF_left,EF_right)
# virtual grid used in Laplace solution
dx_ = dx_virtual



nx = int(L_sol/dx)
nx_ = int(L_sol/dx_)
x = np.linspace(-L_sol/2,L_sol/2,nx)
x_ = np.linspace(-L_sol/2,L_sol/2,nx_)
y_ = EF_sol
y = np.zeros(nx)

# now we need to interpolate the values of the virtual grid
# and make a function
```

```
f =  interpolate.interp1d(x_, y_)


# evaluate the function in the real grid
# at the region of intrest (-L_sol/2, L_sol/2)

imidle = int(Ni/2)
ibegin = imidle - int(L_sol/2/dx)
iend  = imidle + int(L_sol/2/dx)


for i in range(ibegin,iend):
EF[i] = f(x[i-ibegin])


return EF
```

Thermoelectric equation coefficients initialization

```
def
init_params(tau,tau_red,tau_ee,EF_contact,dtrans,dhot,dx,dz,Ni,Nj,T0,Pin,A,EF
_left,EF_right,L_split,tSiN,εr,lamda,mob,nstar):

abs0 = get_absorption(lamda,0,T0,tau_ee)

EF = np.zeros(Ni)
τc = np.zeros((Ni,Nj)) # electron - phonon scattering

# dx in nm
nm = 10**-9
if dx < 10**-3:
xstep = dx/nm
h = dx
else:
xstep = dx
h = dx*nm

EF  = calc_EF(dtrans, xstep, EF_c, EF_left, EF_right, Ni, L_split, tSiN, εr)

for i in range(Ni):
for j in range(Nj):
τc[i,j] = get_τc(i,j,dhot,dx,dz,Ni-1,Nj-1,tau,tau_red)
```

```
# initialize The S,κ,σ,Ce,ΔT lists
ΔT = np.zeros(Ni)
Ce = np.zeros(Ni)
σ = np.zeros(Ni)
S = np.zeros(Ni)
κ = np.zeros(Ni)
deltaS = np.zeros(Ni)
for i in range(Ni):
Ce[i] = get_cv(EF[i],T0,T0/10)/t_gr

for i in range(Ni):
σ[i] = -get_cond(EF[i],T0,nstar,mob)

for i in range(Ni):
κ[i] = Lor*σ[i]*T0/t_gr

for i in range(Ni):
S[i] = get_seebeck(EF[i],T0,nstar,mob)


T0 = 300

c1 = np.zeros(Ni)
c2 = np.zeros(Ni)
c3 = np.zeros(Ni)
c4 = np.zeros((Ni,Nj))
ξ = np.zeros((Ni,Nj))
c5 = np.zeros((Ni,Nj))
norm_abs = np.zeros(Ni)
#calc_params --> get S,Ce,κ,σ lists


for i in range(Ni):

c1[i] = Dx(κ,i,h)/κ[i]
deltaS[i] = Dx(S,i,h)
c2[i] = (1/(Lor*T0))*S[i]*deltaS[i]
c3[i] = (1/(Lor*T0))*S[i]**2
# scale by h**2

norm_abs[i] = get_absorption(lamda,EF[i],T0,tau_ee)/abs0


for i in range(Ni):
for j in range(Nj):
```

```
ξ[i,j]= math.sqrt(τc[i,j]*κ[i]/Ce[i])
c4[i,j] = -1/ξ[i,j]**2

c5[i,j] = Pin*A[i,j]*norm_abs[i]/(t_gr*κ[i])
return EF, τc, Ce, σ, S, κ, c1, c2, c3, c4, c5, ξ
```

Boundary conditions and relaxation algorithm

```
@jit(nopython=True)
def boundary_conditions(i,j,Tdist):

# Use Von Neuman boundary conditions dT/dx --> 0 at the boundary
# whitch translates to Ti+1 = Ti

if j-1 < 0:
Tu = Tdist[i,j]
else:
Tu = Tdist[i,j-1]

if j+1 > Nj-1:
Td = Tdist[i,j]
else:
Td = Tdist[i,j+1]

if i-1 < 0:
Tl = Tdist[i,j]
else:
Tl = Tdist[i-1,j]

if i+1 > Ni-1:
Tr = Tdist[i,j]
else:
Tr = Tdist[i+1,j]

return Tu, Td, Tl, Tr

@jit(nopython=True)
def cycle(dx,ω,nc,c1,c2,c3,c4,c5,tol):

if dx > 10**-6:
dx = dx*10**-9
#initialize Tdist, ΔTmax
```

```
ΔTmax = 0
T0 = 300
h = dx
Te = np.ones((Ni,Nj))*T0
Teprev = np.ones((Ni,Nj))*T0
ΔTmax = 0
error1max = 0
error2max = 0

for k in range(nc):
jpos = 0
error1max = 0
error2max = 0
Tmax = T0
#print("number of cycles  = " + str(k+1))

for j in range(Nj):
for i in range(Ni):

Tu, Td, Tl, Tr  = boundary_conditions(i,j,Te)

Tnew = (-Td*c1[i]*h - 2*Td + Tl*c1[i]*h - 2*Tl - Tr*c1[i]*h - 2*Tr + Tu*c1[i]*h
- 2*Tu - 1.0/2.0*c3[i]*pow(Td - Tl + Tr - Tu, 2) + 600*c4[i,j]*pow(h, 2) -
2*c5[i,j]*pow(h, 2))/(Td*c2[i]*h - Tl*c2[i]*h + Tr*c2[i]*h - Tu*c2[i]*h +
2*c4[i,j]*pow(h, 2) - 8)
deltaT  = Tnew - Teprev[i,j]

Te[i,j] = Te[i,j] + ω*deltaT
# find the maximum temperature

if Te[i,j] > Tmax :
Tmax = Te[i,j]
jpos = j
ipos = i


error1ij = abs(Te[i,j]-Teprev[i,j])/(Te[i,j]+Teprev[i,j])*200
error2ij = abs(deltaT)/Te[i,j]*100

if error1ij > error1max:
error1max = error1ij

if error2ij > error2max:
error2max = error2ij
```

```
Teprev[i,j] = Te[i,j]


# what the current max deviation is from the alltime maximum deltaT

if error1max < tol :

return Te, Tmax, error1max, error2max, ipos, jpos, k

return Te, Tmax, error1max, error2max, ipos, jpos, k
```

PTE voltage calculation and associated figures of merit

```
@jit(nopython=True)

def CalcNEPDet(Pin,T0,R,Vpte,dx,dz):
im = Ni
jm = Nj
jj = 0
pi = np.pi
kb=1.38*10**-23
Active_Area = 0
for i in range(Ni):
for j in range(Nj):
Active_Area = Active_Area + dz*dx

NEP = math.sqrt(4 * kb * T0 / R) / abs(Vpte / R / Pin)
D = math.sqrt(Active_Area * 10**4) / NEP

return NEP, D

@jit(nopython=True)
def PTE(S,Tdist,dx,dz):
W = (Ni-1)*dx
L = (Nj-1)*dz

Vpte = 0


for i in range(Ni-1):
V = 0
jj = 0
for j in range(Nj-1):
```

```
T1 = Tdist[i,j]
T2 = Tdist[i+1,j]
jj = jj + 1

V = V + (S[i]+S[i+1])*(T2-T1)/2

Vpte = Vpte+V/jj



return Vpte


@jit(nopython=True)
def resistance(Rcont,normCond,dx,dz):
# Rcont in Ω*μm

R = 0
resistivity = np.zeros((Ni,Nj))

L = (Nj-1)*dz  # in nm
for i in range(Ni):
sig1=0
for j in range(Nj):
resistivity[i,j] = 1 / normCond[i]

sig1 = sig1 + normCond[i]

R = R + 1/sig1

R = R + Rcont / (L / 10**3) * 2  # Rcont is in Ω*μm
return R
```

Tabulation of thermodynamic matrices based on E(x,z) and T(x,z)

```
@jit(nopython=True)
def interpolator(x,y,f,dx,dy,xmin,xmax,ymin,ymax):

# x , y the point to be interpolated
```

```
# z 2D Matrix with the known points

#xmin , xmax , ymin , ymax dx , dy are the params of the xlist, ylist from witch
z was clalculated


nx = int((x-xmin)/dx)
ny = int((y-ymin)/dy)
r = np.array([x,y])
w = np.zeros((2,2))


# find the closest vertex


r00 = np.array([xmin+nx*dx,ymin+ny*dy])
r01 = np.array([xmin+nx*dx,ymin+(ny+1)*dy])
r11 = np.array([xmin+(nx+1)*dx,ymin+(ny+1)*dy])
r10 = np.array([xmin+(nx+1)*dx,ymin+ny*dy])



R00 = r-r00
R01 = r-r01
R11 = r-r11
R10 = r-r10



w[0,0] = np.linalg.norm(R00)
w[0,1] = np.linalg.norm(R01)
w[1,1] = np.linalg.norm(R11)
w[1,0] = np.linalg.norm(R10)



min_dist = np.min(w)

for i in range(w[:,0].size):
for j in range(w[0,:].size):
if w[i,j] == min_dist:
ii = i
jj = j

i = nx+ii
```

```
j = ny+jj
x0 = xmin+i*dx
y0 = ymin+j*dy


# Use a 2D taylor expansion to aproaximate the grid


# calculate the derivatives at the proximus(x0,y0) to the point of interest
(x,y)


# central difference for non boundary points



Δx = x-x0
Δy = y-y0


if x>xmin+dx and x<xmax-dx and y>ymin+dy and y<ymax-dy:

# Central difference for non boundary points
fx = (f[i+1,j]-f[i-1,j])/(2*dx)
fy = (f[i,j+1]-f[i,j-1])/(2*dy)
fxx = (f[i+1,j]+f[i-1,j]-2*f[i,j])/dx**2
fyy = (f[i,j+1]+f[i,j-1]-2*f[i,j])/dy**2
fxy = (f[i+1,j+1]-f[i+1,j-1])/(4*dx*dy)-(f[i-1,j+1]-f[i-1,j+1])/(4*dx*dy)


z = f[i,j]+fx*Δx+fy*Δy+(fxx*Δx**2+fyy*Δy**2+2*fxy*Δx*Δy)/2


else:
z = f[i,j]




return z
```

Initializing thermodynamic quantities lists based on E(x,z), T(x,z)

```
def init_thermo_lists(mob,nstar,dE,dT,Emin,Emax,Tmin,Tmax):
```

```
# initialize The S,κ,σ,Ce lists as functions of EF and T
E = np.arange(Emin,Emax+dE,dE)
T = np.arange(Tmin,Tmax+dT,dT)

Ce = np.zeros((E.size,T.size))
σ = np.zeros((E.size,T.size))
S = np.zeros((E.size,T.size))
κ = np.zeros((E.size,T.size))

for i in range(E.size):
for j in range(T.size):
Ce[i,j] = get_cv(E[i],T[j],T[j]/10)/t_gr

for i in range(E.size):
for j in range(T.size):
σ[i,j] = -get_cond(E[i],T[j],nstar,mob)
κ[i,j] = Lor*σ[i,j]*T[j]/t_gr

for i in range(E.size):
for j in range(T.size):

S[i,j] = get_seebeck(E[i],T[j],nstar,mob)


return Ce, σ, S, κ


def
init_params(tau,tau_red,tau_ee,EF_c,dtrans,dhot,dx,dz,Ni,Nj,T0,A,EF_left,EF_r
ight,L_split,tSiN,εr,lamda):

#initialize position based parameters

abs0 = get_absorption(lamda,0,T0,tau_ee)
h = dx
EF = np.zeros(Ni)
τc = np.zeros((Ni,Nj)) # electron - phonon scattering

# dx in nm
if dx < 10**-3:
xstep = dx/nm
else:
```

```
xstep = dx

EF  = calc_EF(dtrans, xstep, EF_c, EF_left, EF_right, Ni, L_split, tSiN, εr)


for i in range(Ni):
for j in range(Nj):
τc[i,j] = get_τc(i,j,dhot,dx,dz,Ni-1,Nj-1,tau,tau_red)



norm_abs = np.zeros(Ni)
abs0 = get_absorption(lamda,0,T0,tau_ee)

for i in range(Ni):
norm_abs[i] = get_absorption(lamda,EF[i],T0,tau_ee)/abs0

a = np.zeros_like(A)
for i in range(Ni):
for j in range(Nj):
a[i,j] = A[i,j]*norm_abs[i]


return EF, τc, a
```

Relaxation algorithm with Temperature dependent thermodynamic quantities.

```
@jit(nopython=True)
def
cycle(EFlist,τclist,alist,T0,Pin,ω,nc,tol,dT_update,Lattice_diffusion,dx,dz,N
i,Nj,dE,dT,Emin,Emax,Tmin,Tmax):

print("initiate cycling")

nm = 10**-9
um = 10**-6
dx = dx*nm
dz = dz*nm
ipos = -1
jpos = -1
#initialize Tdist,
```

```
Te = np.ones((Ni,Nj))*T0 # graphene electronic temperature
Teprev = np.ones((Ni,Nj))*T0
Tphprev = np.ones((Ni,Nj))*T0

Qlattice = np.zeros((Ni,Nj))
Temax = T0


κ = np.zeros((Ni,Nj))
S = np.zeros((Ni,Nj))
Celectronic = np.zeros((Ni,Nj))

# init the lists for T0 and EFlist --> solution of the electrostatics

for i in range(Ni):
for j in range(Nj):

κ[i,j] =  interpolator(EFlist[i],Te[i,j],κlist,dE,dT,Emin,Emax,Tmin,Tmax)
S[i,j] =  interpolator(EFlist[i],Te[i,j],Slist,dE,dT,Emin,Emax,Tmin,Tmax)
Celectronic[i,j]                                                              =
interpolator(EFlist[i],Te[i,j],Celist,dE,dT,Emin,Emax,Tmin,Tmax)

temp_last_update = T0


# Convergence  cycle
for k in range(nc):


jpos = 0
ipos = 0
erroremax = 0
errorphmax = 0
errormax = 0


if  Temax-temp_last_update > dT_update:
print("i update Thermo Quantites ")
temp_last_update = Temax
for i in range(Ni):
for j in range(Nj):

κ[i,j] =  interpolator(EFlist[i],Te[i,j],κlist,dE,dT,Emin,Emax,Tmin,Tmax)
S[i,j] =  interpolator(EFlist[i],Te[i,j],Slist,dE,dT,Emin,Emax,Tmin,Tmax)
```

```
Celectronic[i,j]                                                    =
interpolator(EFlist[i],Te[i,j],Celist,dE,dT,Emin,Emax,Tmin,Tmax)



# Calculate the electronic temperature at all the points in the grid
for j in range(Nj):

for i in range(Ni):




Tc, Tu, Td, Tl, Tr  = boundary_conditions(i,j,Ni,Nj,Te)

tau = τclist[i,j]
a = alist[i,j]
κc, κl, κr, κu, κd = boundary_conditions(i,j,Ni,Nj,κ)
Sc, Sl, Sr, Su, Sd = boundary_conditions(i,j,Ni,Nj,S)
Ce = Celectronic[i,j]


ξ = np.sqrt(tau*κc/Ce)

Q1 = ((Td - Tu)/(2*dz) + (-Tl + Tr)/(2*dx))*((κd - κu)/(2*dz) + (-κl +
κr)/(2*dx))/κc
Q2 = (-2*Tc + Td + Tu)/dz**2 + (-2*Tc + Tl + Tr)/dx**2
Q3 = Sc*Tc*((Sd - Su)/(2*dz) + (-Sl + Sr)/(2*dx))*((Td - Tu)/(2*dz) + (-Tl +
Tr)/(2*dx))/(Lor*Tlattice)
Q4 = Sc**2*((Td - Tu)/(2*dz) + (-Tl + Tr)/(2*dx))**2/(Lor*Tlattice)
Q5 = -(1/ξ**2)*(Tc-Tlattice)
Q6 = a*Pin/(t_gr*κc)


denom = 1/ξ**2+2/dz**2+2/dx**2
Tenew = (Q1 + Q3 + Q4 + Q6 + (Td/dz**2) + (Tl/dx**2) + (Tlattice/ξ**2) +
(Tr/dx**2) + (Tu/dz**2))/denom

deltaTe  = Tenew - Teprev[i,j]


# update the temperature according to the relaxation regime
Te[i,j] = Te[i,j] + ω*deltaTe

Qlattice[i,j] = Ce*t_gr*(Te[i,j]-Tlattice)/tau # energy lost to the lattice
```

```
# find the maximum temperature
if Te[i,j] > Temax :
Temax = Te[i,j]
jpos = j
ipos = i
# find the maximum deviation from previus iteration

erroreij = abs(Te[i,j]-Teprev[i,j])/(Te[i,j]+Teprev[i,j])*200

if erroreij > erroremax:
erroremax = erroreij

Teprev[i,j] = Te[i,j]


if errormax < tol :
return S, κ, Te, Temax, errormax , ipos, jpos, k

return S, κ, Te, Temax, errormax, ipos, jpos, k
```